The Dirac spectrum on a cosmic string loop.

Lyle, Ralph

Lyle, Ralph (2006) *The Dirac spectrum on a cosmic string loop..* thesis, Swansea University.
http://cronfa.swan.ac.uk/Record/cronfa42807

The Dirac Spectrum on a Cosmic String Loop

Ralph Lyle

February 14, 2006

Abstract

The bosonic fields associated with a local cosmic string loop are first derived analytically. The resulting equations of motion are solved by numerical simulation to form a stable background on which fermions can be introduced. The fermionic field is then evolved over time, with the Dirac equation also solved numerically both for a straight string and a loop. The oscillations that result at very small radius are finally analysed for the appearance of fermion mass, together with its implications for the lifetime of the microscopic superconducting loops, or vortons.

DECLARATION

This work has not previously been accepted for any degree and is not being concurrently submitted in candidature for any degree.

Signed..(candidate)
Date........14 February 2006..............

STATEMENT 1

This thesis is the result of my own investigations, except where otherwise stated. Other sources are acknowledged by footnotes giving explicit references. A bibliography is appended.

Signed..(candidate)
Date........14 February 2006..............

STATEMENT 2

I hereby give my consent for my thesis, if accepted, to be available for photocopying and for inter-library loan, and for the title and summary to made available to outside organisations.

Signed..(candidate)
Date........14 February 2006..............

Acknowledgements

I wish to express my gratitude to the University of Wales Swansea for the award of a Callaghan Scholarship, which was a very great help at the start of my research.

Many thanks must also go to my supervisor, Warren Perkins, for his patient explanations and helpful insights, that so clarified the progress of the research. This support and encouragement was much appreciated, especially during the low points.

I would like to thank my fellow students for helpful comments and entertaining discussions; also Dave Cope and David Jordan, who is to blame for persuading me to apply for a research degree in the first place.

To Ruth, Robin, Ellen and Leonard

Contents

Thesis Summary

The discovery by Witten [1] that cosmic strings could become superconducting had important implications for cosmology, and has led to intensified research into this type of defect. In particular, further work showed that stable superconducting loops known as vortons could form, and in certain cases possibly survive to the present day.

The current carriers on these loops can be bosonic or fermionic, and this research project is concerned with microscopic vortons, where fermions are the current carrier introduced on a background of static bosonic fields. In the case of the 2-dimensional derivation for a straight string, Jackiw and Rossi have shown[2] that at some distance from the core bosonisation occurs. However, unlike a straight string, loops are not topologically stable and as the radius becomes very small the appearance of mass terms is expected. After the bosonic fields have fully settled, fermions are introduced and allowed to evolve as the loop radius is steadily reduced.

Neither the bosonic nor the fermionic equations have known analytic solutions, so a numerical approach must be used in each case to solve the equations of motion. The technique uses the central difference method on the second derivative to calculate the numerical value at each point on a lattice. If a point is selected on the resulting fermionic profile, for example at the apex on the string, its decay over time after the fermionic fields have reached a stable configuration, may be analysed. By taking the logarithm of the gradient, it can be shown that this decay is exponential at all radii.

At larger radii, on or very close to the string core, the fermions are massless and moving at the speed of light. The expectation is that oscillations will commence at very small radius, indicating the acquisition of fermion mass, with the fermions finally attaining their normal vacuum mass when the loop vanishes as the radius approaches zero. We demonstrate that this does occur and then consider the implications this has for the lifespan of a vorton. Finally, a method for determining an approximate value for the lifespan is shown.

Chapter 1

Introduction

1.1 *Topological Defects*

Topological defects occur in various types of condensed matter systems, such as magnetic flux lines in a type II superconductor, quantized vortex lines in superfluid ^4He or nematic liquid crystals. In the context of cosmology and relativistic field theory, most Grand Unified Theories (GUTs) of fundamental forces provide theoretical evidence for the formation of similar types of defect, although there are differences such as in the dynamics, which tend to be friction dominated in condensed matter systems, rather than relativistic. These very early defects are of great interest to cosmologists due to their characteristics, which could have had profound effects on the evolution of the cosmos. The formation and classification of the different types of defect are looked at in more detail later, together with the reasons why most are now thought unlikely to have survived to the present. For now it is just stated that the linear defects known as cosmic strings are of particular interest as, unlike monopoles and domain walls, their energy density would not have been great enough to dominate that of the universe. They are also considered to be the most likely to have avoided early decay and in certain cases may have survived until the present time.

At first it was hoped that observational confirmation of the existence of cosmic strings might, due to their enormous mass and current carrying capability, provide explanations for the observed cosmos, particularly in areas such as large-scale structure formation, small-scale anisotropies in the cosmic microwave background radiation (CMBR), and ultra high-energy cosmic rays and gamma ray bursts. However, more recent results from WMAP, capable of much finer detail than COBE, would seem to throw doubt on the validity of some of these earlier speculations, indicating that much stronger constraints need to be imposed on the possible contribution from cosmic strings to any unevenness in the CMBR. It was further hoped that explanations might result for galaxy seeding and the existence of dark matter, and the contribution to GUT-scale baryogenesis from the formation of out-of-thermal equilibrium concentrations of Higgs and gauge fields. Although not ruled out, the likely influence due to cosmic strings on these phenomena is looking less promising[3]. Massive GUT strings should also cause gravitational lensing, and since their linear nature (wiggly rather than straight) would produce a different signature from the more usual point source such as a distant galaxy or quasar, this might provide further observational evidence for their existence. More promisingly, there is very recent possible evidence starting to appear, such as the anomalous brightness fluctuations in the quasar Q0957+561 A,B gravitational lens system [4], which may be due to lensing by an oscillating loop. Another example found by Sazhin et al is CSL-1, involving two images of an elliptical galaxy, together with further gravitational lens candidates in the vicinity[5][6][7].

1.2 *Phase Transitions and Spontaneous Symmetry Breaking*

Before looking in more detail at the formation and evolution of cosmic strings, it is necessary to examine briefly the basic mechanism which gives rise to topological defects in general.

The cosmological background is assumed to be the standard model with a hot Big Bang. This background is taken as a spatially flat, homogeneous, isotropic universe, with the Friedman-Robertson-Walker (FRW) metric,

$$ds^2 = dt^2 - a^2(t)\left(\frac{dr^2}{(1-kr^2)^{1/2}} + r^2 d\Omega^2\right), \tag{1.1}$$

where the constant $k = +1, 0, -1$ denotes a closed, flat or open universe, and the function $a(t)$ is the scale factor. With the Hubble parameter $H \equiv \dot{a}/a$, p and ρ the pressure and density of the ambient medium, the conservation of energy momentum gives,

$$\dot{\rho} + 3H(\rho + p) = 0, \tag{1.2}$$

with the equation of state of the medium,

$$p = p(\rho). \tag{1.3}$$

In this model the universe evolves in approximate thermal equilibrium against a decreasing background temperature T, which means that the conservation of entropy gives $a(t)T =$ a constant.

The following notation will be used throughout: the metric $g_{\mu\nu}$ has the signature $(+,-,-,-)$; $c = 1$. Greek indices are used for space and time, with Latin for space only.[3]

Immediately after the Big Bang rapid expansion was accompanied by cooling as the enormous initial energy decreased, until the temperature reached a critical value T_c. Between 10^{-39} and 10^{-37} seconds after the Big Bang, when the temperature was of order $10^{16} GeV$, a spontaneous symmetry breaking is predicted to have occurred in the form of a GUT phase transition, resulting in the separation of the strong nuclear force and the electroweak force.

Further phase transitions are predicted at lower energies, principally the electroweak symmetry breaking of the order of 100 GeV. The quark-hadron confinement transition at around 100 MeV - 1 GeV would not have involved a gauge symmetry breaking, although a chiral symmetry breaking is open to debate. However, for this particular research, which focuses on cosmic strings, the high energy GUT transition is of most interest due to the topological stability of the strings and their great mass, which means they are more likely to have had a greater influence on the subsequent evolution of the cosmos.

Strings formed at the electroweak transition in the standard model are not topologically stable, although stable strings can be produced at this level in supersymmetric models. However, their mass per unit length is very small - some 10mg m^{-1}, as opposed to GUT strings at $\sim 10^{21}$kg m^{-1} - although they might nevertheless have had significant astrophysical effects if superconducting. Some theories predict the possibility of an intermediate phase change between the GUT and electroweak transitions.

Phase transitions can be of two types. A second-order transition is governed by generally classical dynamics and proceeds smoothly in time and homogeneously in space, apart from the phase boundaries which form topological defects, from $\langle\phi\rangle = 0$ for $T \gg T_c$ to a non-vanishing vacuum expectation value $\langle\phi\rangle = \pm\eta$ for $T < T_c$.[3][9][17]

In contrast, a first-order transition proceeds by bubble nucleation, involves quantum mechanical effects and is discontinuous as a function of time. As the temperature falls below T_c a set of degenerate vacua develops, separated from the original (false) vacuum by a potential barrier. If the latter is high enough relative to the thermal energy of the system, then classically ϕ would remain trapped in the false vacuum state, but in fact quantum tunnelling can provide a means of overcoming this, with a probability per unit volume of space and time that a bubble of true vacuum will nucleate at some point $\vec{x}$, so that $\langle|\phi(\vec{x})|\rangle$ is not a continuous function of time.[9] Figure 1.1 shows how the potential changes as T falls, while figure 1.2 shows the effective potential in each case, for $T >> T_c$, before the phase transition and for $T = 0$ when the transition has occured. V_{eff} is the corrected potential after the classical potential, $V(\phi)$, has been modified due to ϕ being a quantum field. These

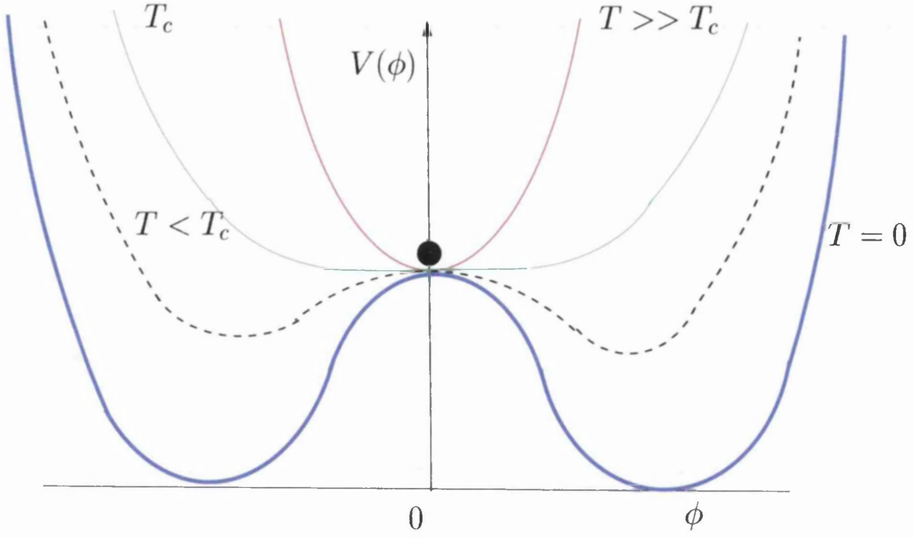

Figure 1.1: The classical potential $V(\phi)$ for different values of T above and below the critical temperature, T_c

radiative corrections to $V(\phi)$ are not significant in some models, but in the case of the abelian-Higgs model (1.13) which will be considered in section 1.6, the gauge coupling causes ϕ to acquire a non-trivial effective potential [10]. Both types of transition can result in defects, but the subsequent evolution of a defect does not depend on the type of transition that produced it.

As applied to relativistic field theory, T.W.B.Kibble first proposed an existence proof in 1976 for the formation of topological defects forming as a result of GUT phase transitions in the very early universe [11]. This is known as the Kibble mechanism, and is based on 1) that the presence of a defect can be determined by looking at the asymptotic field configuration, and 2) that the vacuum expectation value is uncorrelated for distances larger than $d_H(t) \sim t$, the causal horizon. This is because the correlation length $\xi(t) \lesssim t$, which is determined by the dynamics of the phase transition, cannot be established at speeds greater than c, and so cannot exceed the causal horizon[8]. Since then different experiments in the laboratory have verified the Kibble mechanism for string formation in liquid crystals, and it has also been tested in superfluid ^4He [12]. It essentially predicts that theories which admit topological defects will inevitably lead to their formation provided the correct conditions are

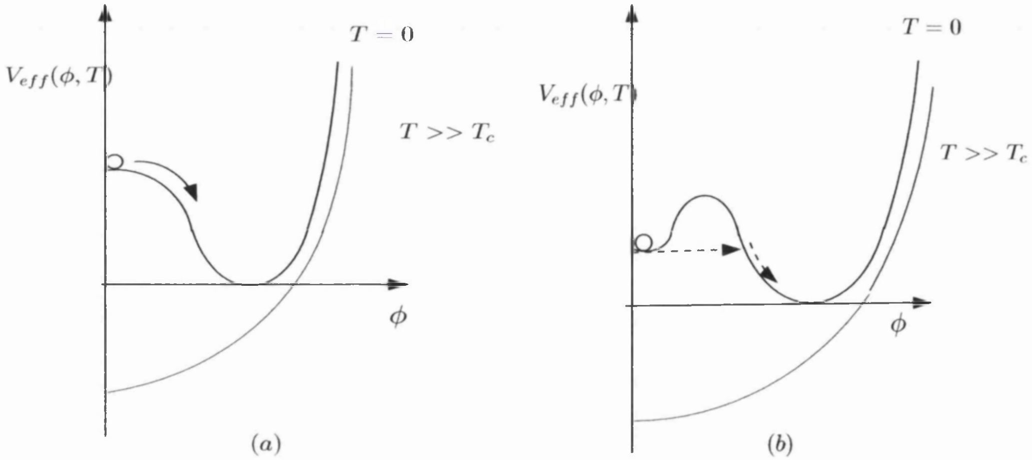

Figure 1.2: The temperature-dependent effective potential $V_{eff}(\phi, T)$ for (a) a second-order and (b) a first-order phase transition. Bubble nucleation (dotted arrows) enables the fields trapped in the false vacuum state to form bubbles of the true vacuum. The critical temperature T_c falls in between.

present, the principal requirement being that the topology of the vacuum manifold is nontrivial, and provided the process is not completely adiabatic[13].

The underlying principle behind various particle physics theories is the attempt to explain the different fundamental forces by means of spontaneous symmetry breaking during a phase transition. Up to the energy limits currently attainable, the standard model of particle physics has so far very successfully withstood experimental testing, particularly with the discovery of the predicted W and Z particles. This model, based on the symmetry group SU(3)×SU(2)×U(1), constitutes electroweak gauge theory based in turn on the symmetry group SU(2)×SU(1) which unifies the weak and electromagnetic interactions at around 100GeV, and together with QCD, constitutes the gauge theory of strong interactions, based on the symmetry group SU(3).

The purpose of GUTs is to predict the unification of all these forces at the earliest times and at an energy level of $10^{15} - 10^{16}$GeV. This still excludes gravity for which no satisfactory inclusive theory yet exists, but if it is found, unification might be expected to occur around 10^{19}GeV. This is the Planck energy scale $\sim 10^{-43}$s after the Big Bang, at which the gravitational force would become as strong as the other interactions [14]. At first it was thought there was no connection between cosmic strings and superstring theory, but it is now starting to appear that this may not be so and could lead to a theory for the unification of all the forces at the Planck scale[7].

The motivating force behind spontaneous symmetry breaking is the scalar Higgs field, which still remains hypothetical until the existence of the Higgs boson is proved. The symmetry breaking that occurs during the GUT transition is one of several thought to take place as the temperature falls, each time indicating the transition from a state of higher symmetry to one involving a smaller group of symmetry rules. Before the symmetry is broken, the field ϕ is everywhere in a vacuum state with a vacuum expectation value (VEV) of $\langle|\phi|\rangle = 0$. The symmetry-breaking scale η determines the critical temperature T_c, at which the symmetry breaks when the Higgs field adopts a specific orientation and the system chooses a new vacuum state with a finite value for ϕ. However, the location of this VEV on the vacuum manifold is not fixed.

Topological defects can take several forms depending on the way the symmetry breaking affects the Higgs field. This can result in a) two-dimensional domain walls, b) one-dimensional linear cosmic strings, c) zero-dimensional monopoles, or d) semi-topological textures. These are briefly examined in turn before focussing on cosmic strings.

a) The simplest field theory where the phase transition demonstrates spontaneous symmetry breaking is given by the Lagrangian [15],

$$L = \frac{1}{2}\partial_\mu\phi\partial^\mu\phi - V(\phi), \tag{1.4}$$

where $V(\phi) = \frac{1}{4}\lambda(\phi^2 - \eta^2)^2$ is the potential with degenerate minima at $\phi = \pm\eta$, as shown in Figure 1.3. The phase transition occurs at the critical temperature $T_c \sim \eta$ and as T falls, the field has to choose between the two degenerate minima, thus breaking the symmetry. The domain wall is the two-dimensional region of trapped energy separating two regions in space, R^3, with $\phi = \eta$ on one side, $\phi = -\eta$ on the other, as shown in Figure 1.4 (a) and (b). Since the symmetry-breaking scale in a GUT phase transition is $\eta \sim 10^{15}$ GeV, and the energy trapped per unit area of wall

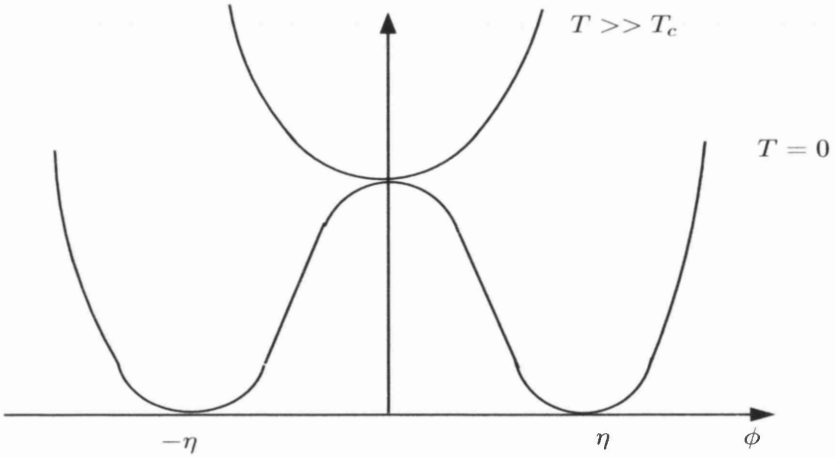

Figure 1.3: The high temperature potential for a domain wall when $T >> T_c$, and the symmetry-breaking potential when $T = 0$, with the two degenerate vacuum states when $\langle\phi\rangle = \pm\eta$.

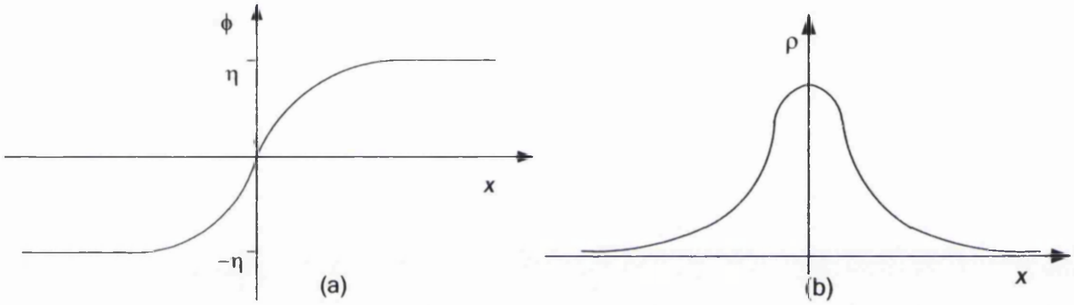

Figure 1.4: (a) The variation of ϕ across a domain wall and (b) the energy density as the field climbs over the potential peak

is of order η^3, the amount of energy involved is enormous[3].

b) For cosmic strings, the symmetry-breaking is illustrated by the "Mexican hat" diagram in Figure 1.5 , which is a three-dimensional projection of the magnitude of the potential $V(\phi)$ on the complex plane of the scalar field. At very high temperature the Higgs VEV lies at the bottom of the temperature-dependent potential V(ϕ), (red contour). At a lower temperature the field spontaneously rolls down the potential gradient to take one of an infinite number of possible positions on the blue circle of degenerate minima, which are the lowest energy states at the base of the 'Mexican hat' potential, where ϕ now acquires some finite value, $|\phi| = \eta$, as the system tries to minimise its energy. This breaks the previous symmetry of the field by giving it a specific orientation. In this way, unconnected regions of the original field which were

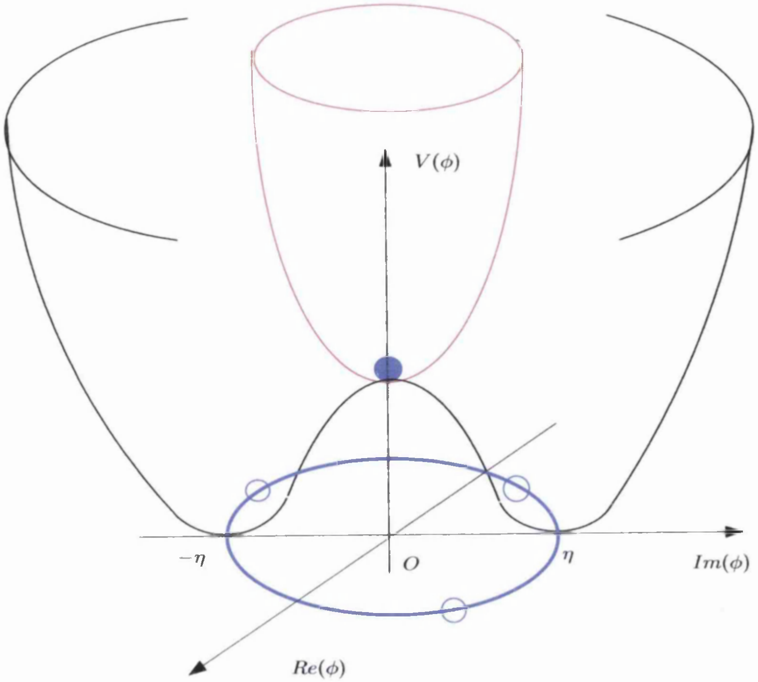

Figure 1.5: The 'Mexican hat' potential for a cosmic string. The unbroken symmetry potential on top of the central peak spontaneously rolls down the potential gradient to one of an infinite number of points on the circle of degenerate minima.

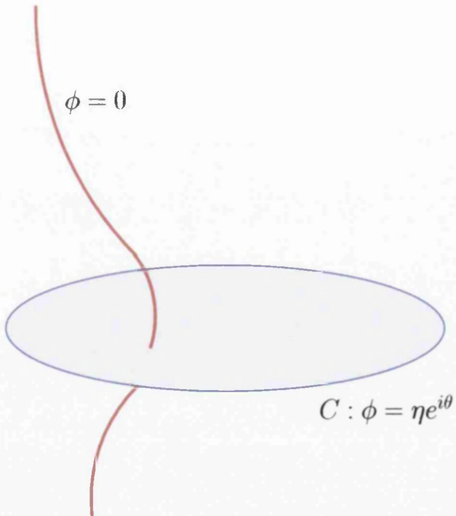

Figure 1.6: As ϕ winds around the circle C it is forced to vanish at some point on the disc spanned by C. The string is formed from the one-dimensional locus of points where $\phi = 0$ on different discs bounded by C[17].

not causally related take up different orientations as the phase transition proceeds. When these uncorrelated domains meet they are unable to merge smoothly and defects form at the interfaces, where they trap enormous energy.

The most basic example of symmetry-breaking resulting in a cosmic string, was proposed by Goldstone (1961) with the Lagrangian density [10],

$$L = (\partial_\mu \bar{\phi})(\partial^\mu \phi) - V(\phi), \tag{1.5}$$

where ϕ is the complex scalar field and the classical scalar potential is

$$V(\phi) = \frac{\lambda}{4}(\bar{\phi}\phi - \eta^2)^2, \tag{1.6}$$

with λ a dimensionless coupling constant, η the scale of symmetry breaking, and the string tension $\mu \sim \eta^2$, identified with the energy per unit length; for GUT strings $\eta \sim 10^{16}$ GeV. This model is invariant under the group $U(1)$ of phase transformations $\phi(x) \rightarrow e^{i\alpha}\phi(x)$, and is an example of a global transformation since α is independent of the spacetime location. The resulting cosmic string has no gauge fields to cancel the scalar gradients outside the core, but only massless Goldstone bosons which give rise to long-range forces[9].

c) Global monopole solutions result from the lagrangian,

$$L = |\partial_\mu \vec{\phi}|^2 - \frac{\lambda}{4}(\vec{\phi}^2 - \eta^2)^2, \tag{1.7}$$

where $\vec{\phi}$ is a triplet of scalar fields. The Lagrangian is invariant under the transformation,

$$\vec{\phi} \rightarrow \vec{\phi'} = R\vec{\phi}, \tag{1.8}$$

with R a rotation matrix in three dimensions, resulting in global $SO(3)$ symmetry which reduces to $SO(2)$ when $\vec{\phi}$ attains its VEV. If θ and ϕ are the angular spherical coordinates, a monopole solution is given by[17],

$$\vec{\phi} = \frac{\eta}{\sqrt{2}}\frac{f(r)}{e}\hat{e_r}(\sin\theta\cos\phi, \sin\theta\sin\phi, \cos\theta), \tag{1.9}$$

where $\hat{e_r}$ is the unit radial vector. Then $f(0) = 0$ ensures regularity at the origin of the 'hedgehog' configuration, Figure 1.7.

In the global case the energy of the monopole is infinite, as the gradient energy does not disappear at infinity, but this cancels out if a gauge field is present. In that case a finite energy solution results with a non-vanishing magnetic flux at infinity, known as a magnetic monopole, first proposed by 't Hooft [18] and Polyakov [19].

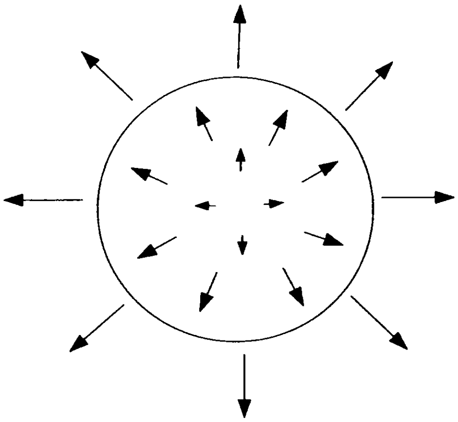

Figure 1.7: A monopole occurs when the minimum of the potential is a non-trivial radial field configuration on a 2-sphere which encloses the point-like defect.

The formation of very massive, stable magnetic monopoles is predicted in most GUTs[20].

d) A texture is a defect where the field takes vacuum values everywhere, but the gradient energy results in a non-trivial energy density. Thus textures can only occur in models that do not solely contain gauged symmetries, since all the scalar field gradients can be compensated by gauge fields [17]. Topologically non-trivial mappings from the 3-sphere into the vacuum manifold can result in textures. Figure 1.8 is a one-dimensional representation of how the Higgs field takes complex values as it winds round the line while remaining in the vacuum manifold $|\phi| = \eta$. The arrows indicate the phase vector. Textures result when $\vec{\phi_a} \equiv (\phi_1, \phi_2, \phi_3, \phi_4)$ with Lagrangian

$$L = \frac{1}{2}\partial_\mu\vec{\phi} \cdot \partial^\mu\vec{\phi} - V(\vec{\phi}), \tag{1.10}$$

where

$$V(\vec{\phi}) = \frac{1}{4}\lambda\left(\sum_{i=1}^{4}\phi_i^2 - \eta^2\right)^2, \tag{1.11}$$

with $\vec{\phi}$ a column vector of four real fields giving the vacuum manifold,

$$\phi_1^2 + \phi_2^2 + \phi_3^2 + \phi_4^2 = \eta^2. \tag{1.12}$$

Textures differ from other topological defects in various ways: they have no potential energy, all the energy being in spatial gradients. The winding number can be quantized as a result of Skyrmions stabilised by the $(\partial\phi)^4$ term but when unquantised, textures are unstable, tending to shrink and tunnel to a trivial vacuum state, and are regarded as semi-topological defects. They were at first considered as possible candidates for early structure formation; however recent COBE results make this very unlikely[21].

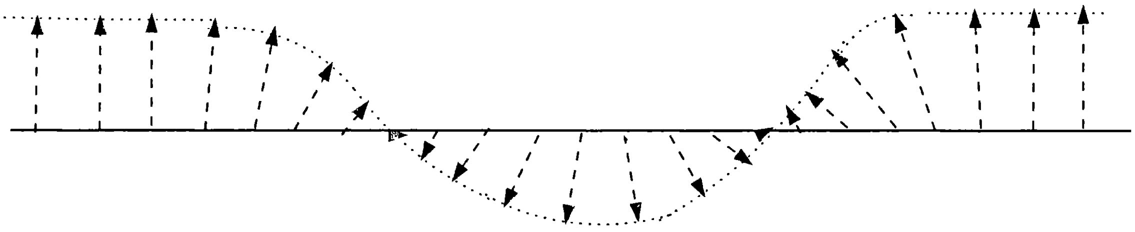

Figure 1.8: A texture in one spatial dimension

These are the main categories of defect, although there are more exotic types such as hybrids, which could be domain walls bounded by strings or monopoles connected by strings[20]. Domain walls and monopoles both pose serious problems for the standard cosmological model as their energy density decreases more slowly than the critical density with the expansion of the universe, and they could thus come to dominate the energy density of the universe [9].

1.3 *The Vacuum Manifold and Defect Classification*

Defects are classified by the topology of the vacuum manifold M as a symmetry-breaking occurs. In general, they are characterised by a restricted core where $\phi \notin M$, so that the potential $V(\phi) > 0$ and the associated quantized winding number means that the defect is topologically stable[3]. Table 1.1 lists the defect types associated with various topologies.

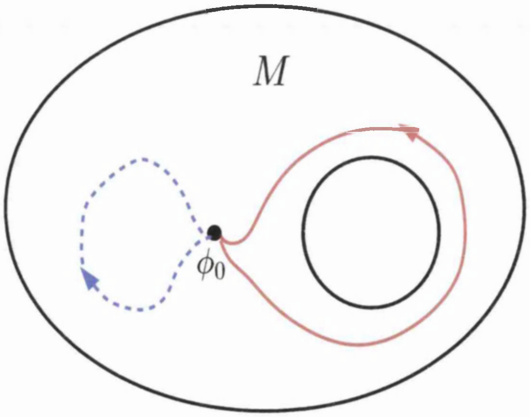

Figure 1.9: A topological surface of genus 1 or greater can form a multiply-connected vacuum manifold M, since the blue path can be contracted to a point, while the red path is non-contractible round the hole [8].

These topologies are defined by taking a group G containing all the symmetry transformations which leave the action invariant under certain field transformations. Then when the scalar field acquires a VEV ϕ_0, all transformations of this by elements of G which have a nontrivial effect on ϕ_0 will also be VEVs of the scalar field.

The elements of G which have a trivial effect on ϕ_0 form a subgroup of G, H. The nontrivial transformations are given by the left cosets of H and the coset space G/H containing all these nontrivial transformations forms the vacuum manifold, M.

When the topology of the vacuum manifold is nontrivial (in other words it contains more than just the identity element), topological defects can form. The different types of defect are classified by the order of the underlying homotopy group, $\pi_n(M)$, to which they belong, consisting of the equivalence classes of those paths that can be transformed into each other. In particular, strings occur when the underlying homotopy group is $\pi_1(M)$, containing one-dimensional closed paths that are non-contractible, as in Figure 1.9.

homotopy group $\pi_n(M)$		spatial dimension	type
$\pi_0(M) \neq 1$	M disconnected	2	domain wall
$\pi_1(M) \neq 1$	non-contractible loop in M	1	cosmic string
$\pi_2(M) \neq 1$	non-contractible 2-sphere in M	0	monopole
$\pi_3(M) \neq 1$	non-contractible 3-sphere in M	-	texture

Table 1. *The defects resulting from the different topologies of M*

Several GUTs involve symmetry-breaking from $G = SO(10)$ and $SU(5)$ (the smallest grand unified group) which result in the formation of strings. For example, the standard model symmetry group, which in itself cannot create stable defects, can have a symmetry-breaking chain of the form, $G_{GUT} \rightarrow H \rightarrow ... \rightarrow SU(3) \times G_{EW}$, where H is a possible intermediate symmetry group and $G_{EW} = SU(2) \times SU(1)$ is the electroweak symmetry group. Another example which results in the formation of strings is $SO(10) \rightarrow SU(5) \times Z_2$, where Z_2 is non-trivial.[23][16][3]

1.4 *The Evolution of Cosmic Strings and Horizon Scaling*

Unlike gauge monopoles and domain walls, whose energy density decreases more slowly than the critical density as the universe expands, GUT strings evolve with a constant fraction of the critical density, so that $\rho_{strings} \propto \eta^2 t^{-2}$ [9]. If the configuration stretches with the Hubble expansion, the string length would increase in proportion to the cosmic scale factor in a comoving volume, in which case the strings would come to dominate the energy density of the universe. Since this is clearly not the case, there must be energy loss mechanisms which prevent this and determine the final state adopted by the network [8].

Lattice simulations show that the initial network of strings produces results with over 80% of the string density in the form of infinite strings, which implies strings with radius of curvature greater than the Hubble radius, since they cannot have free ends [8]. The remainder is in the form of string loops in a scale-invariant distribution,

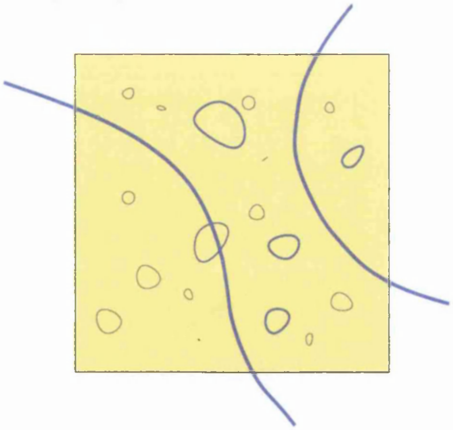

Figure 1.10: The scaling solution for the cosmic string network. The box represents one Hubble volume at arbitrary time t [22].

so that the number density of loops of size between R and $R + \partial R$ is proportional to $\partial R / R^4$. The simulations show that on large scales the strings are Brownian, with length l in a distance R given by, $l \propto R^2$ [15]. Figure 1.10 shows how the long strings cross a Hubble volume at a time t, together with a greater number of loops of radius $R << t$ [22].

After formation, the string network evolves due to various forces and influences, such as tension, friction due to its motion through the ambient medium, the Hubble expansion, intercommuting between strings or self-intersection, and energy loss mechanisms such as gravitational wave emission. For GUT strings, which form in the radiation-dominated era, there is considerable damping early on from the background radiation and friction is important particularly at first before the Hubble expansion dilutes the ambient medium, at the same time diluting and stretching the string network. Long strings also lose energy by intercommuting and self-intersection to produce small loops, so maintaining the energy-density fraction of the string network to the matter in the universe. These loops are subject to enormous tension which causes them to oscillate and decay through the emission of gravitational radiation. A scaling solution for the infinite string network means that at every epoch the network has the same statistical properties, which are time-independent if all distances are

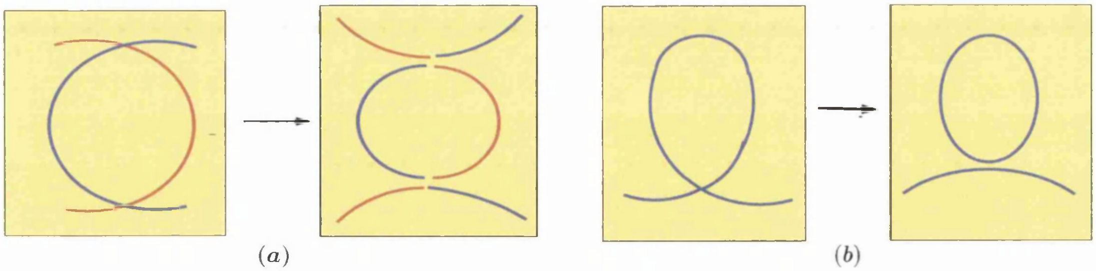

Figure 1.11: Two methods of loop formation by (a) intercommuting strings and (b) a self-intersecting string

scaled to the horizon size. [13], [15], [3]

The formation of cosmic strings in an inflationary context must also be considered, for although inflation is not required for the creation of defects, a problem arises if they formed before it commenced. In that case the defects would have become so diluted by the subsequent inflationary expansion that any detection today would be very unlikely. There are models which resolve this problem by having strings form during the later stages of inflation.

Another more recently considered possibility is topological inflation. In this case inflation, which results from the energy of the false vacuum, is driven by the defect itself, provided the radius of the core containing the false vacuum is greater than the horizon size at the time of formation [10].

1.5 *The Local and Global Solutions to the Abelian-Higgs Model*

We first consider local strings which, as opposed to those derived from a global transformation, have most of their energy confined in a very thin core due to the gauge fields that cancel the external field gradients. These fields also mean that the string core can have a quantized magnetic flux and that the mass per unit length is now finite.

Local abelian-Higgs vortices are analogous to the flux tubes in type II superconductors, with the difference that Neilsen-Olesen vortices exist in the vacuum background, while superconductor vortices live in a background of charged bosons, or Cooper pairs.

The simplest local gauge theory is the abelian-Higgs model, which describes the coupling of the scalar and electromagnetic fields and has the Lagrangian density,

$$L = D_\mu \phi^\dagger D^\mu \phi - \frac{1}{4} F_{\mu\nu} F^{\mu\nu} - \frac{\lambda}{4}(|\phi|^2 - \eta^2)^2, \qquad (1.13)$$

where ϕ is the complex scalar field and $F^{\mu\nu}$ is the field strength tensor.

1.5.1 *Gauge Invariance and the Field Equations*

Before looking at the Nielsen-Olesen vortex in more detail, we need to demonstrate the gauge invariance of the Lagrangian by defining the gauge transformation, followed by the derivation of the field equations from the Lagrangian.

If we choose the local, or coordinate dependent, $U(1)$ gauge transformation,

$$A_\mu(x) \to A_\mu(x) - \delta A_\mu(x) = A_\mu(x) - \frac{1}{e}\partial_\mu \alpha(x), \qquad (1.14)$$

where $A_\mu(x)$ is the gauge field and e is a coupling constant identified with the electric charge, with the space-time dependent phase change,

$$\phi \to e^{i\alpha(x)}\phi, \quad \phi^\dagger \to e^{-i\alpha(x)}\phi^\dagger, \qquad (1.15)$$

then with covariant derivative,

$$D_\mu \phi = (\partial_\mu + ieA_\mu)\phi, \qquad (1.16)$$

and defining

$$F_{\mu\nu} = \partial_\mu A_\nu - \partial_\nu A_\mu, \qquad (1.17)$$

substitution in the Lagrangian shows that it is gauge invariant.

The field equations are derived by applying the Euler-Lagrange equations of motion to the Lagrangian. The scalar equation,

$$\partial_\mu \left(\frac{\partial L}{\partial(\partial_\mu \phi)} \right) - \frac{\partial L}{\partial \phi} = 0, \qquad (1.18)$$

gives (a) the scalar equation of motion in gauge-invariant form,

$$(D_\mu D^\mu \phi)^\dagger + \frac{\lambda}{2}\phi^\dagger(|\phi|^2 - \eta^2) = 0; \qquad (1.19)$$

and (b) the vector equation of motion,

$$\partial_\nu\left(\frac{\partial L}{\partial(\partial_\nu A_\mu)}\right) - \frac{\partial L}{\partial A_\mu} = 0, \tag{1.20}$$

where

$$\partial_\nu\left(\frac{\partial L}{\partial(\partial_\nu A_\mu)}\right) = \partial_\alpha\left(\frac{\partial L}{\partial(\partial_\alpha A_\beta)}\right) = -\frac{1}{4}\left(2F^{\mu\nu}\frac{\partial F_{\mu\nu}}{\partial(\partial_\alpha A_\beta)}\right) = -\partial_\mu F^{\mu\nu}. \tag{1.21}$$

and

$$\begin{aligned}\frac{\partial L}{\partial A_\mu} &= \frac{\partial}{\partial A_\beta}[(\partial_\beta\phi^\dagger - ieA_\beta\phi^\dagger)(\partial^\beta\phi + ieA^\beta\phi)] \\ &= -ie\phi\partial_\beta\phi^\dagger + ie\phi^\dagger\partial_\beta\phi - 2e^2A_\beta\phi^\dagger\phi.\end{aligned} \tag{1.22}$$

After combining and rearranging, the second equation of motion becomes,

$$-\partial_\mu F^{\mu\nu} - ie(\phi^\dagger\partial_\nu\phi - \phi\partial_\nu\phi^\dagger) + 2e^2A_\nu\phi^\dagger\phi = 0. \tag{1.23}$$

1.5.2 *The Local Nielsen-Olesen Vortex Solution*

In chapter 2 (1.19) and (1.23) are derived for a loop in cylindrical polar coordinates in 2+1 dimensions to form the bosonic background for the fermions, and the resulting equations now form the basis from which the static one-dimensional case can be derived for a straight string. This will then yield the Nielsen-Olesen vortex solution to the basic local Abelian Higgs Lagrangian [24]. The four equations, which are derived in Chapter 2, consist of one scalar and three gauge equations,

$$\begin{aligned}&(\partial_0^2 - \partial_r^2 - \frac{1}{r}\partial_r - \frac{1}{r^2}\partial_\theta^2 - \partial_z^2)\phi^\dagger + (\partial_r A_r + \frac{1}{r}A_r + \frac{1}{r}\partial_\theta A_\theta + \partial_z A_z)\phi^\dagger \\ &+2i(A_r\partial_r + \frac{1}{r}A_\theta\partial_\theta + A_z\partial_z)\phi^\dagger + (A_r^2 + A_\theta^2 + A_z^2)\phi^\dagger + \phi^\dagger(\phi^\dagger\phi - 1) = 0.\end{aligned} \tag{1.24}$$

$$\begin{aligned}&\partial_0^2 A_r - \frac{1}{r^2}\partial_\theta^2 A_r - \partial_z^2 A_r + \frac{1}{r}\partial_r\partial_\theta A_\theta - \frac{1}{r^2}\partial_\theta A_\theta + \partial_r\partial_z A_z \\ &-i(\phi^\dagger\partial_r\phi - \phi\partial_r\phi^\dagger) + 2A_r\phi^\dagger\phi = 0,\end{aligned} \tag{1.25}$$

$$\begin{aligned}&\partial_0^2 A_\theta - \partial_r^2 A_\theta - \partial_z^2 A_\theta + \frac{1}{r}\partial_r\partial_\theta A_r - \frac{1}{r^2}\partial_\theta A_r - \frac{1}{r}\partial_r A_\theta + \frac{1}{r^2}A_\theta + \frac{1}{r}\partial_\theta\partial_z A_z \\ &-i(\phi^\dagger\partial_\theta\phi - \phi\partial_\theta\phi^\dagger) + 2A_\theta\phi^\dagger\phi = 0,\end{aligned} \tag{1.26}$$

$$\partial_0^2 A_z - \partial_r^2 A_z - \frac{1}{r^2}\partial_\theta^2 A_z - \frac{1}{r}\partial_r A_z + \partial_r\partial_z A_r + \frac{1}{r}\partial_z A_r + \frac{1}{r}\partial_\theta\partial_z A_\theta$$

$$-i(\phi^\dagger\partial_z\phi - \phi\partial_z\phi^\dagger) + 2A_z\phi^\dagger\phi = 0. \tag{1.27}$$

To adapt these equations to a static, cylindrically-symmetric straight-string configuration, the string is considered to lie along the z-axis, and as the system is symmetrical, $\partial_z = 0$, and A_r, $A_z = 0$. If it is static, $\partial_0(), A_0 = 0$, so after removing any time-dependent terms, we are then left with a scalar equation and a gauge equation in A_θ,

$$(-\partial_r^2 - \frac{1}{r}\partial_r - \frac{1}{r^2}\partial_\theta^2 - \partial_z^2)\phi^\dagger + \frac{ie}{r}A_\theta\partial_\theta\phi^\dagger + e^2A_\theta^2\phi^\dagger + \frac{\lambda}{2}\phi^\dagger(\phi^\dagger\phi - \eta^2) = 0, \tag{1.28}$$

$$-\partial_r^2A_\theta - \frac{1}{r}\partial_rA_\theta + \frac{1}{r^2}A_\theta - \frac{ie}{r}(\phi^\dagger\partial_\theta\phi - \phi\partial_\theta\phi^\dagger) + 2e^2A_\theta\phi^\dagger\phi = 0. \tag{1.29}$$

Specifying the Ansatz,

$$\phi^\dagger = fe^{-in\theta}, \tag{1.30}$$

$$A_\theta = -n\alpha/er, \tag{1.31}$$

where n is the Higgs field winding number, taken as 1, and asymptotic boundary conditions for a local vortex solution,

$$f(r) \to 1, \quad r \to \infty,$$

$$\alpha(r) \to 1, \quad r \to \infty. \tag{1.32}$$

On the string, at the vortex centre, regularity at the origin is ensured by putting,

$$f(0) = \alpha(0) = 0, \tag{1.33}$$

Substituting (1.30) and (2.17) in (1.28) and (2.16), with primes denoting differentiation with respect to r, the two equations become,

$$-f'' - \frac{1}{r}f' + \frac{1}{r^2}(\alpha - 1)^2f + \frac{\lambda}{2}f(f^2 - \eta^2) = 0, \tag{1.34}$$

$$\alpha'' - \frac{1}{r}\alpha' - 2e^2(\alpha - 1)f^2 = 0. \tag{1.35}$$

These equations have no known analytical solutions, but approximate asymptotic solutions can be found [10]. Rescaling with,

$$f \to \eta p, \quad r^2 \to \frac{2\rho^2}{\lambda\eta^2},$$

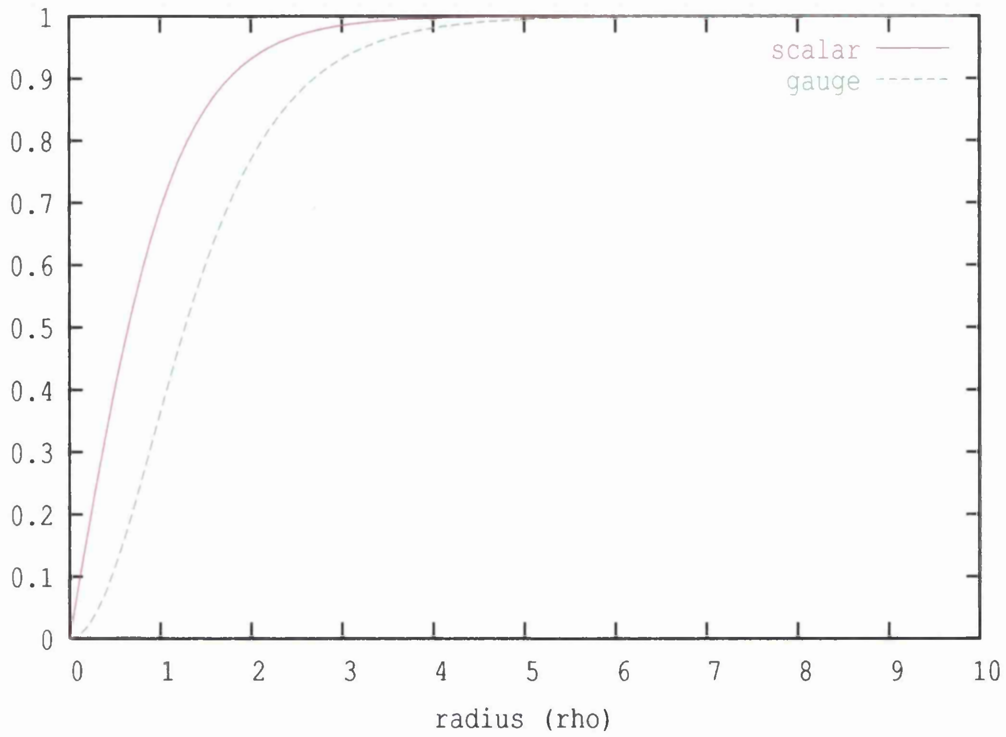

Figure 1.12: The Nielsen-Olesen cylindrically-symmetric vortex solutions with n=1, for the scalar function $p(\rho)$ and vector function $a(\rho)$.

to eliminate λ and η gives the second-order differential equations

$$p'' + \frac{1}{\rho}p' - \frac{1}{\rho^2}(\alpha - 1)^2 p - p(p^2 - 1) = 0, \tag{1.36}$$

$$\alpha'' - \frac{1}{\rho}\alpha' - 2(\alpha - 1)p^2 = 0, \tag{1.37}$$

which can then be reduced to two double systems of non-linear, first-order ordinary equations. Expanding p and α as power series, we find that $p = a.\rho + O(\rho^3)$ and $\alpha = b.\rho^2 + O(\rho^4)$. At very small radius, the condition (1.33) requires starting values a, b, for p and α. These constants are found by trial and error to ensure the asymptotic behaviour of the two functions.

Numerical solutions may be obtained using the 4th-order Runge-Kutta method, and the resulting 1-dimensional scalar and gauge profiles are shown in Figure 1.12 with $\rho <= 10$. We find that a=0.85..., b=0.49...,to 9 decimal places at this radius, the number of places increasing rapidly as ρ is increased. Figure 1.13 is the Higgs vortex when the scalar field profile is rotated about the string.

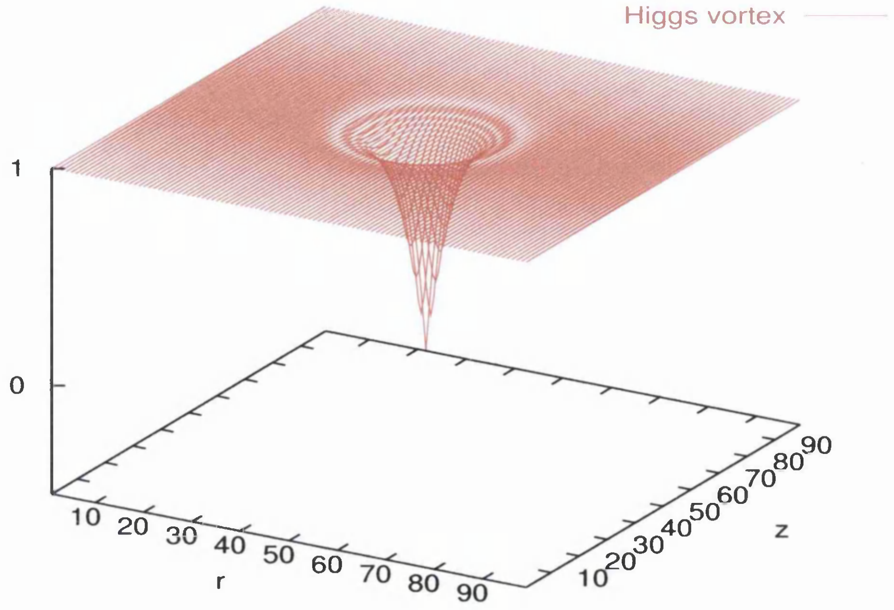

Figure 1.13: The Higgs vortex when $p(\rho)$ is rotated about the string

1.5.3 *The Global Solution to the Abelian-Higgs Model*

The global solution is briefly considered because it is interesting to compare the scalar field with the local case. The abelian-Higgs model without the gauge fields gives the Goldstone model (1.5) in which the field equations become

$$\partial_\mu \partial^\mu \phi^\dagger + \frac{\lambda}{2}\phi^\dagger(\phi\phi^\dagger - \eta^2) = 0; \tag{1.38}$$

In this case there is no Higgs mechanism operating at the global symmetry breaking, and there is no gauge field to compensate the angular gradient of the scalar field away from the core. As a result, the energy per unit length is logarithmically divergent with a power law decay mode instead of the local mode, where ϕ approaches the VEV exponentially. With the same ansatz used to obtain the local solution, $\phi^\dagger(\mathbf{r}) = f(r)e^{-in\theta}$ and the same boundary conditions, the field equations (1.13, 1.14) reduce (with n=1) to,

$$f'' + \frac{1}{r}f' - \frac{1}{r^2}f - \frac{\lambda}{2}f(f^2 - \eta^2) = 0. \tag{1.39}$$

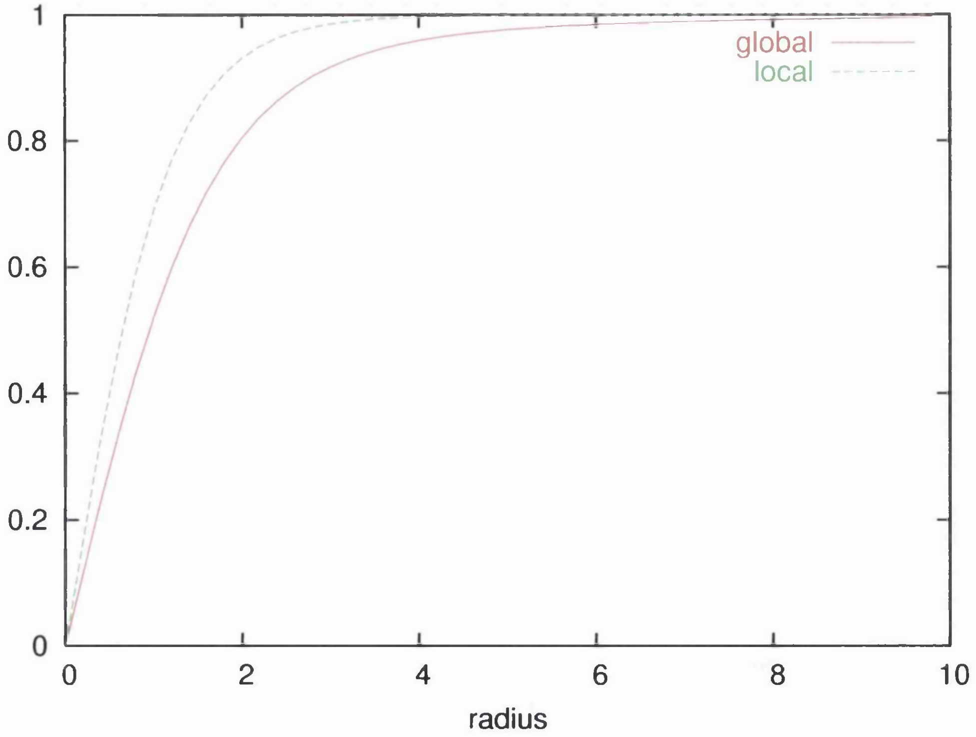

Figure 1.14: The global straight string solution compared with the local solution for the Abelian-Higgs Lagrangian

The rescaled equation can then be solved using the same numerical methods as before, with the coefficient now 0.58... The resulting profile is compared with the local solution in Figure 3.1.1[10]

1.6 *Superconducting Strings and Vorton Formation*

Witten[1] first demonstrated the possibility that cosmic strings might behave like superconducting wires able to carry large charge, and in the case of GUT strings, potentially enormous currents, so opening up new cosmological possibilities. While ordinary Nambu-Goto strings - the simplest type - would sooner or later radiate away their energy and eventually disappear, this need not be the case with Witten type superconducting strings [25]. As such longer-lived strings moved at relativistic speeds through the primordial plasma in the radiation-dominated era, they could have had a profound effect on galaxy formation by creating significant magnetic fields. This offered an interesting new way in which strings and more particularly loops, might prolong their existence with longer-term effects.

To find the reason why strings become superconducting, it is necessary to look at what is happening inside the core. Charged fermions, for example, would become essentially massless due to interactions between their own field and the Higgs field that formed the string. In that case, only a small amount of energy would be required to produce pairs of trapped fermions, which being massless could propagate at the speed of light on the core. These fermions produce the zero energy states, or fermionic zero modes, and are responsible for the fact that both straight strings and loops can carry currents, and in the latter case also cause the angular momentum [26].

If the current carriers are bosonic (which will not be considered further here), the charged Higgs field has a non-zero expectation value in the string core; if they are fermionic, the fermions couple to the string fields creating fermion zero modes, which are zero- energy solutions to the Dirac equation in the bosonic string background. In this vortex background the massless states are confined to the core, the fermions only being able to acquire mass if they move off the core. If these fermions also carry electric charge, either string motion through a magnetic field, or electric fields along the string can produce currents on the string which persist even when the electric field is turned off and in this sense the strings are said to be superconducting. This effect may be interpreted in terms of the Dirac sea where, without an applied electric field, the negative energy states of both the left and right movers are filled, while the positive states are not [27].

The current on a superconducting string depends on the flux of the magnetic field that it has passed through, and its motion through the surrounding medium leads to electromagnetic radiation which can dissipate the string energy. If this radiation is considered as a possible cause of spectral distortions in the CMB, this would place constraints on the density of superconducting strings in the early universe and on the amount of current they would be able to carry. [15][9]

In the period following the phase transition, loops formed as a result of string interactions and intersections in the original string network and, like the strings that gave rise to them, also moved at relativistic speeds, emitting gravitational radiation. Initially the loops can be quite large and irregular, but damping from the surrounding medium and the loss of energy from radiation emission cause them to shrink and become more circular. If a loop does not carry a current, symmetry does not make it possible to define a rotation round an axis perpendicular to the loop plane, and the loop will continue to oscillate and shrink due to the string tension, emitting gravitational radiation until it finally disintegrates in a burst of particles. Any current around the loop will break the symmetry and make rotation possible. This can prevent decay when the string tension is balanced by the angular momentum of the trapped charge, and the resulting stationary vortex loops are known as vortons, although not all loops with given characteristic quantum numbers N and Z necessarily become vortons [28].

R.L. Davis and E.P.S. Shellard consider three vorton formation regimes [29]. The earliest formation of vortons would have resulted from the irregular loops created from the brownian network of vortices produced during the GUT phase transition. A requirement would have been bosonic or fermionic bound states on the strings, so that the resulting loops could carry currents and charge quantum numbers. Since the loops at first were in a highly excited state, a further necessary condition would be that they could relax into a stationary circular vorton state, which would require that some quantum numbers remain as the loop loses energy and shrinks. This first period of formation would have occurred in the overcritically damped period with small cosmological stretching, and is the most likely because the strong damping would prevent the initial string current being much larger than the vorton current. This would ensure the greater probability of irregular loops evolving into vortons with similar quantum numbers.

In the next period, fewer loops would survive initially overcritical damping followed by subcritical damping which causes them to oscillate and relax. Because strings could have points on them reaching relativistic speeds, the vortons formed would need to be more robust to survive. During the third stage, the vortons are the least likely to form. The irregular loops enter the horizon at a later time, and must then undergo radiation damping accompanied by violent, relativistic motion [29].

However, it should be pointed that a later model by C.J.A.P. Martins and E.P.S. Shellard (1998)[30], throws doubt on this formation sequence, because if the friction-dominated epoch were too short to allow currents and charges to build up sufficiently to prevent the strings from becoming relativistic, with consequent losses, GUT-scale vortons would have been unlikely to form. Instead, vorton formation would be more likely as the energy scale for string production became less. Their analysis suggests that even intermediate-scale vortons should also be ruled out, because they could lead to a matter-dominated universe at an earlier stage than is allowed observationally. The result would be that plentiful vorton formation would only occur as the string-producing energy scale fell to around $T \sim 10^2 GeV$, when the vortons might contribute as much as 6% of the critical density, and could also be strong dark-matter candidates.

The question of the stage at which vortons would form also has to take into account certain constraints, in particular nucleosynthesis and the existence of dark matter, and this determines an upper temperature limit.[30][31][32]

From a distance vortons appear particle-like, as they are apparently point masses possessing quantized electric charge and angular momentum. They are extremely small, with a loop width 10-100 times the string width, and since the latter is approximately 10^{-30}m, this means that a vorton is about 10^{14} times smaller than a proton. The charge they can carry is typically 100 times that of the electron, and their mass is of the order of 10^{20} times greater [9].

Vortons are classically stable, but susceptible to quantum tunnelling. If this were rapid enough it might help overcome the problem of excess energy density that vortons formed very near the original phase transition could cause if their lifetimes were very extended.

It is assumed that the vortons under consideration carry particle and antiparticle zero modes moving in opposite directions (left and right movers), similar to Dirac masses on electro-weak strings. If both modes are populated, the net effect is to reduce the charge and increase the current, because the antiparticles carry opposite charge.

Chiral vortons, which appear in some supersymmetric models, such as the SUSY D-term model, are not considered here, but should be mentioned as they have attracted interest more recently; there are reasons to expect that they may have been the most numerous to form initially, and their possible longevity could make them of cosmological importance. Chiral vortons are characterised by having equal charge and current with the conserved current being null, which means that it is the boundary between time-like and space-like currents, and has rotation velocity $v = 1$, comparable to lightspeed [26]. Such chiral loops carry fermion zero modes of either a particle or an antiparticle moving at the speed of light in one direction only.

We end this section and the introduction with a brief preview of the main aim of this research, which poses the questions:

a) Do fermions on a vorton acquire mass as the radius is reduced, and at what radius

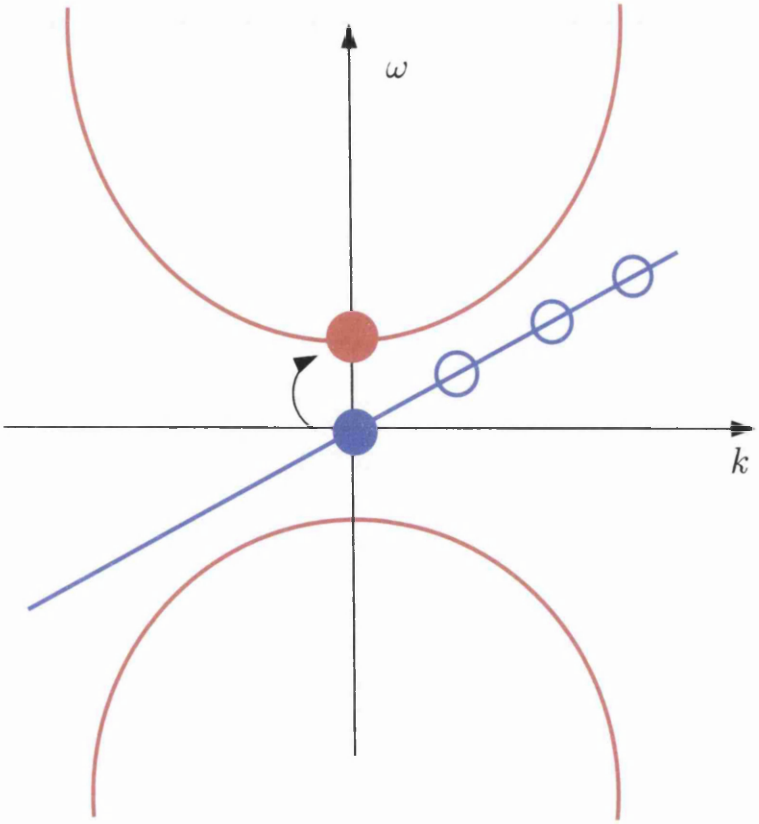

Figure 1.15: On the straight string (blue) there is only one zero energy mode. All the other modes have higher energy and carry momentum and because of the conservation of energy and momentum they cannot get onto the curve (red) and become massive. We are concerned with the point on the curve where the fermion has mass ω and $k = 0$, ensuring there is no momentum around the loop.

does this start to occur?

b) If so, do they acquire their vacuum mass as they move off the string when the vorton finally dissipates at minimum radius?

c) Given the typical vorton dimensions already suggested, can we determine an approximate figure for the lifetime of a vorton? This question is very important because if the current decay rate is too rapid, the vortons cannot have any significant cosmological effects, and if too slow, vorton domination of the critical mass of the universe becomes a problem . The Figure 1.15 illustrates the basis of this research, with a zero mode fermion possessing sufficient energy to move off the string to become a massive particle on the curve of massive modes.[27][33][34]

Chapter 2

The Bosonic Fields

2.1 *The Equations of Motion*

The bosonic fields in 3+1 dimensions can now be derived from the scalar and gauge equations of motion (1.19) and (1.23),

$$\partial_\mu\partial^\mu\phi^\dagger - ie\partial_\mu A^\mu\phi^\dagger - 2ieA^\mu\partial_\mu\phi^\dagger - e^2A_\mu A^\mu\phi^\dagger + \frac{\lambda}{2}\phi^\dagger(\phi\phi^\dagger - \eta^2) = 0, \tag{2.1}$$

$$-\partial_\mu F^{\mu\nu} - ie(\phi^\dagger\partial_\nu\phi - \phi\partial_\nu\phi^\dagger) + 2e^2A_\nu\phi^\dagger\phi = 0, \tag{2.2}$$

enabling the consideration of a string in the form of a loop centered about the z-axis, as shown in figure 2.1.

In the Minkowski metric, with

$$A_\mu = g_{\mu\nu}A^\nu, \quad \partial^\mu = (\partial_0, -\underline{\nabla}), \quad \partial_\mu = (\partial_0, +\underline{\nabla}), \quad \partial_\mu\partial^\mu = \partial_0^2 - \nabla^2,$$

the equations give, in Cartesian coordinates,

$$\begin{aligned}\Box\phi^\dagger - ie(\partial_0A_0 - \partial_xA_x - \partial_yA_y - \partial_zA_z)\phi^\dagger - 2ie(A_0\partial_0 - A_x\partial_x - A_y\partial_y - A_z\partial_z)\phi^\dagger \\ -e^2(A_0^2 - A_x^2 - A_y^2 - A_z^2)\phi^\dagger + \frac{\lambda}{2}\phi^\dagger(\phi\phi^\dagger - \eta^2) = 0.\end{aligned} \tag{2.3}$$

Translating this into cylindrical polars, with

$$\partial_x = \cos\theta\partial_r - \frac{\sin\theta}{r}\partial_\theta, \quad \partial_y = \sin\theta\partial_r + \frac{\cos\theta}{r}\partial_\theta,$$

$$A_x = A_r\cos\theta - A_\theta\sin\theta, \quad A_y = A_r\sin\theta + A_\theta\cos\theta,$$

we then substitute and eliminate the trigonometric terms to obtain the scalar equation,

$$(\partial_0^2 - \partial_r^2 - \frac{1}{r}\partial_r - \frac{1}{r^2}\partial_\theta^2 - \partial_z^2)\phi^\dagger - ie(\partial_0A_0 - \partial_rA_r - \frac{1}{r}A_r - \frac{1}{r}\partial_\theta A_\theta - \partial_zA_z)\phi^\dagger - 2ie(A_0\partial_0 - A_r\partial_r$$

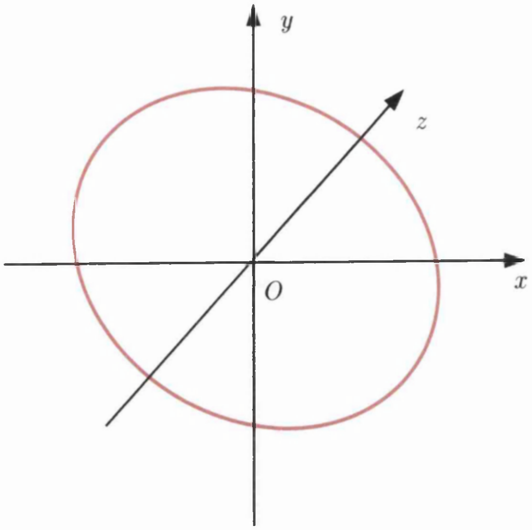

Figure 2.1: The string loop centred about the z-axis

$$-\frac{1}{r}A_\theta\partial_\theta - A_z\partial_z)\phi^\dagger - e^2(A_0^2 - A_r^2 - A_\theta^2 - A_z^2)\phi^\dagger + \frac{\lambda}{2}\phi^\dagger(\phi^\dagger\phi - \eta^2) = 0. \qquad (2.4)$$

First rescaling (2.4) with,

$$\phi^\dagger \rightarrow \eta\phi^\dagger, \quad r^2 \rightarrow \frac{2}{\lambda\eta^2}r^2, \quad A_i \rightarrow \sqrt{\frac{\lambda}{2}}\frac{\eta}{e}A_i, \qquad (2.5)$$

and eliminating terms in A_0, since we are free to choose time-independence for the gauge field, the scalar equation can thus be simplified to become,

$$(\partial_0^2 - \partial_r^2 - \frac{1}{r}\partial_r - \frac{1}{r^2}\partial_\theta^2 - \partial_z^2)\phi^\dagger + (\partial_r A_r + \frac{1}{r}A_r + \frac{1}{r}\partial_\theta A_\theta + \partial_z A_z)\phi^\dagger$$

$$+2i(A_r\partial_r + \frac{1}{r}A_\theta\partial_\theta + A_z\partial_z)\phi^\dagger + (A_r^2 + A_\theta^2 + A_z^2)\phi^\dagger + \phi^\dagger(\phi^\dagger\phi - 1) = 0. \qquad (2.6)$$

The vector field is treated similarly, with

$$\partial_\mu F^{\mu\nu} = \partial_\mu(\partial^\mu A^\nu - \partial^\nu A^\mu) = (\partial_0^2 - \nabla^2)A^\nu - g^{\nu\lambda}\partial_\lambda\partial_\mu A^\mu, \qquad (2.7)$$

so that from (2.2),

$$-\partial_\mu F^{\mu\nu} - ie(\phi^\dagger\partial_\nu\phi - \phi\partial_\nu\phi^\dagger) + 2e^2A_\nu\phi^\dagger\phi = 0, \qquad (2.8)$$

and again stipulating $A_0 = 0$, results in three equations of motion in cartesian coordinates,

$$(\partial_0^2 - \partial_y^2 - \partial_z^2)A_x + \partial_x\partial_y A_y + \partial_x\partial_z A_z - ie(\phi^\dagger\partial_x\phi - \phi\partial_x\phi^\dagger) + 2e^2A_x\phi^\dagger\phi = 0, \quad (2.9)$$

$$(\partial_0^2-\partial_x^2-\partial_z^2)A_y+\partial_y\partial_x A_x+\partial_y\partial_z A_z-ie(\phi^\dagger\partial_y\phi-\phi\partial_y\phi^\dagger)+2e^2A_y\phi^\dagger\phi=0, \quad (2.10)$$

$$(\partial_0^2-\partial_x^2-\partial_y^2)A_z+\partial_x\partial_z A_x+\partial_y\partial_z A_y-ie(\phi^\dagger\partial_z\phi-\phi\partial_z\phi^\dagger)+2e^2A_z\phi^\dagger\phi=0. \quad (2.11)$$

After making the substitutions as before, we obtain in cylindrical polars,

$$(\partial_0^2-\frac{1}{r^2}\partial_\theta^2-\partial_z^2)A_r+\frac{1}{r}\partial_r\partial_\theta A_\theta-\frac{1}{r^2}\partial_\theta A_\theta+\partial_r\partial_z A_z$$

$$-ie(\phi^\dagger\partial_r\phi-\phi\partial_r\phi^\dagger)+2e^2A_r\phi^\dagger\phi=0, \quad (2.12)$$

$$(\partial_0^2-\partial_r^2-\partial_z^2)A_\theta+\frac{1}{r}\partial_r\partial_\theta A_r-\frac{1}{r^2}\partial_\theta A_r-\frac{1}{r}\partial_r A_\theta+\frac{1}{r^2}A_\theta+\frac{1}{r}\partial_\theta\partial_z A_z$$

$$-\frac{ie}{r}(\phi^\dagger\partial_\theta\phi-\phi\partial_\theta\phi^\dagger)+2e^2A_\theta\phi^\dagger\phi=0, \quad (2.13)$$

$$(\partial_0^2-\partial_r^2-\frac{1}{r^2}\partial_\theta^2)A_z-\frac{1}{r}\partial_r A_z+\partial_r\partial_z A_r+\frac{1}{r}\partial_z A_r+\frac{1}{r}\partial_\theta\partial_z A_\theta$$

$$-ie[\phi^\dagger\partial_z\phi-\phi\partial_z\phi^\dagger]+2e^2A_z\phi^\dagger\phi=0. \quad (2.14)$$

The same rescaling terms are used as for the scalar equations which introduces an additional λ. The coupling constants e and λ may be given arbitrary values, and this fact can be used in justification for setting $e^2/\lambda = 1/2$, thus simplifying the equations by eliminating both. The three rescaled equations of motion finally become,

$$(\partial_0^2-\frac{1}{r^2}\partial_\theta^2-\partial_z^2)A_r+\frac{1}{r}\partial_r\partial_\theta A_\theta-\frac{1}{r^2}\partial_\theta A_\theta+\partial_r\partial_z A_z$$

$$-i(\phi^\dagger\partial_r\phi-\phi\partial_r\phi^\dagger)+2A_r\phi^\dagger\phi=0, \quad (2.15)$$

$$(\partial_0^2-\partial_r^2-\partial_z^2)A_\theta+\frac{1}{r}\partial_r\partial_\theta A_r-\frac{1}{r^2}\partial_\theta A_r-\frac{1}{r}\partial_r A_\theta+\frac{1}{r^2}A_\theta+\frac{1}{r}\partial_\theta\partial_z A_z$$

$$-i(\phi^\dagger\partial_\theta\phi-\phi\partial_\theta\phi^\dagger)+2A_\theta\phi^\dagger\phi=0, \quad (2.16)$$

$$(\partial_0^2-\partial_r^2-\frac{1}{r^2}\partial_\theta^2)A_z-\frac{1}{r}\partial_r A_z+\partial_r\partial_z A_r+\frac{1}{r}\partial_z A_r+\frac{1}{r}\partial_\theta\partial_z A_\theta$$

$$-i(\phi^\dagger\partial_z\phi-\phi\partial_z\phi^\dagger)+2A_z\phi^\dagger\phi=0. \quad (2.17)$$

Stipulating that the loop is both circular and symmetrical with respect to the z-axis, means that we can now set $\partial_\theta() = 0$, $A_\theta = 0$, and consequently (2.16) is satisfied. The remaining equations (2.6), (2.15), and (2.17) then become,

$$(\partial_0^2-\partial_r^2-\frac{1}{r}\partial_r-\partial_z^2)\phi^\dagger+i(\partial_r A_r+\frac{1}{r}A_r+\partial_z A_z)\phi^\dagger+2i(A_r\partial_r+A_z\partial_z)\phi^\dagger$$

$$+(A_r^2 + A_z^2)\phi^\dagger + \phi^\dagger(\phi^\dagger\phi - 1) = 0, \tag{2.18}$$

$$\partial_0^2 A_r - \partial_z^2 A_r + \partial_r\partial_z A_z - i(\phi^\dagger\partial_r\phi - \phi\partial_r\phi^\dagger) + 2A_r\phi^\dagger\phi = 0, \tag{2.19}$$

$$\partial_0^2 A_z - \partial_r^2 A_z + \partial_r\partial_z A_r + \frac{1}{r}\partial_z A_r - \frac{1}{r}\partial_r A_z - i(\phi^\dagger\partial_z\phi - \phi\partial_z\phi^\dagger) + 2A_z\phi^\dagger\phi = 0. \tag{2.20}$$

The scalar field is complex, so for numerical calculation it is convenient to eliminate the complex terms to obtain a real system of equations by putting $\phi = \phi_1 + i\phi_2, \quad \phi^\dagger = \phi_1 - i\phi_2$. This is shown in an Appendix.

In order to set the initial Higgs profile in the numerical code, we can use a similar Ansatz to that for the 1-dimensional Nielsen-Olesen vortex solution, but now extended to a 2-dimensional lattice. This is done by letting the loop pass through the the centre of a square lattice, as in Figure 2.2, and by setting the loop radius $r \to \infty$. The fields can then be calculated radially round the string, with radius ρ and polar angle ξ, to distinguish these components from those of the loop. Applying the Ansatz, we then have $A_\rho = 0, \quad A_\xi = A_\xi(\rho)$ and $\phi = f(\rho)e^{i\xi t}$, where $t = \pm 1$ is the phase of the Higgs field. The method is explained in detail in Chapter 3, pages 50-51.

2.2 *Solving the Equations Numerically*

As the equations of motion on the loop cannot be solved analytically, a program code is used to obtain a numerical solution. This employs the central difference method on the second derivatives on an $l \times m$ lattice. Figure 2.2 shows the loop passing through the centre of the lattice, while still centred on the z-axis as before. The radius r consists of two parts, from the origin of the loop, O, to the edge of the lattice plus the distance to the centre of the lattice.

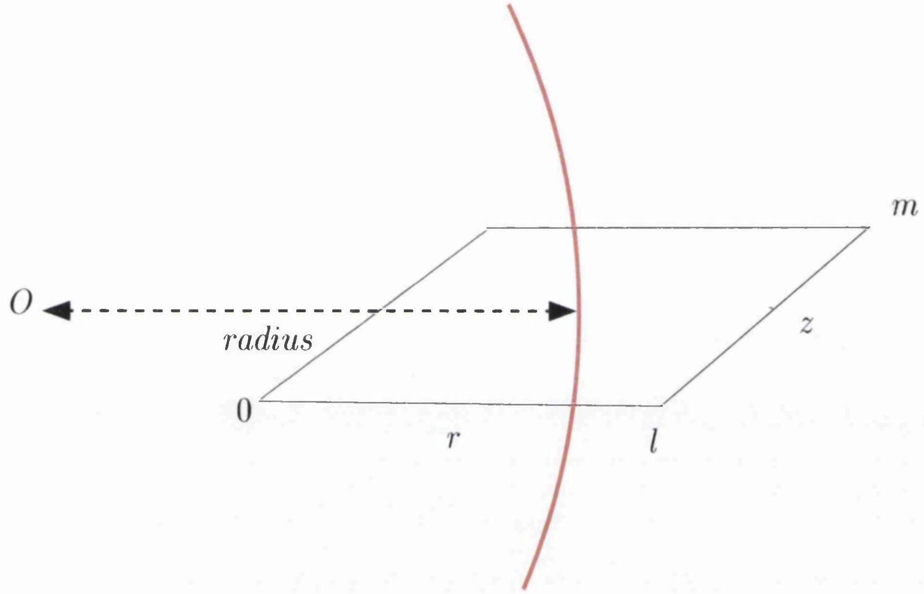

Figure 2.2: The string loop passing through the centre of an $l \times m$ lattice

Before starting to calculate on the lattice, we need to define the parameters that will be used to determine the output from the code. The method is essentially the same for both the bosonic and fermionic equations, so the same parameters apply. These are:

the electromagnetic coupling constant, e and the scalar coupling constant, λ. Although both have been eliminated at this point, they could be assigned a different value if required;

the scalar-fermion mass coupling constant, g;

the lattice step sizes, $\Delta r, \Delta z$, determine the distance in terms of radius units between lattice points - due to scaling, these units are dimensionless;

the time step Δt;

a numerical damping factor, γ, is also required to control the fields, which can otherwise oscillate indefinitely. This is applied when the fields are updated at each point as the code is run. The damping acts on the acceleration for each of the components ϕ_{re}, ϕ_{im}, A_r, A_z so that, for example,

$$\partial_0\phi_{re} = \gamma \times \partial_0\phi_{re} + \Delta t \times \partial_0^2\phi_{re}. \tag{2.21}$$

Thus the fields are undamped when $\gamma = 1$, and the acceleration is slowed for $\gamma < 1$. In the case of the bosonic fields, a relatively light damping factor of 0.99 is sufficient.

A 100×100 lattice is chosen for calculating speed and is large enough for general use, but a 200×200 lattice can be used to check accuracy if required, for instance if more grid space is required for the gauge fields to evolve, or if more reference points are needed very close to the string where the profile gradient is steepest.

2.2.1 *The Bosonic Fields on a Straight String*

The analytical equations are specifically designed for a loop, but by making the radius large enough we obtain a straight- string approximation; to do this in the code the radius is put at 10^{20}, effectively eliminating any terms with $1/r$ and $1/r^2$.

With the straight-string configuration, the string passes through the centre of the lattice, so the fields need to be calculated radially, with the radius on the lattice defined as,

$$\texttt{radius}_{lattice} = \sqrt{}((l - r_{max}/2)^2 + (m - r_{max}/2)^2 + a), \tag{2.22}$$

where a is an arbitrarily small number to prevent zero denominators in the terms containing 1/r in the initial phi profile, and r_{max} is the maximum size chosen for the lattice.

At this stage the conditions on the lattice boundary must be considered; Dirichelet boundary conditions do not give a realistic representation at the edge of the grid, since the fields do not suddenly become zero there, so von Neumann boundary conditions are used, which make the derivative zero at the edge, allowing the fields to continue more realistically beyond the lattice. The implications of this are shown by the gauge field which falls off as $1/r$, which means its derivative falls off as $1/r^2$. The von Neumann boundary conditions force something which should be $1/r^2$ to zero on a lattice with a typical unit of 5 (if $\Delta_r = 0.2$), so that rather than setting something which should be 0.2 to zero, $1/r^2 = 0.04$ becomes zero instead.

We are now ready to plot the first straight string profiles and Figure 2.3 shows the r and z-axis cross-sections of the Higgs and magnetic field profiles on both lattices. The Higgs field is compared with the 1-dimensional profile already obtained, Figure 1.12. The magnetic field is the curl, in this case $\partial_z A_r - \partial_r A_z$, since symmetry has eliminated the A_θ terms. Without damping, the fields would continue to oscillate steadily, but a damping factor of 0.99 reduces the oscillations to zero after approximately 500 time-steps, and the fields continue evolving quite quickly thereafter to become completely settled after 1800 time-steps, with no further change over time. Of note is the very good coincidence between all the profiles. This is particularly important to find in the case of these physical quantities, which are gauge invariant, and confirms the correctness of the code.

At this point the gauge fields can be introduced. They are treated separately, because they are not gauge-invariant and are therefore more likely to reveal time-related anomalies, such as drifting. Figure 2.6 and Figure 2.7 compare the gauge field cross-sections on the two lattices at 2000 timesteps, and again after 25000 timesteps, when the divergence further from the string has noticeably increased. This effect soon stops increasing, however, and is caused by the larger lattice allowing more freedom for the fields to relax, rather than by any drift in the gauge field. This is supported by the very good coincidence of all profiles close to the string, even after long time spans. On a sufficiently large lattice the gauge field would approach zero,

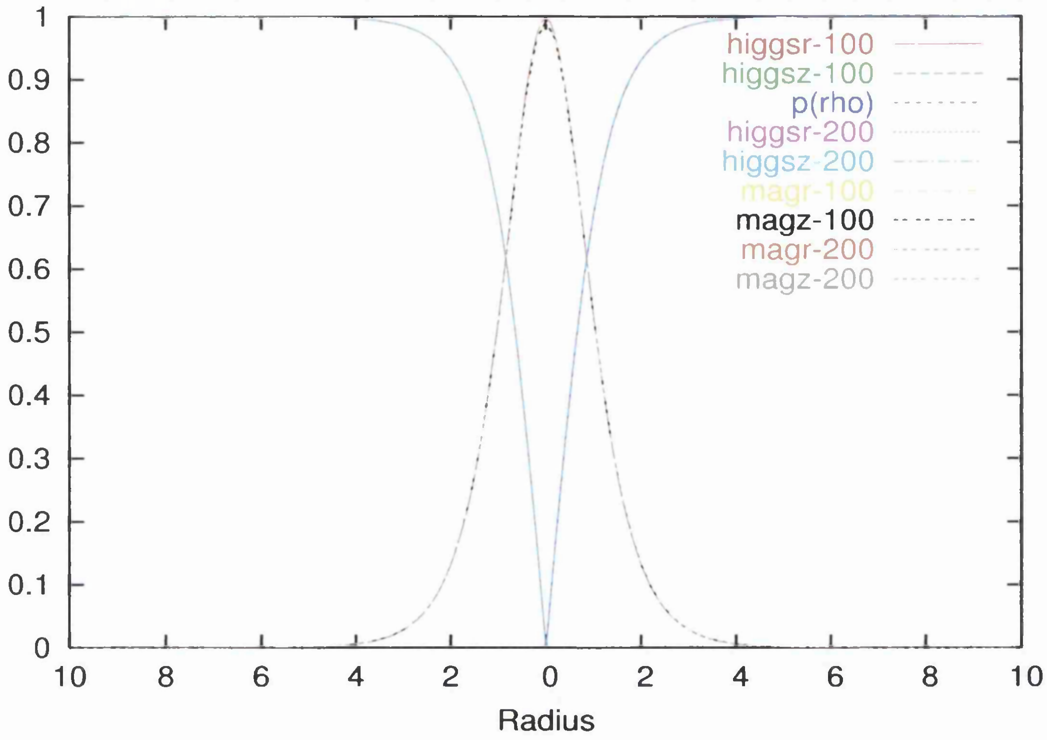

Figure 2.3: The scalar and magnetic field r-z axis cross-sections compared on lattices of 100×100 and 200×200, together with the 1-dimensional solution $p(\rho)$. The coincidence of the cross-sections and the profiles on both lattices is very good at all radii. With $\Delta t = 0.01$ in both cases, about 1800 time-steps are needed for the fields to fully evolve. The lack of coincidence at the apex of the magnetic field on the two lattices reflects the fewer plotting points available very close to the string on the coarser lattice.

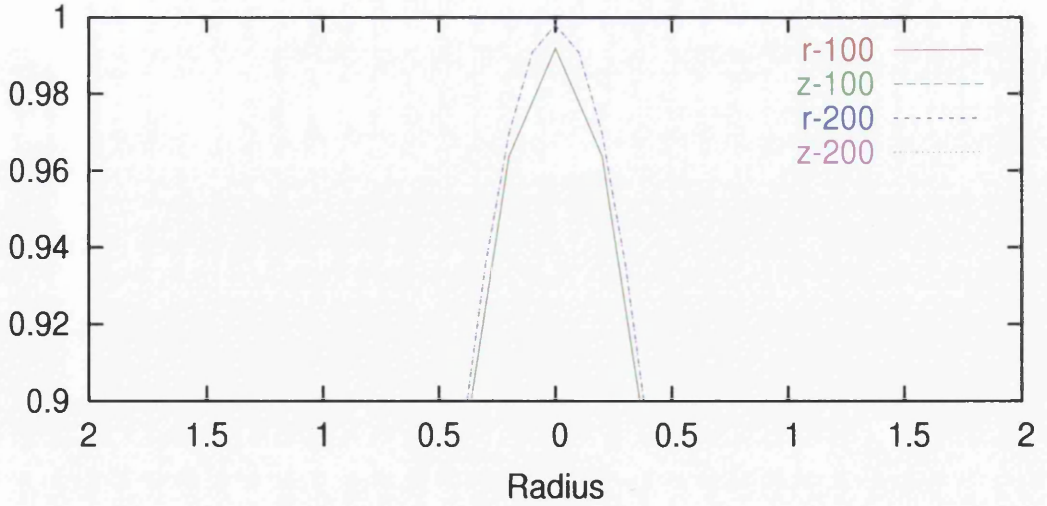

Figure 2.4: The magnetic field cross-sections on the two lattices with the apex enlarged to show the difference at that point on the two lattices due to the larger number of plotting points on the larger lattice.

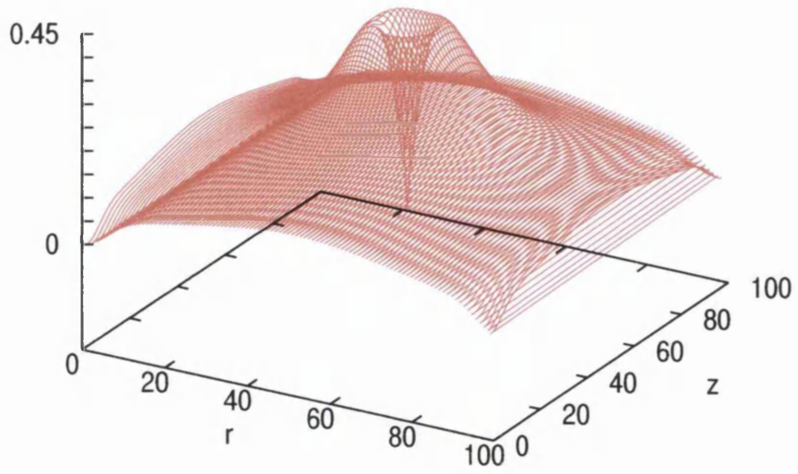

Figure 2.5: The 2-dimensional gauge field as a 3-dimensional projection. At the corners the greater distance from the string illustrates how the field continues to approach zero.

but as already discussed the boundary conditions are forcing the gradient to zero at the edge, so preventing the fields reaching zero. For each lattice the cross-sections are otherwise identical.

2.2.2 *The Bosonic Fields on a Loop*

We next consider the behaviour of the bosonic fields on a loop of finite radius as the radius is gradually reduced. If the radius is large, say $r > 10,000$, it is difficult to detect any shift in the profiles without a very large number of timesteps, and even then any asymmetry along the r-axis is negligible. With $r \approx 1000$ the displacement from the lattice centre is small but noticeable. It is more interesting to reduce the radius to the point where the loop shrinks by a full lattice space. The effect of this with the radius now reduced to 100, is shown before it has recentered in Figure 2.9 and Figure 2.10. The asymmetry in the r-axis gauge cross-section is starting to become very pronounced.

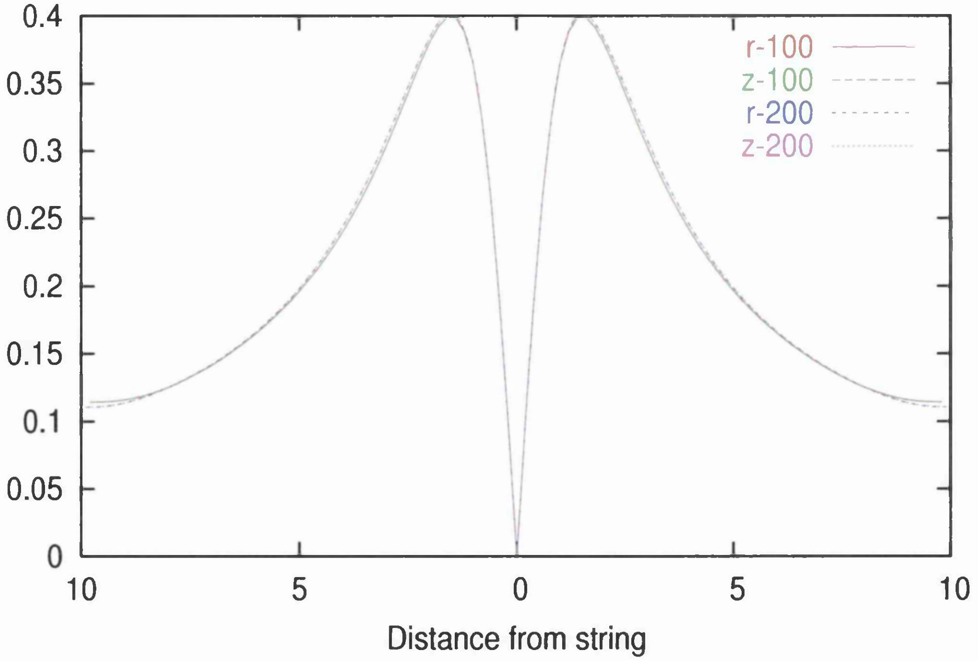

Figure 2.6: The straight string gauge field cross-sections compared on the two lattices after a minimal evolution time of 1800 time-steps. The alignment is very good close to the string, but a small deviation between the lattices is apparent towards the boundary.

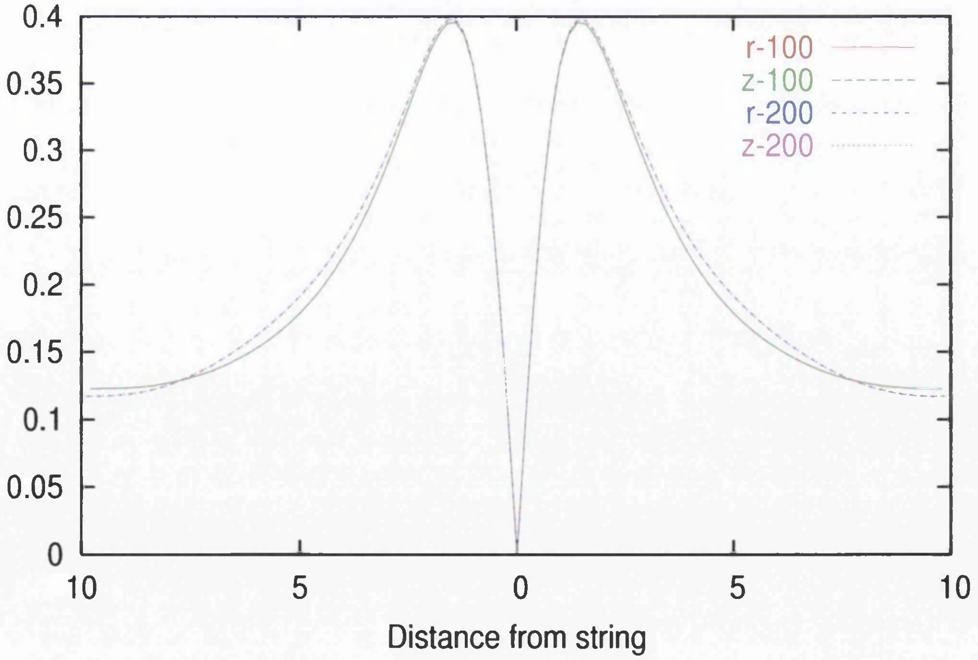

Figure 2.7: The straight string gauge field cross-sections compared on the two lattices after 25000 time-steps. The profiles remain well aligned close to the string, but there is a noticeable increase in the deviation between the two lattices as the distance from the string increases.

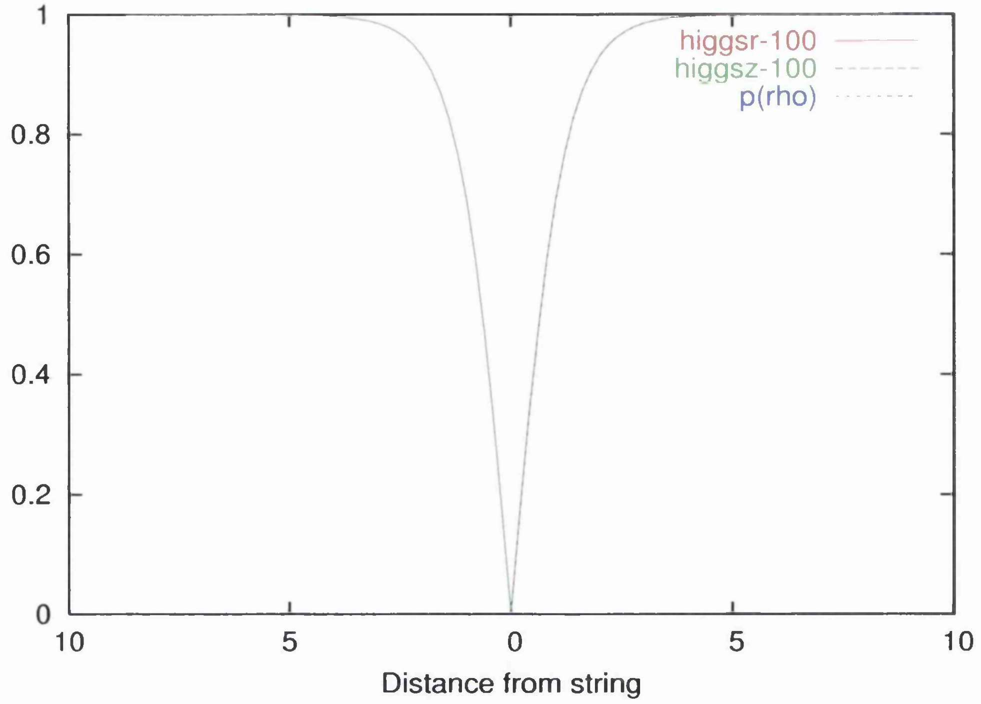

Figure 2.8: The Higgs r and z-axis cross-sections compared with the 1-dimensional profile at a radius of 10,000. At this large radius the profiles are identical.

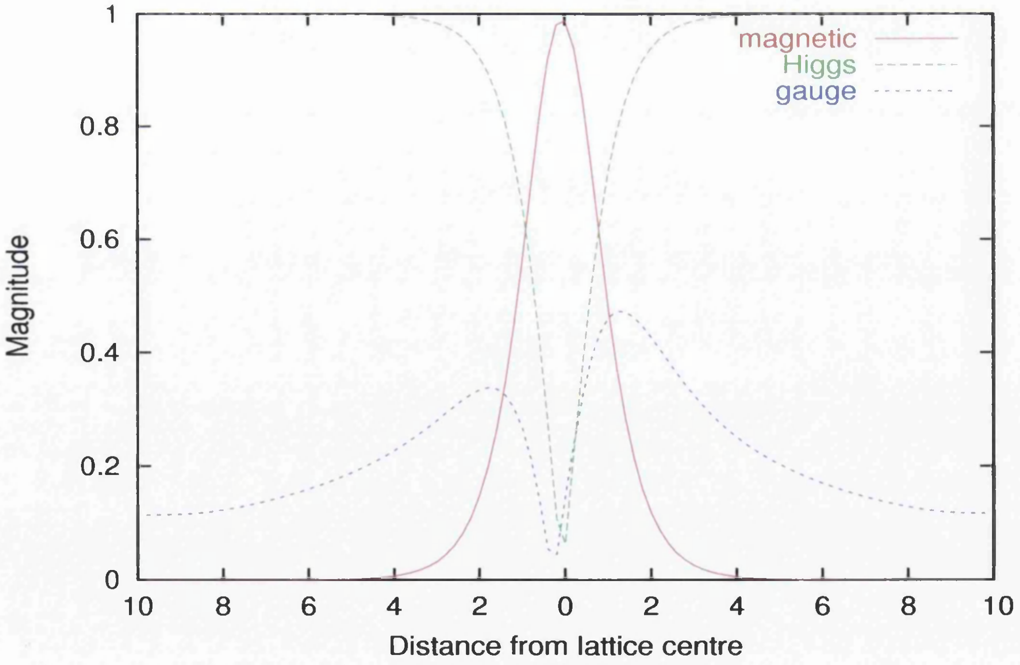

Figure 2.9: The scalar and magnetic profiles on a loop of radius 100 after enough time has elapsed for them to fully evolve. The string is between lattice points. The gauge field is shown by the dotted line, showing the marked distortion that occurs in the radial direction.

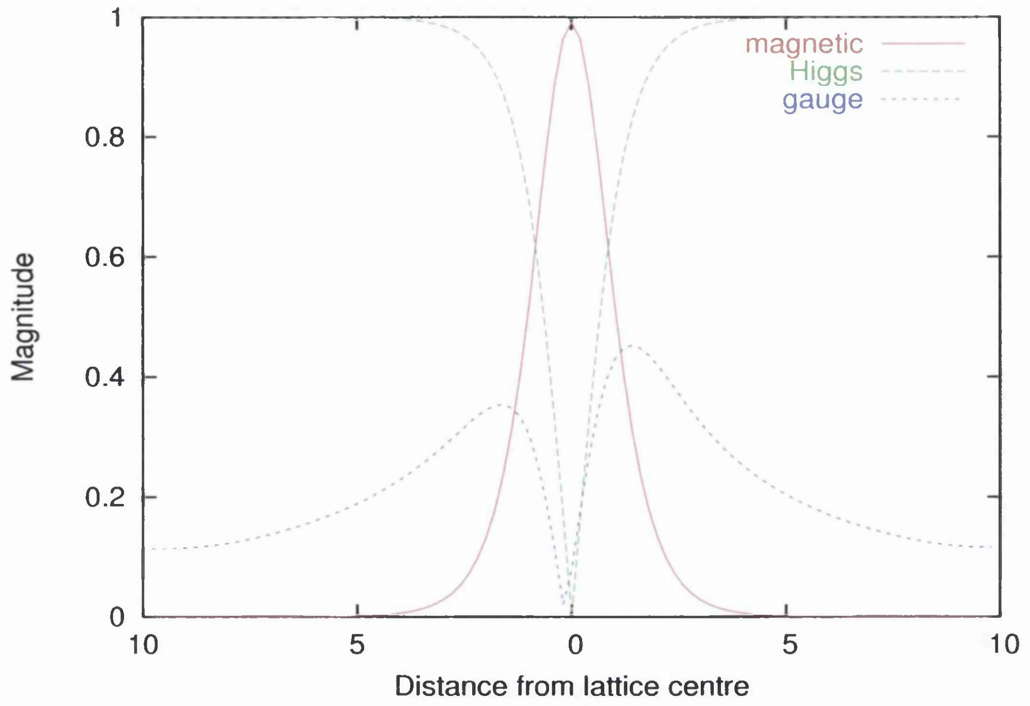

Figure 2.10: The scalar and magnetic profiles at a radius of 100 after further time has elapsed to allow the fields to recentre. The gauge field does not recenter with them, but at a different point in the cycle.

If the movement towards the loop centre is not corrected, the string would eventually leave the lattice altogether. The code prevents this happening by recentering the lattice on the string each time a full lattice space is reached. The stepsize is 0.2, so in terms of the radius units each shift of the lattice to recentre the string reduces the radius by 0.2. As the lattice is recentred there is a point at which its inner edge reaches the origin of the loop after which the string starts moving along the lattice as the loop continues to shrink. This can continue until the string reaches the first lattice point, when its radius is 0.2, in the case of the 100x100 lattice, or 0.1 for the 200x200 lattice.

At larger loop radii there is no discernible distortion in the sections of the Higgs and magnetic fields taken in the radial direction, but this is not the case with the gauge field which is showing significant radial distortion even at a radius of 100, as in Figure 2.10. This effect increases rapidly as the radius decreases, and for clarity the gauge profile will not be shown in future. As a non-physical quantity it is of less

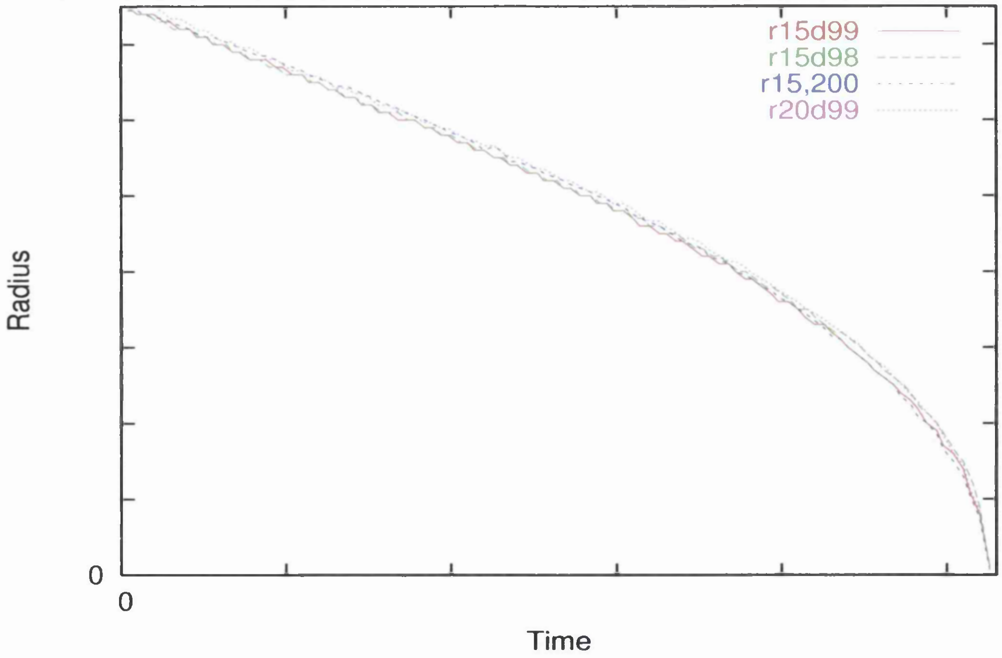

Figure 2.11: The reducing radius as a loop contracts from 20 to 0.2 (mauve) is compared with (a) reducing the radius from 15 to 0.2 (red), (b) repeating the latter on a 200 × 200 lattice (blue), each with a damping factor of 0.99, and (c) (green) increasing the damping to 0.98 on a 100 × 100 lattice.

importance than the gauge-invariant quantities, and it is the behaviour of the latter as the radius becomes very small, that is of more interest. This radial distortion is to be expected at small radius, due to the asymmetry between the inside and outside of a loop, and the gauge field happens to be much more sensitive to decreasing radius.

Rather than taking spot readings at a succession of decreasing radii, it is more realistic to allow the loop to shrink from an intermediate value, say 20, to the required radius and then view the results. The next stage will determine how small this starting radius can be.

Figure 2.11 compares the radius shrinking over time from starting values of 20 and 15 down to an end value of 0.2, and for different damping values and lattice sizes. These results are consistent enough to justify the use of a starting radius of 15 on a 100×100 lattice, thereby decreasing the program runtime by a factor of about 2. This starting radius will be used in future unless otherwise stated.

The main reason for shrinking the loop to extremely small radius is in order to

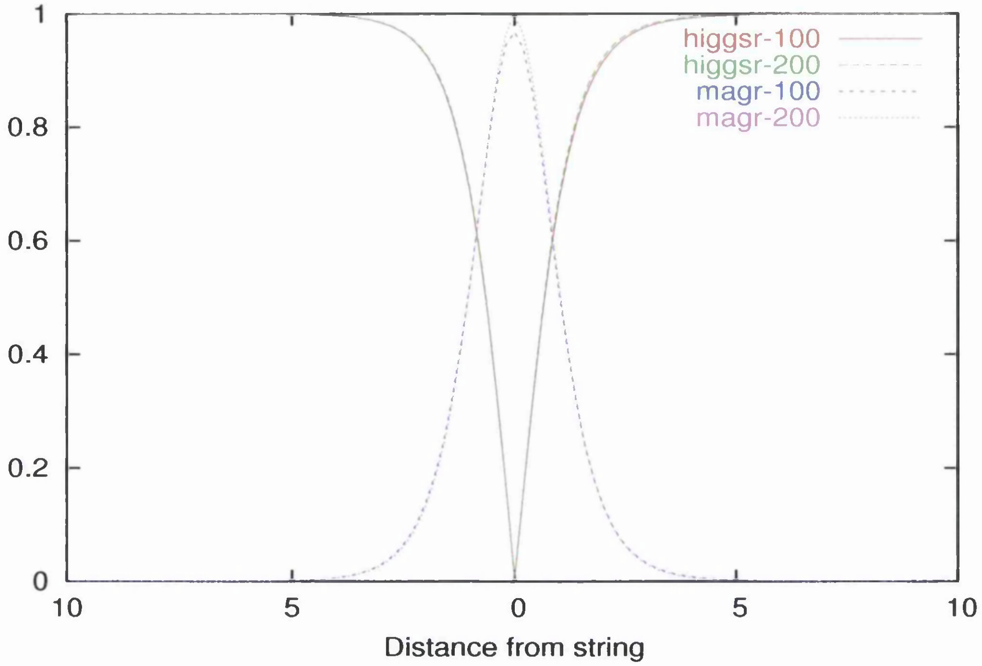

Figure 2.12: The scalar and magnetic field r-axis cross-sections on a loop of radius 10, just as the lattice edge has reached the loop origin, with the string still at the centre of the lattice. The profiles coincide quite well on both lattices, but a small radial distortion is starting to become evident on the 100x100 lattice.

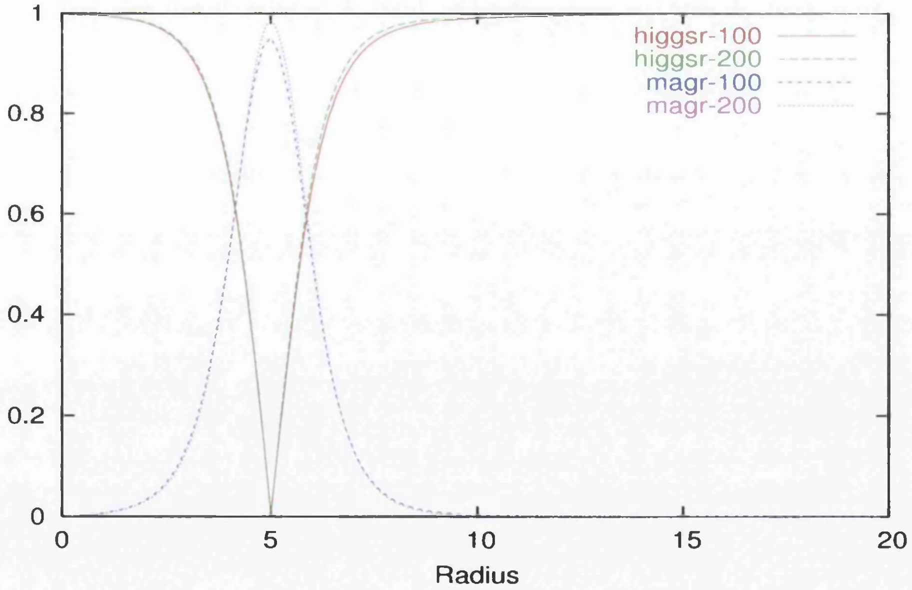

Figure 2.13: The scalar and magnetic field r-axis cross-sections compared on the two lattices on a loop contracted from a radius of 15 down to a radius of 5. The profiles on the finer lattice are more accurate, with the Higgs profile on the 200x200 lattice remaining very close to the 1-dimensional profile (which is not shown). The radial displacement is only noticeable on the 100x100 lattice.

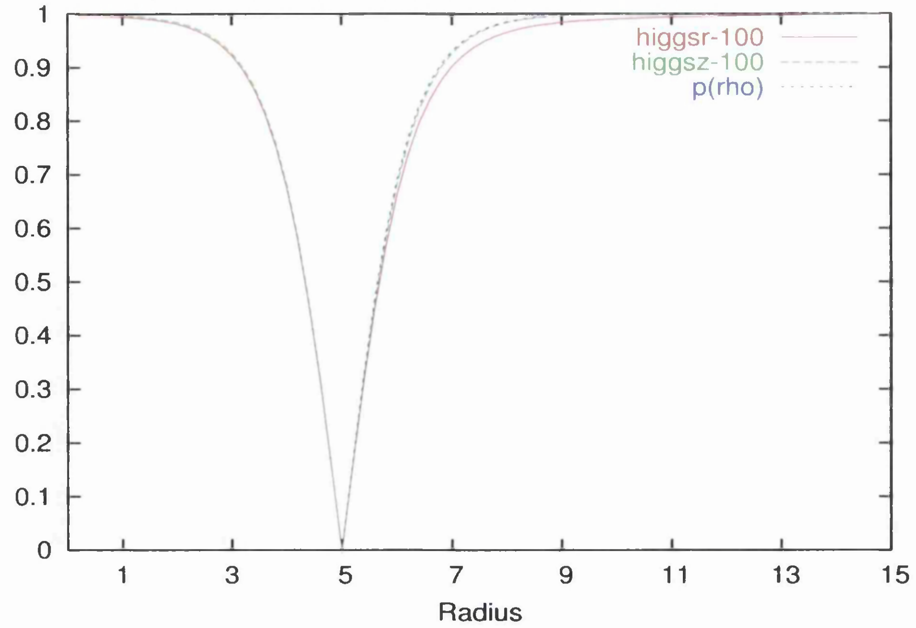

Figure 2.14: The scalar field r and z cross-sections at a radius of 5 compared with the abelian-Higgs 1-dimensional profile from Figure 1.12. The deviation along the r-axis is starting to show away from the core, while the z-section and the 1-dimensional profile are identical. This result may be compared with the same profiles at large radius, Figure 2.8, and confirms that the displacement is a radial effect.

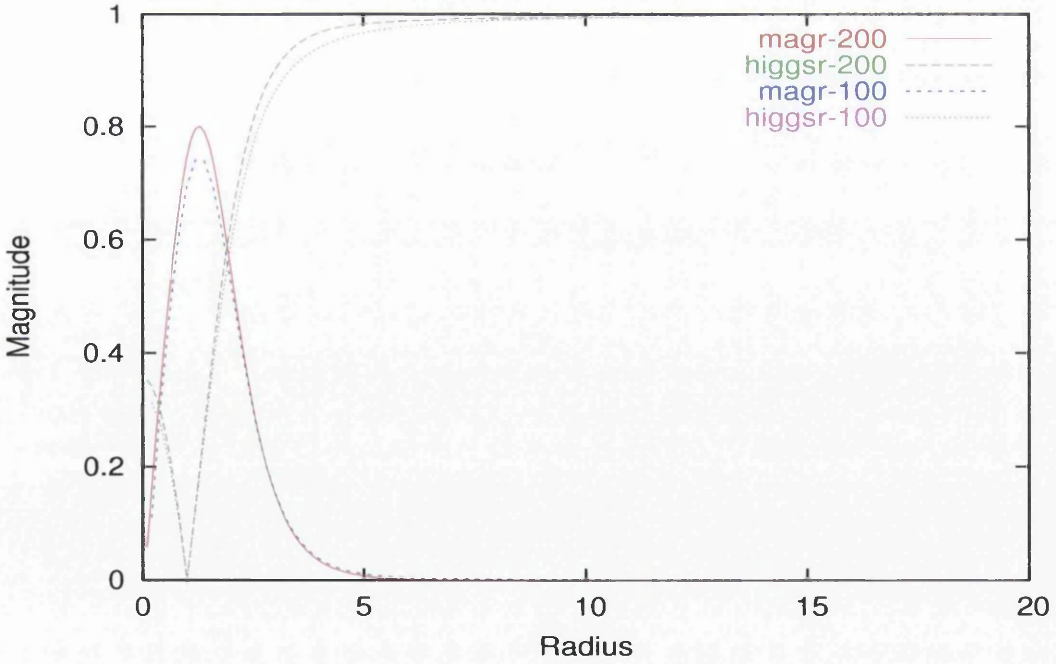

Figure 2.15: The scalar and magnetic fields on a loop contracted from a radius of 15 down to a radius of 1. The radial displacement is very slowly increasing, while the magnitude of the magnetic field is noticeably decreasing.

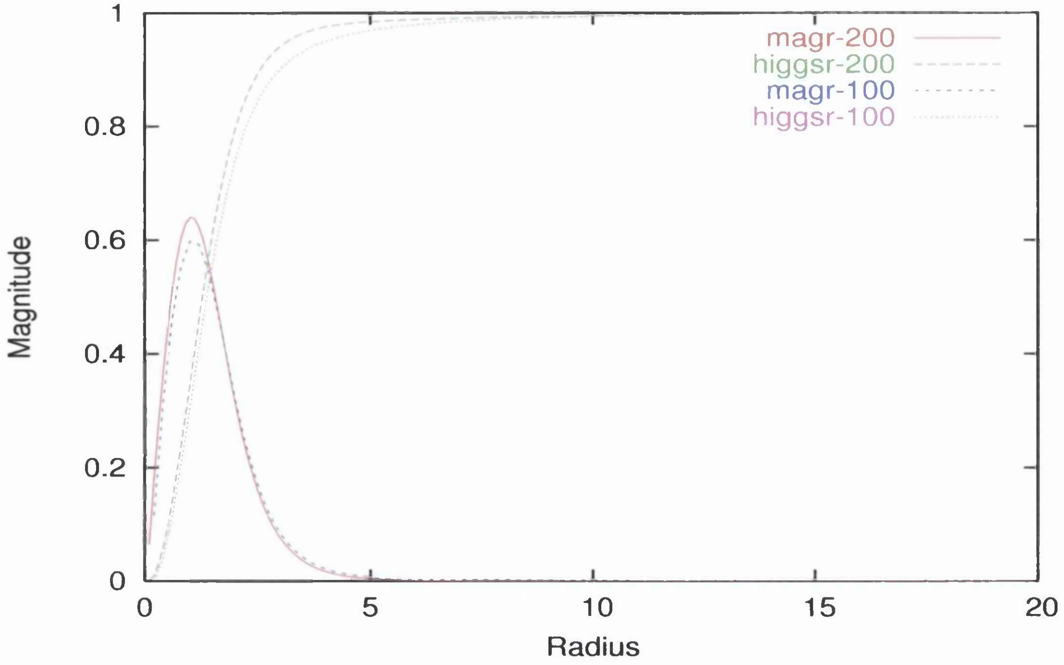

Figure 2.16: The scalar and magnetic fields on a loop contracted from a radius of 15 down to the minimum radius of 0.2 for the 100x100 lattide and 0.1 for the 200x200 lattice. In each case the radius corresponds to one lattice space from the origin.

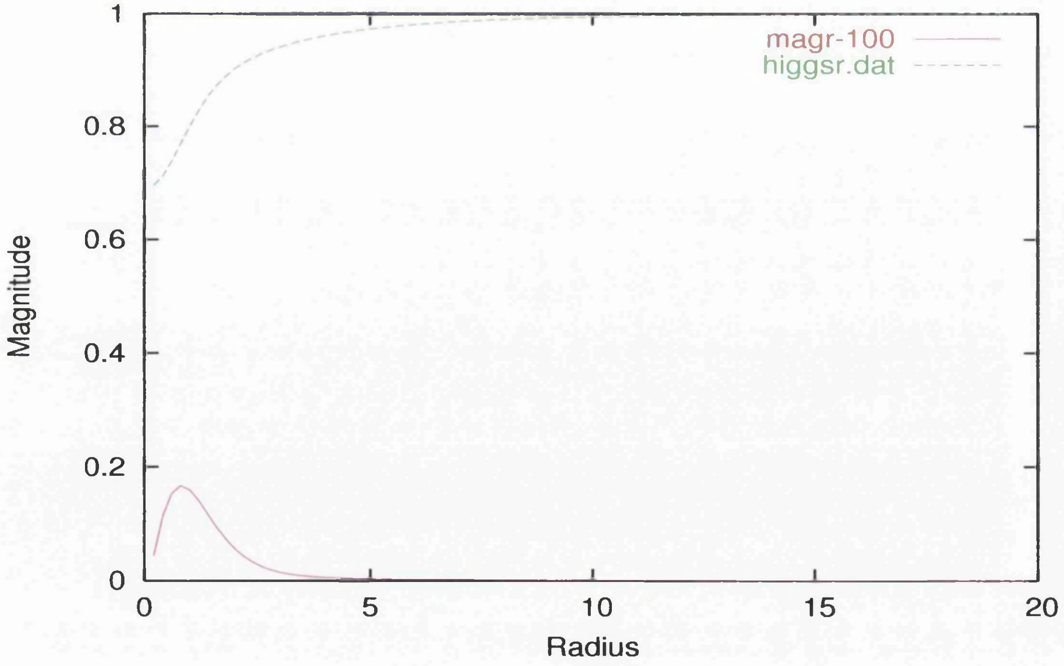

Figure 2.17: If the bosonic fields continue to run after the minimum radius, they rapidly decay and take on their vacuum values, as the loop effectively vanishes.

locate and observe the behaviour of the fermionic zero modes, which forms the subject of the next chapter, but we first need to ascertain what happens to the bosonic fields as the radius approaches its minimum value on the lattice.

Figures 2.12-2.17 illustrate how the magnetic and Higgs fields remain basically unchanged, the main differences in the profiles being due to the influence of the decreasing radius and the decrease in magnitude of the magnetic field. A radial displacement is only just discernible at a radius of 12.4, which is further justification for using a starting radius of 15. Differences between the two lattices increase as the radius becomes very small, particularly when comparing the r-axis cross-sections with the 1-dimensional profile.

Chapter 3

A Review of Fermionic Straight-String Solutions

3.1 *Scalar-Fermion Interactions*

With the bosonic background fields now established, the next stage is to deduce the fermionic mass terms analytically, but as a preliminary to this we start with the form of the Dirac lagrangian used by Jackiw and Rossi [2] to include the scalar-fermion interactions in the complete fermion-vortex system. They demonstrated, with the Lagrangian reduced to 2-dimensional form for a straight string, that there are exactly $|n|$ normalisable zero energy solutions to the Dirac equation which allow massless fermions to propagate at the speed of light, where n is the Higgs field winding number on the string [2][33]. These zero modes arise because the winding of the Higgs field on the string core results in the fermion mass terms becoming zero. Away from the core, the Higgs field takes on a non-vanishing value. Later in this chapter the local fermionic straight-string equation will be derived from the more general case for a loop, but for now we obtain the 1-dimensional solution using the equations of motion from Jackiw and Rossi, in which the gauge fields have been suppressed, thus giving a global result, which can then be compared with the solution derived later.

The full Dirac lagrangian is [2],

$$L = \bar{\Psi}(\gamma^{\mu}[i\partial_{\mu} - eA_{\mu}])\Psi - \frac{1}{2}ig\phi\bar{\Psi}\Gamma\Psi^{c} + \frac{1}{2}ig^{*}\phi^{*}\bar{\Psi}^{c}\bar{\Gamma}\Psi, \qquad (3.1)$$

with e the electric charge of the fermion and g the scalar coupling constant,

3.1.1 *The Global Straight-String Solution*

From (3.1), the 2-dimensional Dirac equation has the form[2],

$$i\partial_t \Psi = \alpha \cdot (\mathbf{p} - e\mathbf{A})\Psi - g\phi\sigma^2\Psi^*, \tag{3.2}$$

where $\mathbf{p} = \frac{1}{i}\nabla$, and α is the pair of Pauli matrices (σ^1, σ^2).

By defining the two-component spinor

$$\psi = \begin{pmatrix} e^{(1/2)\int_0^r \partial_\rho A(\rho)} \psi_U \\ e^{-(1/2)\int_0^r \partial_\rho A(\rho)} \psi_L \end{pmatrix}, \tag{3.3}$$

the gauge potential can be eliminated from the zero energy equations,

$$0 = \alpha \cdot (\mathbf{p} - e\mathbf{A})\psi - g\phi\sigma^2\psi^*, \tag{3.4}$$

so that they decouple,

$$e^{i\theta}\left(\partial_r + \frac{i}{r}\partial_\theta\right)\psi_U + gfe^{in\theta}\psi_U^* = 0, \tag{3.5}$$

$$e^{-i\theta}\left(\partial_r - \frac{i}{r}\partial_\theta\right)\psi_L - gfe^{in\theta}\psi_L^* = 0. \tag{3.6}$$

A two-phase Ansatz separates the angular dependence and defines the upper and lower components of ψ,

$$\psi_U = U_U(r)e^{im\theta} + V_U(r)e^{i(n-1-m)\theta} \tag{3.7}$$

$$\psi_L = U_L(r)e^{-im\theta} - V_L(r)e^{i(n+1+m)\theta}, \tag{3.8}$$

where $m =$ is an integer $\neq \frac{1}{2}n - \frac{1}{2}$. The first-order equations can then be derived,

$$\left(\partial_r - \frac{m}{r}\right) V_u + gfU_u^* = 0, \tag{3.9}$$

$$\left(\partial_r - \frac{n-1-m}{r}\right) U_u + gfV_u^* = 0. \tag{3.10}$$

We obtain U_u and V_u in terms of U_u^* and V_u^*, where the subscripts indicate the upper spinor components, n is the winding number of the Higgs field and m is the angular dependence of the spinors. Putting $U^* = u_u^*$, gives the second-order equation in u_u^*,

$$\left(\partial_r - \frac{n-1-m}{r}\right)\left[-\frac{1}{gf}\left(\partial_r - \frac{m}{r}\right)u^*\right] + gfu^* = 0, \tag{3.11}$$

$$\Rightarrow -u^{*\prime\prime} + \left(\frac{f'}{f} + \frac{n-1}{r}\right) u^{*\prime} - \left(\frac{f'}{f}\frac{m}{r} + \frac{m}{r^2}(n-m)\right) u^* + g^2 f^2 u^* = 0. \tag{3.12}$$

In the particular case with n=1, m=0, this reduces to,

$$-u^{*\prime\prime} + \frac{f'}{f} u^{*\prime} + g^2 f^2 u^* = 0. \tag{3.13}$$

Using the same method for v_u^*,

$$\left(\partial_r - \frac{m}{r}\right)\left[-\frac{1}{gf}\left(\partial_r - \frac{n-1-m}{r}\right) v^*\right] + g^2 f^2 v^* = 0 \tag{3.14}$$

results in the second-order equation,

$$-v^{*\prime\prime} + \left(\frac{f'}{f} + \frac{n-1}{r}\right) v^{*\prime} - \frac{n-1-m}{r}\left(\frac{f'}{f} + \frac{1+m}{r}\right) v^* + g^2 f^2 v^* = 0. \tag{3.15}$$

Again with n=1, m=0, this reduces to,

$$-v^{*\prime\prime} + \frac{f'}{f} v^{*\prime} + g^2 f^2 v^* = 0. \tag{3.16}$$

The equivalent second-order equations for the lower components are similarly derived from the first-order equations,

$$\left(\partial_r - \frac{m}{r}\right) V_L + gfU_L^* = 0, \tag{3.17}$$

$$\left(\partial_r + \frac{n+1+m}{r}\right) U_L + gfV_L^* = 0. \tag{3.18}$$

With n=1, m=0, these result in the pair of equations,

$$-u^{*\prime\prime} + \left(\frac{f'}{f} - \frac{2}{r}\right) u^{*\prime} + g^2 f^2 u^* = 0, \tag{3.19}$$

$$-v^{*\prime\prime} + \left(\frac{f'}{f} - \frac{2}{r}\right) v^{*\prime} + \frac{2}{r}\left(\frac{f'}{f} + \frac{1}{r}\right) v^* + g^2 f^2 v^* = 0. \tag{3.20}$$

In general, we would expect one regular and one diverging solution, internally and externally, while with a zero mode there are two internal solutions, guaranteeing a solution.

For very small r, we use the fact that $f'/f = 1/r$ and $u^*, v^* = r^p$, for some power p. Substituting $\partial_r r^p = pr^p/r$, the second-order equations become (a) for u_u^*:

$$\begin{aligned}\left(\frac{1}{r}\left(\frac{p}{r} - \frac{m}{r}\right) - \left[\frac{p^2}{r^2} - \frac{p}{r^2} - \frac{pm}{r^2} + \frac{m}{r^2} - \frac{(n-1-m)}{r^2}p\right]\right) r^p \\ - \left(\frac{m(n-1-m)}{r^2}\right) r^p + O(r^{p+2}) = 0,\end{aligned} \tag{3.21}$$

multiplying by r^2 and with n=1, results in the pair of solutions $p = (0, 2)$ when $m = 0$, and therefore a zero-mode solution. The global solution is shown in Fig.3.1.

The lower-component solutions are obtained in the same way, but do not result in coinciding solution sets. There is therefore no zero mode solution for the lower components, which are set at zero.

For the straight string the Lagrangian may be reduced to two-dimensional form from the start, but for a loop the full form is not developed until much further on, when for reasons of symmetry, the analytical working can be continued in 2+1 dimensions.

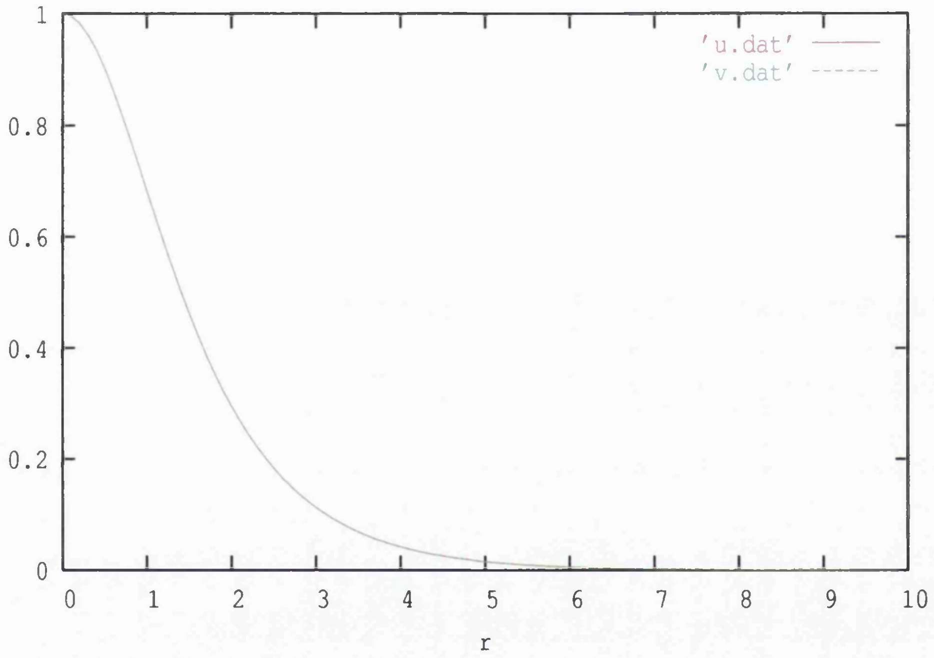

Figure 3.1: The global 1-dimensional fermionic solutions for a straight string

3.1.2 *The Straight-String Limit*

The local fermionic solution for the straight string can be obtained directly from the matrix (4.49), by making the radius of the loop very large, effectively $r \to \infty$, thus allowing the elimination of any terms containing $1/r$. The motivation for this solution is to provide an initial condition for numerically solving the fermionic equations to be derived in chapter 4. With this condition the equations are also made time-independent. We then convert to cylindrical polars by considering the straight string at the centre of an azimuthal gauge field, with a new polar angle ξ. The matrix can then be expressed in terms of a radial component A_ρ and an angular component A_ξ. Setting $A_\rho = 0$ and $A_\xi = -\alpha/er$, allows the derivation of a 1-dimensional fermionic equation of the same form obtained originally for the bosonic fields in the Nielsen-Oleson vortex solution.

Letting the radius of the loop $r_0 \to \infty$, and setting $\partial_0 = 0$ in the limit, the matrix (4.49)

$$\begin{pmatrix} \partial_0^2 - \left(\partial_r^2 + \frac{1}{r}\partial_r + \partial_z^2\right) + e^2(A_r^2 + A_z^2) - ie(\partial_z A_z + \partial_r A_r + \frac{1}{r}A_r) - 2ieA_z\partial_0 + \frac{ie}{\phi}(\partial_z\phi A_z + \partial_r\phi A_r) + \frac{1}{\phi}[(\partial_z\phi\partial_z + \partial_r\phi\partial_r) - \partial_z\phi\partial_0] + |g\phi|^2 & 2ie[(A_z\partial_r - A_r\partial_z) - A_r\partial_0 + \frac{1}{r}A_z] - ie(\partial_z A_r - \partial_r A_z) + \frac{ie}{\phi}(\partial_z\phi A_r - \partial_r\phi A_z) + \frac{1}{\phi}[(\partial_z\phi\partial_r - \partial_r\phi\partial_z) - \partial_r\phi\partial_0 + \frac{1}{r}\partial_z\phi] \\ -\{2ie[(A_z\partial_r - A_r\partial_z) + A_r\partial_0] + ie(\partial_z A_r - \partial_r A_z) + \frac{ie}{\phi}(\partial_z\phi A_r - \partial_r\phi A_z) + \frac{1}{\phi}(\partial_z\phi\partial_r - \partial_r\phi\partial_z)\} - \frac{1}{\phi}\partial_r\phi\partial_0 & \partial_0^2 - \left(\partial_r^2 + \frac{1}{r}\partial_r + \partial_z^2 - \frac{1}{r^2}\right) + e^2(A_r^2 + A_z^2) - ie(\partial_z A_z + \partial_r A_r + \frac{1}{r}A_r) + 2ieA_z\partial_0 + \frac{2ie}{r}A_r + \frac{ie}{\phi}(\partial_z\phi A_z + \partial_r\phi A_r) + \frac{1}{\phi}[(\partial_z\phi\partial_z + \partial_r\phi\partial_r) + \partial_z\phi\partial_0 + \frac{1}{r}\partial_r\phi] + |g\phi|^2 \end{pmatrix} \begin{pmatrix} a_L \\ \\ b_L \end{pmatrix} = 0 \tag{3.22}$$

reduces to the form,

$$\begin{pmatrix} -(\partial_r^2 + \partial_z^2) + e^2(A_r^2 + A_z^2) - ie(\partial_r A_r + \partial_z A_z) + |g\phi|^2 + \frac{ie}{\phi}(\partial_z\phi A_z + \partial_r\phi A_r) + \frac{1}{\phi}(\partial_z\phi\partial_z + \partial_r\phi\partial_r) & 2ie(A_z\partial_r - A_r\partial_z) - ie(\partial_z A_r - \partial_r A_z) + \frac{ie}{\phi}(\partial_z\phi A_r - \partial_r\phi A_z) + \frac{1}{\phi}(\partial_z\phi\partial_r - \partial_r\phi\partial_z) \\ -[2ie(A_z\partial_r - A_r\partial_z) - ie(\partial_z A_r - \partial_r A_z) + \frac{ie}{\phi}(\partial_z\phi A_r - \partial_r\phi A_z) + \frac{1}{\phi}(\partial_z\phi\partial_r - \partial_r\phi\partial_z)] & -(\partial_r^2 + \partial_z^2) + e^2(A_r^2 + A_z^2) - ie(\partial_z A_z + \partial_r A_r) + |g\phi|^2 + \frac{ie}{\phi}(\partial_z\phi A_z + \partial_r\phi A_r) + \frac{1}{\phi}(\partial_z\phi\partial_z + \partial_r\phi\partial_r) \end{pmatrix} \begin{pmatrix} a_L \\ \\ b_L \end{pmatrix} = 0. \tag{3.23}$$

For operators D_1 and D_2, this has the form

$$\begin{pmatrix} D_1 & D_2 \\ \\ -D_2 & D_1 \end{pmatrix} \begin{pmatrix} a_L \\ \\ b_L \end{pmatrix} + \begin{pmatrix} -A & -B \\ \\ -B & A \end{pmatrix} \partial_0 \begin{pmatrix} a_L \\ \\ b_L \end{pmatrix} = 0$$

Then

$$D_1 a_L + D_2 b_L = 0 = D_1 b_L - D_2 a_L$$

$$\Longrightarrow D_1(a_L + ib_L) + D_2(b_L - ia_L) = 0$$

$$\Longrightarrow (D_1 - iD_2)(a_L + ib_L) = 0, \quad (D_1 + iD_2)(a_L - ib_L) = 0,$$

where

$$D_1 = -(\partial_r^2 + \partial_z^2) + e^2(A_r^2 + A_z^2) - ie(\partial_z A_z + \partial_r A_r) + |g\phi|^2$$
$$+ \frac{ie}{\phi}(\partial_z \phi A_z + \partial_r \phi A_r) + \frac{1}{\phi}(\partial_z \phi \partial_z + \partial_r \phi \partial_r),$$

$$D_2 = 2ie(A_z \partial_r - A_r \partial_z) - ie(\partial_z A_r - \partial_r A_z)$$
$$+ \frac{ie}{\phi}(\partial_z \phi A_r - \partial_r \phi A_z) + \frac{1}{\phi}(\partial_z \phi \partial_r - \partial_r \phi \partial_z).$$

Now let r_s be the distance from the straight string, so the equations of motion are confined to the $r_s - z$ plane. In order to see if the 1-dimensional solution satisfies the equations of motion in this case, we have to effect a transformation to 2 dimensions.

We first convert to cylindrical polars, using the definitions,

r_0 radius of loop

$r_s z_s$ distance from string on lattice in r and z directions.

$\rho = \sqrt{(r_s^2 + z^2)}$ radial distance from string

ξ polar angle

$\phi = f(\rho)e^{it\xi}$, where $t = \pm 1$ is the phase sign of the Higgs field

then,

$$\rho = \sqrt{r_s^2 + z^2} \Longrightarrow \sin\xi = \frac{z}{\rho}, \quad \cos\xi = \frac{r_s}{\rho}, \quad \tan\xi = \frac{z}{r_s};$$
$$\xi_{,z} = \frac{1}{r_s}\tan^{-1}\left(\frac{z}{r_s}\right) = \frac{r_s}{\rho^2}; \quad \xi_{,r} = -\frac{z}{r_s^2}\tan^{-1}\left(\frac{z}{r_s}\right) = -\frac{z}{\rho^2}.$$

With $A_\rho = 0, \quad A_\xi = A_\xi(\rho)$, we then have the collected terms,

$\partial_r^2 + \partial_z^2 = \partial_\rho^2 + \frac{1}{\rho}\partial_\rho + \frac{1}{\rho^2}\frac{\partial^2}{\partial\xi^2}$,

$A_r\partial_r + A_z\partial_z = \frac{1}{\rho}A_\xi\partial_\xi$,

$A_r^2 + A_z^2 = A_\xi^2$,

$\partial_r A_r + \partial_z A_z = 0$,

$\frac{1}{\phi}(\partial_r\phi\partial_r + \partial_z\phi\partial_z) = \frac{f'(\rho)}{f}\partial_\rho + \frac{it}{\rho^2}\partial_\xi$,

$\frac{1}{\phi}(\partial_r\phi A_r + \partial_z\phi A_z) = \frac{it}{\rho}A_\xi$,

$A_z\partial_r - A_r\partial_z = A_\xi\partial_\rho$,

$\partial_z A_r - \partial_r A_z = -\partial_\rho A_\xi - \frac{1}{\rho}A_\xi$,

$\frac{1}{\phi}(\partial_z\phi\partial_r - \partial_r\phi\partial_z) = \frac{it}{\rho}\partial_\rho - \frac{1}{\rho}\frac{f'(\rho)}{f}\partial_\xi$,

$\frac{1}{\phi}(\partial_z\phi A_r - \partial_r\phi A_z) = -\frac{f'(\rho)}{f}A_\xi$.

Substituting these terms in the matrix (3.23), we get the operators for the straight string equation,

$$D_1 = -(\partial_\rho^2 + \frac{1}{\rho}\partial_\rho + \frac{1}{\rho^2}\frac{\partial^2}{\partial\xi^2}) + e^2A_\xi^2 + g^2f^2 + ie(\frac{it}{\rho}A_\xi) + \frac{f'(\rho)}{f}\partial_\rho + \frac{it}{\rho^2}\partial_\xi, \tag{3.24}$$

$$D_2 = 2ieA_\xi\partial_\rho - ie(-\partial_\rho A_\xi - \frac{1}{\rho}A_\xi) + ie(-\frac{f'(\rho)}{f}A_\xi) + \frac{it}{\rho}\partial_\rho - \frac{1}{\rho}\frac{f'(\rho)}{f}\partial_\xi. \tag{3.25}$$

When ρ is very small, we can try

$(a_L \pm ib_L) \sim (\rho^p e^{iq\xi})$,

so that,

$$(D_1 - iD_2)(\rho^p e^{iq\xi}) = (D_1 + iD_2)(\rho^p e^{iq\xi}) = 0,$$

to give the indicial equation,

$$-(p^2 - q^2) + p - tq \pm (-q + tp) = 0, \tag{3.26}$$

with the solution $p = (0, 2)$, so that the initial value for the numerical approximation consists of a constant plus a term in ρ^2. The full solution to this equation is given in Appendix 2.

Returning to the straight-string operators, we can omit terms containing theta derivatives, as the loop is assumed to be symmetrical about the origin, to obtain the straight-string equation of motion.

With $t = \pm 1$, the operators are now,

$$D_1 = -(\partial_\rho^2 + \frac{1}{\rho}\partial_\rho) + e^2 A_\xi^2 + g^2 f^2 \mp \frac{e}{\rho} A_\xi + \frac{f'(\rho)}{f}\partial_\rho, \tag{3.27}$$

$$D_2 = 2ieA_\xi \partial_\rho - ie(-\partial_\rho A_\xi - \frac{1}{\rho}A_\xi) + ie(-\frac{f'(\rho)}{f}A_\xi) \pm \frac{i}{\rho}\partial_\rho. \tag{3.28}$$

We next require real equations for the coinciding solutions for each spinor component and since,

$$D_1 a_L + D_2 b_L = 0 \qquad (a) \tag{3.29}$$

$$D_1 b_L - D_2 a_L = 0 \qquad (b) \tag{3.30}$$

$$(1) \qquad a_L = -ib_L \Longrightarrow \quad (D_2 - iD_1)b_L = 0, \tag{3.31}$$

$$(2) \qquad a_L = ib_L \Longrightarrow \quad (D_1 - iD_2)b_L = 0, \tag{3.32}$$

$$(3) \qquad b_L = ia_L \Longrightarrow \quad (D_2 - iD_1)a_L = 0, \tag{3.33}$$

$$(4) \qquad b_L = -ia_L \Longrightarrow \quad (D_1 - iD_2)a_L = 0, \tag{3.34}$$

with t=+1, the required solution is given by (2) and (4), with the same equation for a_L and b_L,

$$\begin{pmatrix} D_1 & D_2 \\ & \\ -D_2 & D_1 \end{pmatrix} \begin{pmatrix} ib_L \\ \\ b_L \end{pmatrix} = 0, \qquad \begin{pmatrix} D_1 & D_2 \\ & \\ -D_2 & D_1 \end{pmatrix} \begin{pmatrix} a_L \\ \\ -ia_L \end{pmatrix} = 0. \tag{3.35}$$

Putting g=1,

$$D_1 = \left\{ -\frac{\partial^2}{\partial\rho^2} - \frac{1}{\rho}\frac{\partial}{\partial\rho} + e^2 A_\xi^2 + f^2 - \frac{e}{\rho}A_\xi + \frac{f'}{f}\frac{\partial}{\partial\rho} \right\}, \tag{3.36}$$

$$D_2 = \left\{ 2ieA_\xi \frac{\partial}{\partial\rho} + ie\frac{\partial}{\partial\rho}A_\xi + \frac{ie}{\rho}A_\xi - ie\frac{f'}{f}A_\xi + \frac{i}{\rho}\frac{\partial}{\partial\rho} \right\}. \tag{3.37}$$

The solution $(D_1 - iD_2)a_L = 0$, is then,

$$\left\{ -\frac{\partial^2}{\partial\rho^2} + \left(\frac{f'}{f} + 2eA_\xi\right)\frac{\partial}{\partial\rho} + \left(f^2 + e^2 A_\xi^2 + e\frac{\partial A_\xi}{\partial\rho} - e\frac{f'}{f}A_\xi\right) \right\} a_L = 0. \tag{3.38}$$

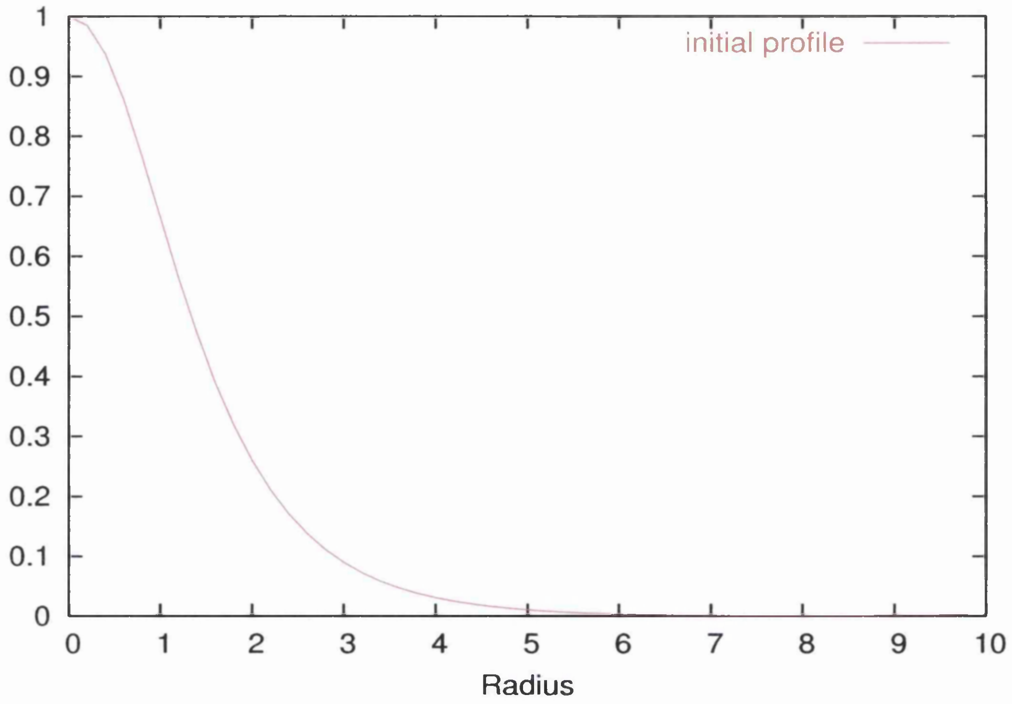

Figure 3.2: The local straight-string fermionic solution which will form the initial profile for the string loop equations.

In Chapter 5 it will be found necessary to assign a specific value to the coupling constant e, and for this reason it cannot be eliminated from (3.38). In that case, we specify $A_\xi = -\alpha/\rho$ and (3.38) then becomes,

$$\left\{-\frac{\partial^2}{\partial\rho^2}+\left(\frac{f'}{f}-2e\frac{\alpha}{\rho}\right)\frac{\partial}{\partial\rho}+\left(f^2+e^2\frac{\alpha^2}{\rho^2}-\frac{e}{\rho}\frac{\partial\alpha}{\partial\rho}+e\frac{f'}{f}\frac{\alpha}{\rho}\right)\right\}a_L=0. \qquad (3.39)$$

The local solution to this equation is shown in Figure 3.2, in which e has been assigned the value 0.3.

Chapter 4

The Dirac Lagrangian

4.1 *The Fermionic Equations of Motion on a Loop*

In order to establish the initial fermionic profile for a straight string in the last chapter, we assumed the derivation of the equations of motion for a loop from the Dirac lagrangian (3.1),

$$L = \bar{\Psi}(\gamma^\mu[i\partial_\mu - eA_\mu])\Psi - \frac{1}{2}ig\phi\bar{\Psi}\Gamma\Psi^c + \frac{1}{2}ig^*\phi^*\bar{\Psi}^c\bar{\Gamma}\Psi. \tag{4.1}$$

We now proceed with this derivation.

A chiral basis is used for the γ matrices, with

$$\gamma^0 = \begin{pmatrix} 0 & -I \\ -I & 0 \end{pmatrix}, \quad \gamma^i = \begin{pmatrix} 0 & \sigma^i \\ -\sigma^i & 0 \end{pmatrix}, \quad \gamma^5 = \begin{pmatrix} I & 0 \\ 0 & -I \end{pmatrix},$$

where σ^i are the Pauli matrices

$$\sigma^1 = \begin{pmatrix} 0 & 1 \\ 1 & 0 \end{pmatrix}, \quad \sigma^2 = \begin{pmatrix} 0 & -i \\ i & 0 \end{pmatrix}, \quad \sigma^3 = \begin{pmatrix} 1 & 0 \\ 0 & -1 \end{pmatrix},$$

We define the charge conjugate spinor

$$\Psi^c = C\bar{\Psi},$$

where, in this basis, C is an antisymmetric charge conjugation matrix,

$$C = i\gamma^2\gamma^0 = \begin{pmatrix} -i\sigma^2 & 0 \\ 0 & i\sigma^2 \end{pmatrix}. \tag{4.2}$$

The Dirac bilinear coupling matrix Γ must be a Lorentz scalar [2], which is satisfied by,

$$\Gamma = \gamma^5 = \bar{\gamma}^5 = \bar{\Gamma}, \quad \text{or} \quad \Gamma = I;$$

hence, with $\Gamma = \gamma^5$,

$$C\Gamma = \Gamma C = -\begin{pmatrix} i\sigma^2 & 0 \\ 0 & i\sigma^2 \end{pmatrix}, \tag{4.3}$$

and with $\Gamma = I$,

$$C\Gamma = \Gamma C = \begin{pmatrix} -i\sigma^2 & 0 \\ 0 & i\sigma^2 \end{pmatrix}. \tag{4.4}$$

With these definitions for C and Γ, the fermion mass terms in (3.1) can now be derived in terms of either $\bar{\Psi}$ or Ψ. The following derivation is restricted to $\Gamma = \gamma^5$, for reasons which will be explained shortly.

With $\psi_i^c = C_{ij}\bar{\psi}_j$ and $\bar{\psi}_i^c = C_{ij}\overline{(\gamma_{jl}^0\psi_l^*)}$, we have respectively,

$$\bar{\Psi}\Gamma\Psi^c = \bar{\psi}_k\Gamma_{kl}C_{lj}\bar{\psi}_j, \tag{4.5}$$

$$\bar{\Psi}^c\bar{\Gamma}\Psi = -\psi_j C_{jl}\bar{\Gamma}_{lk}\psi_k. \tag{4.6}$$

Varying $\bar{\Psi}, \Psi$ separately, we get

$$\bar{\Psi}\bar{\Gamma}\Psi^c = (\bar{\psi}_k\Gamma_{kl}C_{lj}\bar{\psi}_j + \delta\bar{\psi}_k\Gamma_{kl}C_{lj}\delta\bar{\psi}_j) + (\delta\bar{\psi}_k\Gamma_{kl}C_{lj}\bar{\psi}_j + \bar{\psi}_k\Gamma_{kl}C_{lj}\delta\bar{\psi}_j), \tag{4.7}$$

$$\bar{\Psi}^c\bar{\Gamma}\Psi = -(\psi_j C_{jl}\Gamma_{lk}\psi_k + \delta\psi_j C_{jl}\Gamma_{lk}\delta\psi_k) - (\delta\psi_j C_{jl}\Gamma_{lk}\psi_k + \psi_j C_{jl}\Gamma_{lk}\delta\psi_k), \tag{4.8}$$

with the required terms linear in $\delta\bar{\psi}, \delta\psi$.

Putting $C_{jl}\Gamma_{lk} = [\Gamma C]_{jk} = M_{jk}$, the expanded Lagrangian finally becomes,

$$\begin{aligned} L = L_0 &+ \delta\psi_j\{(\gamma_{ij}^\mu)^T i\partial_\mu\bar{\psi}_i + \bar{\psi}_i\gamma_{ij}^\mu eA_\mu - \frac{1}{2}ig^*\phi^*[M_{ji} - M_{ij}]\psi_i\} \\ &+\delta\bar{\psi}_i\{\gamma_{ij}^\mu i\partial_\mu\psi_j - \gamma_{ij}^\mu eA_\mu\psi_j - \frac{1}{2}ig\phi[M_{ij} - M_{ji}]\bar{\psi}_j\}. \end{aligned} \tag{4.9}$$

The 4-component spinor ψ can be decomposed into two 2-component Weyl spinors consisting of left and right components, using the chiral operators

$$\psi = \psi_L + \psi_R = \frac{1}{2}(1 - \gamma_5)\psi + \frac{1}{2}(1 + \gamma_5)\psi, \tag{4.10}$$

and conjugate wavefunction

$$\bar{\psi} = \bar{\psi}_L + \bar{\psi}_R = \bar{\psi}\frac{1}{2}(1+\gamma_5) + \bar{\psi}\frac{1}{2}(1-\gamma_5). \tag{4.11}$$

We then have,

$$\bar{\psi}_L(\gamma^\mu[i\partial_\mu - eA_\mu])\psi_R = \bar{\psi}\frac{1}{2}(1+\gamma_5)\gamma^\mu[i\partial_\mu - eA_\mu]\frac{1}{2}(1+\gamma_5)\psi$$

$$= \frac{1}{4}\bar{\psi}\gamma^\mu(1-\gamma_5)(1+\gamma_5)\psi = 0, \tag{4.12}$$

from which it follows,

$$\bar{\psi}(\gamma^\mu[i\partial_\mu - eA_\mu])\psi \to \bar{\psi}_L(\gamma^\mu[i\partial_\mu - eA_\mu])\psi_L + \bar{\psi}_R(\gamma^\mu[i\partial_\mu - eA_\mu])\psi_R. \tag{4.13}$$

Also, from $\bar{\psi}\Gamma\psi^c$,

$$\bar{\psi}\Gamma C\bar{\psi} = \bar{\psi}\frac{1}{2}(1+\gamma_5)\Gamma C\bar{\psi}\frac{1}{2}(1+\gamma_5) + \bar{\psi}\frac{1}{2}(1-\gamma_5)\Gamma C\bar{\psi}\frac{1}{2}(1-\gamma_5)$$

$$= \bar{\psi}_L\Gamma C\bar{\psi}_L + \bar{\psi}_R\Gamma C\bar{\psi}_R, \tag{4.14}$$

and from $\bar{\psi}^c\Gamma C\psi$,

$$\psi\Gamma C\psi = \frac{1}{2}(1-\gamma_5)\psi\Gamma C\frac{1}{2}(1-\gamma_5)\psi + \frac{1}{2}(1+\gamma_5)\psi\Gamma C\frac{1}{2}(1+\gamma_5)\psi$$

$$= \psi_L\Gamma C\psi_L + \psi_R\Gamma C\psi_R. \tag{4.15}$$

A Dirac-type mass has the form

$$\bar{\psi}\psi \to m(\bar{\psi}_L\psi_R + \bar{\psi}_R\psi_L), \tag{4.16}$$

whereas in this case the fermion mass terms connect the left and right components of conjugate fields, and therefore constitute Majorana-type mass.

The full Dirac lagrangian thus becomes,

$$L = \bar{\psi}_L(\not{\partial} + ie\not{A})\psi_L + \bar{\psi}_R(\not{\partial} + ie\not{A})\psi_R$$

$$-\frac{1}{2}g\phi\{\bar{\psi}_L\Gamma C\bar{\psi}_L + \bar{\psi}_R\Gamma C\bar{\psi}_R\} - \frac{1}{2}g^*\phi^*\{\psi_L\Gamma C\psi_L + \psi_R\Gamma C\psi_R\}. \tag{4.17}$$

The complete Lagrangian must also include the scalar and gauge fields. The Euler-Lagrange equations for these have already been produced, (2.6) and (2.15)-(2.17), and it is against this background that the Dirac equations of motion will be applied.

Due to the two Lorentz scalar values for Γ, we must consider separately two possible spinor-scalar interactions with four-component spinors. Defining ΓC as either $\gamma^5 C$ or IC, then when $\Gamma = \gamma^5$ the Lagrangian (4.17) is hermitian, but when $\Gamma = I$, we need to put $\Gamma = iI$ to ensure that it remains so.

4.2 *The Derivation of the Equations of Motion*

The components of $\psi, \bar{\psi}$ are determined from the chiral operators (4.10), (4.11),

$$\psi = \frac{1}{2}\begin{pmatrix} 0 & 0 \\ 0 & 2 \end{pmatrix}\psi + \frac{1}{2}\begin{pmatrix} 2 & 0 \\ 0 & 0 \end{pmatrix}\psi = \begin{pmatrix} 0 \\ 0 \\ a_L \\ b_L \end{pmatrix} + \begin{pmatrix} a_R \\ b_R \\ 0 \\ 0 \end{pmatrix} = \begin{pmatrix} a_R \\ b_R \\ a_L \\ b_L \end{pmatrix} \tag{4.18}$$

$$\bar{\psi} = \frac{1}{2}\begin{pmatrix} 2 & 0 \\ 0 & 0 \end{pmatrix}\bar{\psi} + \frac{1}{2}\begin{pmatrix} 0 & 0 \\ 0 & 2 \end{pmatrix}\bar{\psi} = \begin{pmatrix} \bar{a}_L \\ \bar{b}_L \\ 0 \\ 0 \end{pmatrix} + \begin{pmatrix} 0 \\ 0 \\ \bar{a}_R \\ \bar{b}_R \end{pmatrix} = \begin{pmatrix} \bar{a}_L \\ \bar{b}_L \\ \bar{a}_R \\ \bar{b}_R \end{pmatrix}. \tag{4.19}$$

Hence ψ_R, ψ_L are the upper and lower components respectively of Ψ, where

$$\psi_R = \begin{pmatrix} a_R \\ b_R \end{pmatrix}, \quad \psi_L = \begin{pmatrix} a_L \\ b_L \end{pmatrix}, \quad \bar{\psi}_R = \begin{pmatrix} \bar{a}_R \\ \bar{b}_R \end{pmatrix}, \quad \bar{\psi}_L = \begin{pmatrix} \bar{a}_L \\ \bar{b}_L \end{pmatrix}.$$

Using the definitions,

$\gamma_0^T = \gamma^0$, $\gamma_1^T = -\gamma^1$, $\gamma_2^T = \gamma^2$, $\gamma_3^T = -\gamma^3$, $(\gamma^\mu)^\dagger = \gamma^0\gamma^\mu\gamma^0$, the metric $g_{\mu\nu} = (1, -1, -1, -1)$, and the functional derivatives obtained from (4.9),

$$\frac{\delta L}{\delta \bar{\psi}_i} = \gamma^\mu_{ij}(\partial_\mu + ieA_\mu)\psi_j - g\phi\Gamma C\bar{\psi}_j = 0, \tag{4.20}$$

$$\frac{\delta L}{\delta \psi_j} = (\gamma^{\mu}_{ij})^T(\partial_\mu - ieA_\mu)\bar{\psi}_i - g^*\phi^*\Gamma C\psi_i = 0, \tag{4.21}$$

the equations of motion for the left and right spinor components become,

$$(\not{\partial} + ie\not{A})\psi_L - g\phi(\Gamma C)\bar{\psi}_L = 0, \tag{4.22}$$

$$(\not{\partial} + ie\not{A})\psi_R + g\phi(\Gamma C)\bar{\psi}_R = 0, \tag{4.23}$$

$$(\gamma^\mu)^T(\partial_\mu - ieA_\mu)\bar{\psi}_L - g^*\phi^*(\Gamma C)\psi_L = 0, \tag{4.24}$$

$$(\gamma^\mu)^T(\partial_\mu - ieA_\mu)\bar{\psi}_R + g^*\phi^*(\Gamma C)\psi_R = 0. \tag{4.25}$$

Now, up to factors of i,

$$\Gamma C = \begin{pmatrix} \sigma^2 & 0 \\ 0 & \pm\sigma^2 \end{pmatrix}, \tag{4.26}$$

and with $\Gamma = \gamma^5$, both signs are positive and ΓC alternately commutes and anticommutes with $(\gamma^\mu)^T$.

If we work with ψ_L, the same form of the equations applies for both values of Γ because, by multiplying (4.24) by (ΓC) on the left,

$$\gamma^\mu(\partial_\mu - ieA_\mu)(\Gamma C)\bar{\psi}_L - \eta g^*\phi^*(\Gamma C)(\Gamma C)\psi_L = 0 \tag{4.27}$$

where $\eta = \begin{cases} +1 : \gamma^5 \\ -1 : I \end{cases},$

so that with

$$(\Gamma C)(\Gamma C) = \begin{cases} -1 : \gamma^5 \\ +1 : I \end{cases},$$

$$\Longrightarrow \gamma^\mu(\partial_\mu - ieA_\mu)(\Gamma C)\bar{\psi}_L + g^*\phi^*\psi_L = 0. \tag{4.28}$$

Substituting for $\bar{\psi}_L$

$$\gamma^\mu(\partial_\mu - ieA_\mu)\frac{1}{g\phi}\gamma^\nu(\partial_\nu + ieA)\psi_L + g^*\phi^*\psi_L = 0, \tag{4.29}$$

$$\Longrightarrow \left\{\Box + e^2A^2 + |g\phi|^2\right\}\psi_L - \frac{\phi_{,\mu}}{\phi}(\gamma^\mu\gamma^\nu)(\partial_\nu + ieA_\nu)\psi_L$$

$$+\gamma^\mu\gamma^\nu\left\{ie(A_\nu\partial_\mu - A_\mu\partial_\nu) + ie\partial_\mu A_\nu\right\}\psi_L = 0. \tag{4.30}$$

For static background fields, when $A_0 = 0; \quad i, j = 1, 2, 3,$

$$\Box + e^2 A^2 - \frac{\phi_{,i}}{\phi}(\gamma^i\gamma^j)(\partial_j + ieA_j)\psi_L - \frac{\phi_{,i}}{\phi}(\gamma^i\gamma^0)\partial_0\psi_L$$

$$+\gamma^i\gamma^j ie(A_j\partial_i - A_i\partial_j) + ie(\partial_i A_j) + \gamma^i\gamma^0(-ieA_i\partial_0) + |g\phi|^2\psi_L = 0. \qquad (4.31)$$

$$\text{Now,} \quad \gamma^i\gamma^0 = \begin{pmatrix} -\sigma_i & 0 \\ 0 & \sigma_i \end{pmatrix}, \quad \gamma^i\gamma^j = \begin{pmatrix} -\sigma_i\sigma_j & 0 \\ 0 & -\sigma_i\sigma_j \end{pmatrix},$$

$\Longrightarrow$ only $\gamma^i\gamma^0$ terms change sign between right and left ψ components, so restricting ourselves to the bottom two components, ψ_L,

$$\Longrightarrow \left\{\Box + e^2A^2 + |g\phi|^2\right\}\psi_L - \sigma_i\left[\frac{\phi_{,i}}{\phi} + 2ieA_i\right](\partial_0\psi_L)$$

$$+\sigma_i\sigma_j\left[\frac{\phi_{,i}}{\phi}(\partial_j + ieA_j) - ie(A_j\partial_i - A_i\partial_j) - ie(\partial_i A_j)\right]\psi_L = 0. \qquad (4.32)$$

Pulling the σ's across, with

$$\sigma_i\sigma_j + \sigma_j\sigma_i = 2\delta_{ij}, \qquad (4.33)$$

$$\Longrightarrow \left\{\Box + e^2A^2 - 2ieA_i\partial_i + |g\phi|^2\right\}\psi_L - \left[\frac{(\sigma_i\phi_{,i})}{\phi} + 2ie(\sigma_iA_i)\right]\partial_0\psi_L$$

$$+ie\frac{(\sigma_i\phi_{,i})}{\phi}(\sigma_jA_j)\psi_L + \left[\frac{(\sigma_i\phi_{,i})}{\phi} + 2ie(\sigma_iA_i)\right](\sigma_j\partial_j)\psi_L$$

$$-ie[(\sigma_i\partial_i)(\sigma_jA_j)]\psi_L = 0, \qquad (4.34)$$

from which we note there are various sigma-coupled terms of similar form, for example,

$$(\sigma_i\partial_i) = \begin{pmatrix} \partial_z & \partial_x - i\partial_y \\ \partial_x + i\partial_y & -\partial_z \end{pmatrix}, \quad (\sigma_iA_i) = \begin{pmatrix} A_z & A_x - iA_y \\ A_x + iA_y & -A_z \end{pmatrix}. \qquad (4.35)$$

We can now go into polars using:

$$x = r\cos\theta, \quad y = r\sin\theta, \quad \partial_r = \cos\theta\frac{\partial}{\partial x} + \sin\theta\frac{\partial}{\partial y}, \quad \frac{1}{r}\partial_\theta = -\sin\theta\frac{\partial}{\partial x} + \cos\theta\frac{\partial}{\partial y};$$

from which we get the transformation matrices,

$$\begin{pmatrix} \partial_r \\ \frac{1}{r}\partial_\theta \end{pmatrix} = \begin{pmatrix} \cos\theta & \sin\theta \\ -\sin\theta & \cos\theta \end{pmatrix}\begin{pmatrix} \partial_x \\ \partial_y \end{pmatrix}, \quad \begin{pmatrix} \partial_x \\ \partial_y \end{pmatrix}\begin{pmatrix} \cos\theta & -\sin\theta \\ \sin\theta & \cos\theta \end{pmatrix}\begin{pmatrix} \partial_r \\ \frac{1}{r}\partial_\theta \end{pmatrix}, \qquad (4.36)$$

$$\Longrightarrow \partial_x - i\partial_y = e^{-i\theta}(\partial_r - \frac{i}{r}\partial_\theta); \quad A_x - iA_y = e^{-i\theta}(A_r - iA_\theta), \tag{4.37}$$

$$\partial_x + i\partial_y = e^{i\theta}(\partial_r + \frac{i}{r}\partial_\theta); \quad A_x + iA_y = e^{i\theta}(A_r + iA_\theta), \tag{4.38}$$

so in general the sigma terms now become,

$$\begin{pmatrix} \partial_z & e^{-i\theta}\left(\partial_r - \frac{i}{r}\partial_\theta\right) \\ e^{i\theta}\left(\partial_r + \frac{i}{r}\partial_\theta\right) & -\partial_z \end{pmatrix}, \quad \begin{pmatrix} A_z & e^{-i\theta}(A_r - iA_\theta) \\ e^{i\theta}(A_r + iA_\theta) & -A_z \end{pmatrix}. \tag{4.39}$$

The exponential terms mean that the angular dependence will also have to be considered. Since all combinations of terms result in the same matrix structure,

$$\begin{pmatrix} \alpha & e^{-i\theta}\beta \\ e^{i\theta}\gamma & \delta \end{pmatrix}, \tag{4.40}$$

the angular form can be taken to be,

$$\psi_L = \begin{pmatrix} e^{im\theta}a_L(r,z) \\ e^{i(m+1)\theta}b_L(r,z) \end{pmatrix}, \tag{4.41}$$

where m is the angular dependence. On a straight string the true zero energy mode has no dependence; since the mass is zero, so is the momentum, and m=0. In the case of a loop, this value for m is also used for reasons which are explained in Chapter 5, section 5.5.

Using

$$A_i\partial_i = A_r\partial_r + \frac{A_\theta}{r}\partial_\theta + A_z\partial_z, \tag{4.42}$$

$$\partial_i A_i = \partial_r A_r + \frac{1}{r}A_r + \frac{\partial_\theta}{r}A_\theta + \partial_z A_z, \tag{4.43}$$

the various terms in (4.34) can now be expressed directly in polars,

In the restricted case, when the background fields are independent of θ and $A_\theta = 0$, the sigma-coupled terms simplify,

$$[\sigma_i A_i] = \begin{pmatrix} A_z & A_r \\ A_r & -A_z \end{pmatrix}, \quad [\sigma_i \phi,_i] = \begin{pmatrix} \partial_z\phi & \partial_r\phi \\ \partial_r\phi & -\partial_z\phi \end{pmatrix}, \tag{4.44}$$

$$(\sigma_i\partial_i)(\sigma_jA_j) = \begin{pmatrix} \partial_zA_z + \partial_rA_r + +\frac{1}{r}A_r & \partial_zA_r - \partial_rA_z \\ & \\ \partial_rA_z - \partial_zA_r & \partial_rA_r + \frac{1}{r}A_r + \partial_zA_z \end{pmatrix}, \tag{4.45}$$

and we also note the terms,

$$\psi_L = \begin{pmatrix} a_L \\ b_L \end{pmatrix} \implies \quad [\sigma_j\partial_j\psi_L] = \begin{pmatrix} \partial_za_L + \partial_rb_L + \frac{(m+1)}{r}b_L \\ \\ \partial_ra_L - \frac{m}{r}a_L - \partial_zb_L \end{pmatrix}, \tag{4.46}$$

$$\implies [\sigma_j\partial_j - \partial_0]\psi_L = \begin{pmatrix} \partial_za_L - \partial_0a_L & \partial_rb_L + \frac{m+1}{r}b_L \\ & \\ \partial_ra_L - \frac{m}{r}a_L & -\partial_zb_L - \partial_0b_L \end{pmatrix}. \tag{4.47}$$

Equation (4.34), is first rearranged slightly before changing to polars,

$$\begin{aligned} &\left\{\Box + e^2A^2 - 2ie(A_r\partial_r + A_z\partial_z) + |g\phi|^2\right\}\psi_L \\ &+ \left[\frac{(\sigma_i\phi_{,i})}{\phi} + 2ie(\sigma_iA_i)\right][\sigma_j\partial_j - \partial_0]\psi_L + ie\frac{(\sigma_i\phi_{,i})}{\phi}(\sigma_jA_j)\psi_L \\ &-ie[(\sigma_i\partial_i)(\sigma_jA_j)]\psi_L = 0, \end{aligned} \tag{4.48}$$

and the various terms are now applied. Putting $m = 0$ and noting that the $(A_r\partial_r + A_z\partial_z)$ terms cancel, the result can now be represented as a single matrix,

$$\begin{pmatrix} \partial_t^2 - (\partial_r^2 + \frac{1}{r}\partial_r + \partial_z^2) + e^2(A_r^2 + A_z^2) - ie(\partial_zA_z + \partial_rA_r + \frac{1}{r}A_r) - 2ieA_z\partial_0 + \frac{ie}{\phi}(\partial_z\phi A_z + \partial_r\phi A_r) + \frac{1}{\phi}[(\partial_z\phi\partial_z + \partial_r\phi\partial_r) - \partial_z\phi\partial_0] + |g\phi|^2 & 2ie[(A_z\partial_r - A_r\partial_z) - A_r\partial_0 + \frac{1}{r}A_z] - ie(\partial_zA_r - \partial_rA_z) + \frac{ie}{\phi}(\partial_z\phi A_r - \partial_r\phi A_z) + \frac{1}{\phi}[(\partial_z\phi\partial_r - \partial_r\phi\partial_z) - \partial_r\phi\partial_0 + \frac{1}{r}\partial_z\phi] \\ & \\ -\{2ie[(A_z\partial_r - A_r\partial_z) + A_r\partial_0] - ie(\partial_zA_r - \partial_rA_z) + \frac{ie}{\phi}(\partial_z\phi A_r - \partial_r\phi A_z) + \frac{1}{\phi}[(\partial_z\phi\partial_r - \partial_r\phi\partial_z) + \partial_r\phi\partial_0]\} & \partial_t^2 - (\partial_r^2 + \frac{1}{r}\partial_r + \partial_z^2 - \frac{1}{r^2}) + e^2(A_r^2 + A_z^2) - ie(\partial_zA_z + \partial_rA_r + \frac{1}{r}A_r) + 2ieA_z\partial_0 + \frac{2ie}{r}A_r + \frac{ie}{\phi}(\partial_z\phi A_z + \partial_r\phi A_r) + \frac{1}{\phi}[(\partial_z\phi\partial_z + \partial_r\phi\partial_r) + \partial_z\phi\partial_0 + \frac{1}{r}\partial_r\phi] + |g\phi|^2 \end{pmatrix} \begin{pmatrix} a_L \\ \\ \\ b_L \end{pmatrix} = 0. \tag{4.49}$$

In the next chapter this matrix will form the basis for the 2-dimensional equations, first for a straight-string approximation, and then in the special case of a symmetrical loop.

Expansion of the ϕ terms, with $\phi, \phi^\dagger = \phi_1 \pm i\phi_2$, eliminates the complex terms as in the bosonic equations. This results in a real and imaginary equation of motion for each of the spinor components. In this form, these four equations can then be directly translated into the program code to obtain a numerical solution.

Chapter 5

Fermion Zero Modes on a Loop

5.1 *The Time-Dependent Straight String Approximation*

We can now use the equations obtained in the last chapter to observe the behaviour of fermions when they are allowed to evolve on a static bosonic background. Before looking at a loop, the matrix (4.49) is used to obtain the numerical approximation in the case of a straight string by letting $r \to \infty$, as in the 1-dimensional case, but this time the time-dependence is retained. The loop still passes through the centre of the lattice, but its radius is now made effectively infinite by making it 10^{20}; the result can be viewed in two dimensions, Fig.5.1, which superimposes both spinor components when they have fully settled after approximately 500 time steps. After stability is attained, the profile shape remains unchanged over time, while the magnitude steadily decreases. The bosonic background fields are already stable and fully evolved before the fermions are introduced; this requires a minimum of 1600 time steps.

However, it is more revealing to look at the fermionic cross-sections for the ψ component a_L and b_L on lattices of 100×100 and 200×200, Figure 5.2. This illustrates how well the the pairs of cross-sections align on each lattice, with a very small relative displacement near the base between the two lattices. At this stage two important parameter choices need to be mentioned, namely the electromagnetic coupling constant e in the fermionic equations, and the numerical damping factor

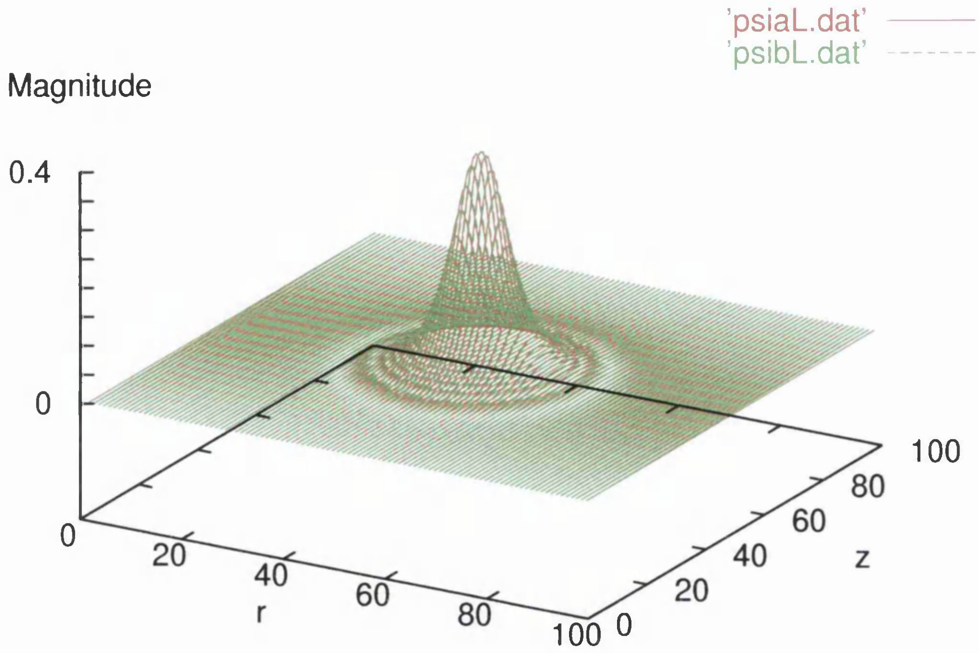

Figure 5.1: The fermionic spinor components in two dimensions on a straight string after 500 timesteps, by which stage the profile has attained its final form.

used in the code. This decision is made now because it maintains consistency at all radii for it will be seen later that the values of both these parameters become critical at radii < 10. At this point the behaviour of the fermions is not noticeably affected in any other way by the value chosen for e, other than to require slightly more time to fully evolve the fields. The numerical damping should ideally be kept to a minimum, for it is an artifact in the code that does not reflect the real world, but if it has to be increased, the main effect at very large radius or on a straight string is to increase the rate of decay.

5.2 *The Fermionic Solutions on a Contracting Loop*

A good point to start investigating a loop is at a radius of 10,000. This is large enough to preclude any radial effects, other than over time spans too long to be of practical

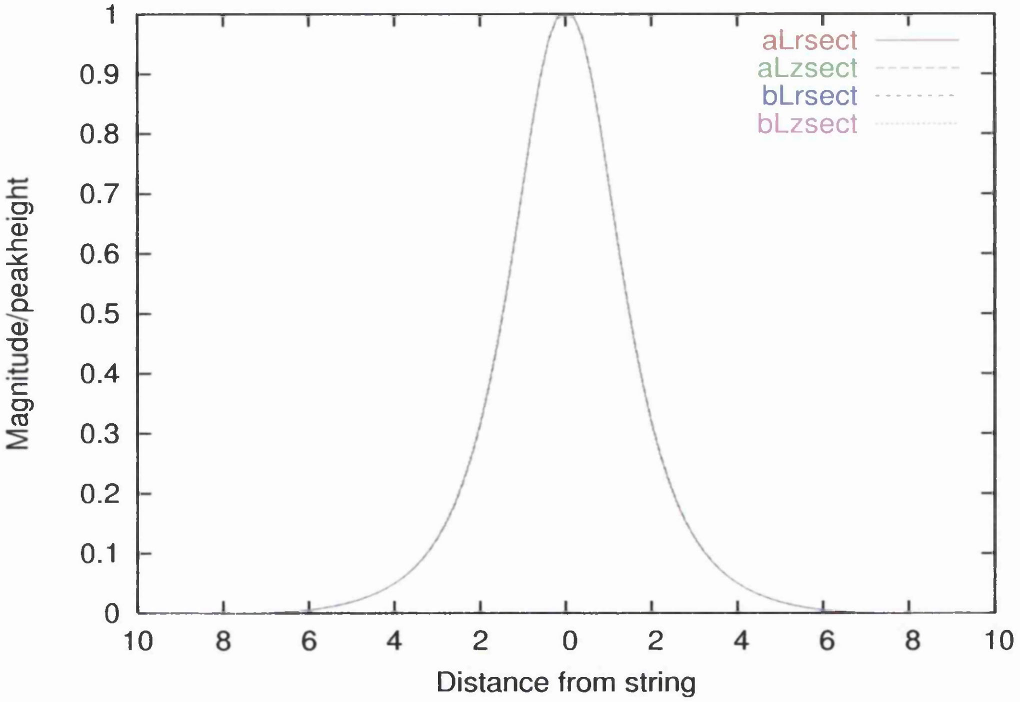

Figure 5.2: The fermionic straight string r-z axis cross-sections on a 100 × 100 lattice for the ψ components a_L, b_L. Both pairs are identical.

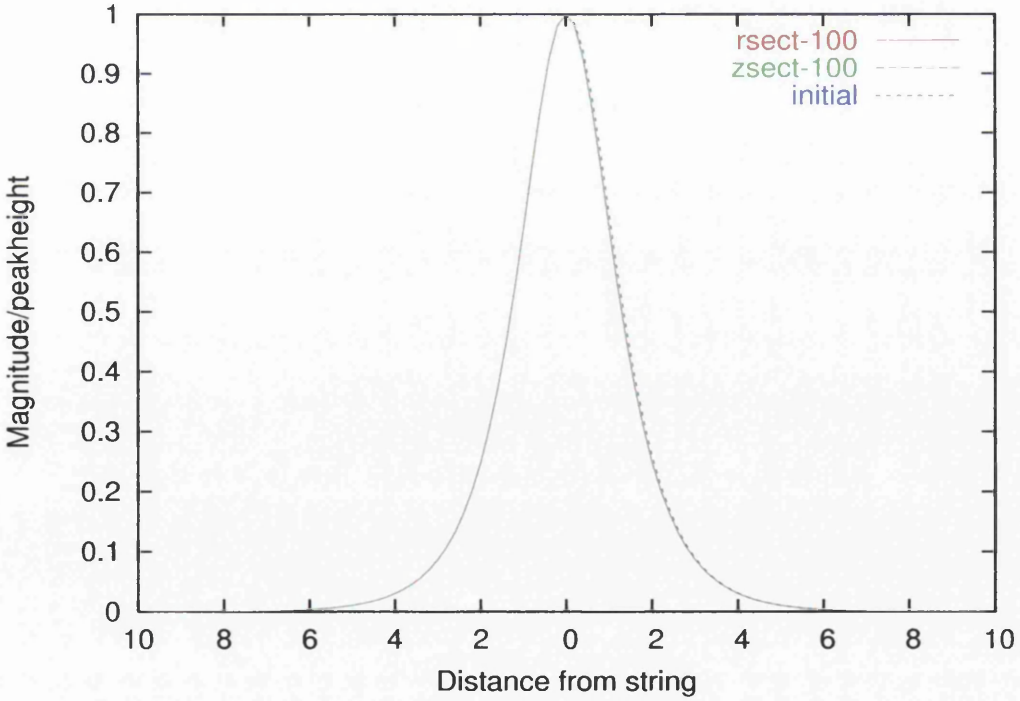

Figure 5.3: The fermionic r-z axis cross-sections for the ψ component a_L on a large loop of radius 10,000 and a 100x100 lattice, compared with the initial profile. The r and z cross-section are identical both with each other and the initial profile.

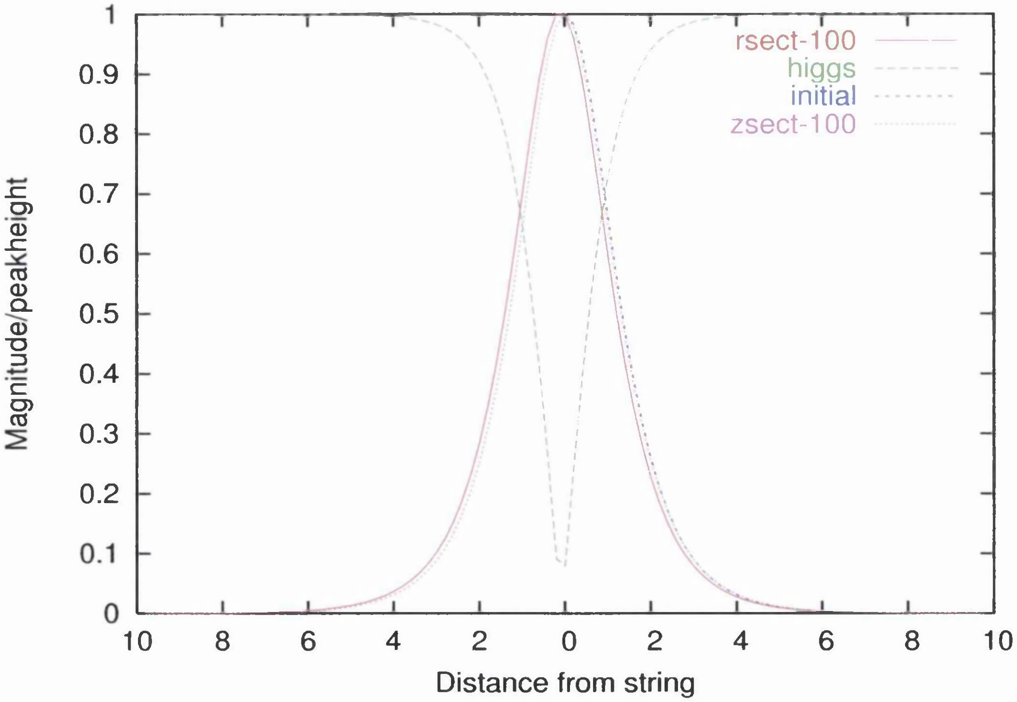

Figure 5.4: The Higgs and ψ component r-z axis cross-sections on a loop of starting radius 30, compared with the initial profile. The z-sections align with the initial profile. The Higgs minimum is mid-way between lattice points, just before the lattice re-centres.

use. Figure 5.3, illustrates the r and z-axis cross-sections for the ψ component a_L at this radius on a 100×100 lattice, showing the perfect alignment with the initial profile even after extended time. Another interesting point is that the rate of decay is much slower than on the straight string. In fact the rate of decay reaches a minimum at around $r = 5000$, before it very gradually starts increasing again.

A more suitable radius to start investigating the behaviour of fermions is around $r = 30$, of which the lattice makes up 10 distance units. This is small enough to produce a change within a reasonable number of steps, but large enough for any change to take place fairly slowly. It turns out that the cycle between lattice points as the radius contracts is essentially the same at all scales, but at this radius is still greatly extended in time. We can use this fact to study various aspects in detail at this larger radius, when there is good control, and this leads to a better understanding as we get down to the smallest radii, when changes occur very rapidly, ultimately over one or two steps.

At this point it is convenient to define the magnitude at the apex of the profile as the peak height, and this term will be used in future. The magnitude is scaled to one in all plots, by dividing by the peak height, which means that the fermionic and bosonic profiles may be superimposed on the same plot. Peak height decay still limits the run time and after about 2000 steps has become very small indeed. At this radius this time span would just provide a sufficient number of data points for future analysis in the next chapter, but other means need to be found to boost the peak height to get a long enough run at smaller radii when the decay becomes very rapid, until it is eventually slowed by increasing oscillations.

The first noticeable thing is that when the Higgs field is very close to its minimum the fermionic field starts increasing exponentially, indicating an instability. Before investigating this, it was first necessary to find out if stable results were obtainable over the rest of the cycle. The bosonic steps were continued until the Higgs minimum was very close to the mid-point between lattice points, Figure 5.4. The fermionic fields settle within a few hundred steps and thereafter the profiles do not change shape, while they slowly decay. Without changing the fermionic fields, a few additional bosonic steps cause the code to shift the lattice back, the lattice re-centering on the string as described with the bosonic fields. Stable fermionic profiles can thus be obtained over the whole cycle apart from the region affected by the instability.

The instability at the lattice points needs further investigation to establish the extent of the region affected. By letting the Higgs minimum approach the lattice point very slowly, latterly 1 step at a time, it is possible to maintain a very stable fermionic profile until the Higgs minimum reaches a value of ~ 0.008, as in Figure 5.5. After this point, the stability starts to deteriorate until significant distortion increases at about 10 bosonic steps before the minimum reaches the lattice point, and in general the field is unstable over a span of about 50 steps. When the Higgs minimum has reached its minimum value at the lattice point the peak height increases exponentially in the space of 50-150 fermionic steps. At this radius there are about

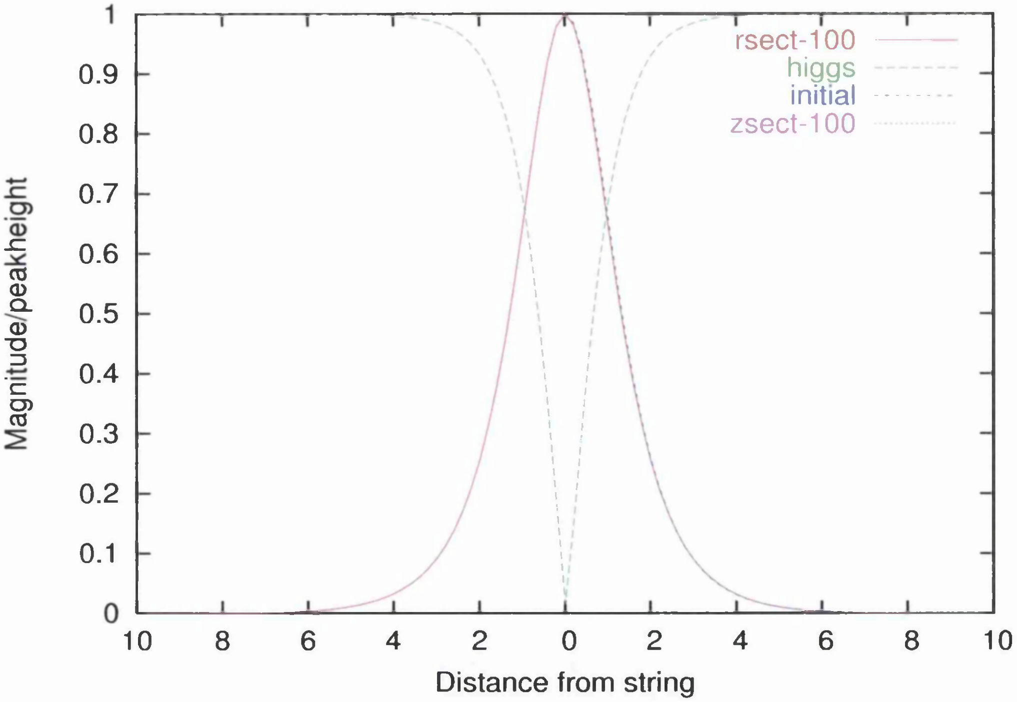

Figure 5.5: The Higgs and ψ component a_L r-axis cross-sections on a loop of radius 28.2, compared with the initial profile. The Higgs minimum has reduced to 0.008, and the fermionic profiles are still very stable.

600 steps between lattice points, so the instability is affecting less than 10 percent of the cycle. There is clearly a problem at the lattice points that seems to be numerical in origin, probably due to the $1/m^2$ terms in the fermionic equations. Some attention has been given to finding a way to slow the enormous increase in the peak height, such as capping the points on either side of the peak, but without success and the conclusion is that the instability exists, probably due to a numerical effect, and the code in its present form cannot handle the simulation there. The important thing is that it is not due to the physics involved, and in that case to treat the affected region at each lattice point with extreme caution, and avoid it altogether. Repeating on the finer lattice, which has smaller time steps, makes it easier to approach the unstable region more smoothly, without ultimately affecting the exponential increase, but it does indicate the problem is probably not lattice-related.

Setting up the method for placing fermions on the string at smaller radii

We can now begin a more detailed analysis at a starting radius of 15, when the loop origin is 5 units from the edge of the lattice.

Applying sufficient steps to produce stable bosonic fields and placing the string close to the mid point between lattice points in this case reduces the radius to 13.6. There are then two ways to follow the string with the fermions as the loop contracts and the string moves across the lattice:

a) Move the bosonic fields one or two lattice spaces at a time, always keeping near the mid-point between lattice points and run the fermions for a few steps each time, when they readily follow the string. In theory this should maintain a good profile down to the desired radius, when a long fermion run can be carried out. In practice problems arise as the damping factor has to be increased at smaller radii, and if the fermions are not stable and are run for too long so that the field collapses, it is necessary to start from the beginning again. This can result in a very long and inefficient procedure.

b) The second method entails altering the code so that the fermions are always placed directly on the string, wherever it is, instead of at the centre of the lattice. In this case, every fermion run is unique and is unaffected by any previous runs. Thus a long run can be performed at a radius of e.g. 5, after which the loop might be reduced to a radius of 4, and the procedure repeated. This results in a large increase in efficiency. Both methods were carefully compared to make sure the resulting profiles are the same, the only difference being that b) requires a slightly longer fermionic run to obtain identical results, because the fermions have to settle down again each time. This method is used from now on.

To enable a sufficiently long fermion run for data analysis at very small radius, the peak height must be numerically boosted to a considerable degree, sometimes as much as by a factor of 10^{25}. This makes it easier to handle the data files, particularly when logarithms are used later to obtain the gradient of the decay. After the bosonic

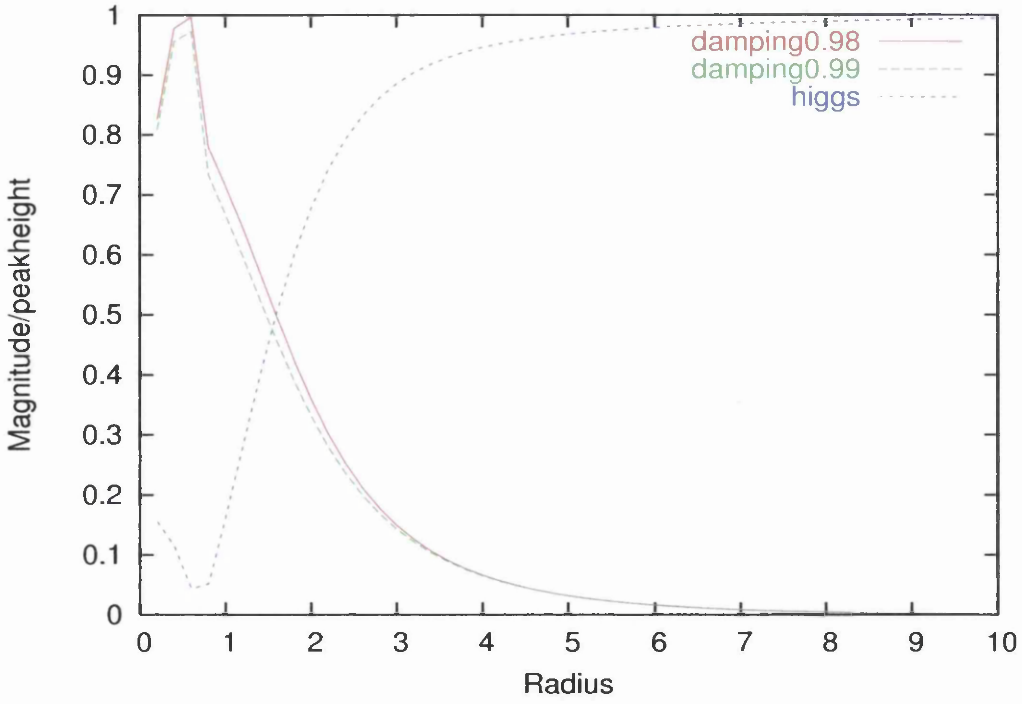

Figure 5.6: The Higgs and fermionic profiles at a radius of 0.6 and damping of 0.98 and 0.99. At this small radius, changes in damping make little relative difference.

fields have run, the required boost is chosen before the number of fermionic steps is entered.

5.3 *Fermionic Modes at Small Radii*

Some examples of fermionic profiles at very small radius for different damping values are shown in Figure 5.6, where it is seen that at this very small radius changes in numerical damping make much less difference. A point of interest is that a reasonable fermionic profile close to the string is still obtained with no numerical damping at all, Figure 5.7. It is only further from the core that the lack of damping is most evident.

The main criterion for comparison in this range is the nature of the fermion decay, which is now examined. The method involves selecting a point on the fermionic profile - the apex is a convenient point - and analysing the output data over time. We are looking for an exponential and increasing rate of decay as the radius decreases and if this is the case, the log of the output will be a straight line. Figure 5.10 with damping

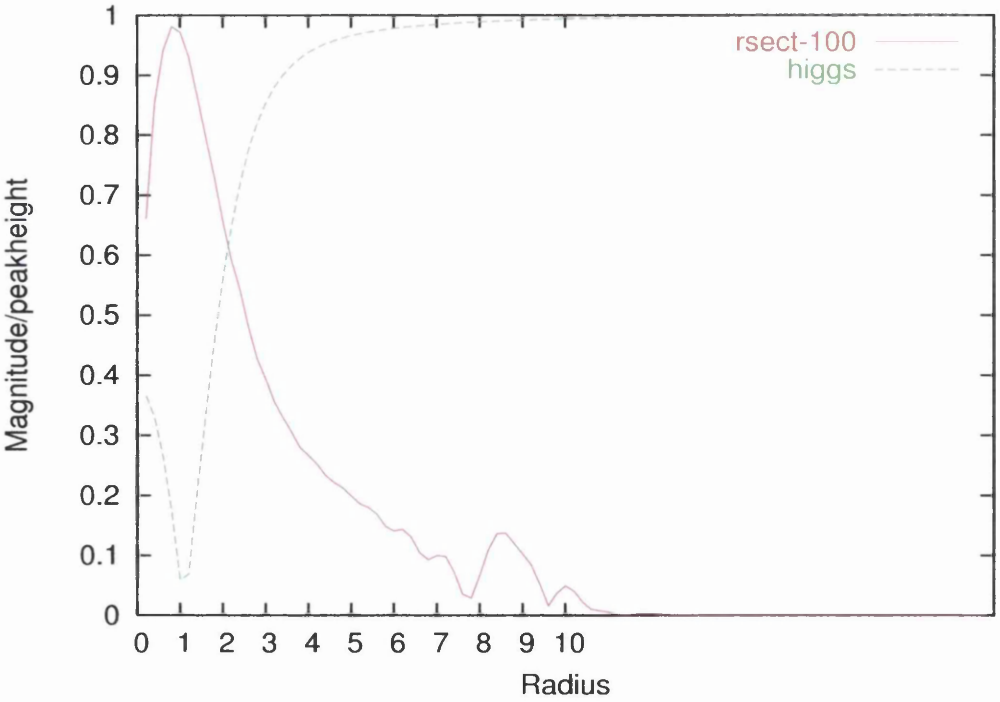

Figure 5.7: The fermionic profile after 1000 steps at a radius of 1.0 and no numerical damping. Even after about 4000 steps the profile is still good close to the string, but the oscillation amplitude becomes more erratic, especially further from the string, with no decay overall.

of 0.98 shows that the increase in gradient is reasonably consistent up to a peak at radius 1.8, after which point the increasing nearness of the boundary causes a rapid decrease in the decay rate.

5.4 *The Onset of Oscillations*

Ideally, it would be preferable not to have to resort to numerical damping, or at best a very minimal amount. However, rather heavy damping of 0.98 is required for a good result at a radius of 0.4, and as a result with this value oscillations only start to appear at a radius between 1.8 and 2. This value is used over the whole radius range for consistency. If the numerical damping is any lighter, the oscillations increase exponentially at a radius of 0.4. The region from a radius of 2 to 0.4 is of principal concern, for the increasing oscillations indicate the fermions are rapidly acquiring increasing mass. Oscillations are first noticeable at a radius of about 3.0, depending on the level of damping; the lighter the damping the earlier the oscillations appear.

However, at larger radii there is often a very fine line between maintaining a stable fermionic profile and obtaining any oscillations, and to ensure reasonable oscillations with a fairly regular period it is preferable to confine the data analysis to radii of less than 2.

Figure 5.9 compares the observed angular frequency Ω, for different damping values. The full data are summarised in table 5.1, over the range from radius $= 10 - 0.4$. The most noticeable thing is the wide difference in the observed frequency for different damping values at a given radius, particularly at the larger radii. The frequencies do start to converge quite rapidly at radii below 1 and there is considerable overlap, but in general the results do not conform well to the SHO model.

It is also found that with very minimal or no numerical damping oscillations never cease at any radius, reaching a constant minimum of 0.21 after a radius of 100, which points to some effect apparently caused by the lattice making the wave bounce backwards and forwards across the box. This is confirmed by repeating for the same parameter values on a 200×200 lattice producing a frequency minimum of $\omega = 0.1$ at any very large radius, which suggests that a much larger lattice would be required for conditions to approach the natural state.

Changing the Parameters

At this stage it is appropriate to discuss more thoroughly the motivation for the choice of parameters briefly mentioned in Section 5.1. Despite leaving this question until now, the fermionic profiles up to this point have assumed certain choices.

On a straight string or at large radius, no problems were evident with the gauge coupling constant e set at 1 in the fermionic equations and a damping factor of 0.98. However, this was not the case when small-radius investigations were started. We have already shown, in subsection 2.2.2, that a suitable starting radius for these investigations is $r = 15$. As the radius was reduced with $e = 1$ it was apparent that the fermionic profile was gradually displacing further to the left of the string. At first this movement was small, but below a radius of 12 the profile continued moving away and increasingly swelling, until the imposed boundary conditions, which ensure that the field is zero along the inner edge of the lattice, prevented it moving off the lattice altogether. Furthermore, at these small radii below 12, the numerical damping is particularly critical; too little and the profile disintegrates, too much and the profile subsides smoothly to zero. In fact, it turned out that there was no single damping value which would enable a satisfactory reduction in radius from about 12. We are most interested in the behaviour of the fermions at the smallest possible radius and with $e = 1$, although apparently producing plausible results at radii below 1, the boundary condition is forcing the fermions back onto the string and therefore the results are probably unreliable.

The reluctance of the fermions to stick to the string over the radius range $12 - 0.4$ was a serious problem, since a zero mode should be strongly associated with the string, and data collection from a chosen point on a profile far from the string cannot be taken as accurate. In the absence of any apparent errors the only alternative was to see if changing certain parameters could affect the result. The two obvious parameters to adjust are the scalar-fermion mass coupling and the gauge coupling.

The mass coupling was first increased by a factor between one and two, and the resulting profile was closer to the string, but very rough with oscillations starting to appear at much larger radii with, as expected, very long periods. Combining this change with a reduction in the gauge coupling produced better results, as the latter tends to oppose the effects produced by a mass increase. In practice, when the rather critical level of the damping factor was brought in, it proved too complex to manipulate with three variables.

The best result was achieved by reducing e alone, from 1.0 to 0.3, until the fermions remained right on the string in the problem span. The overall effect is slightly to suppress the onset of oscillations and to increase the period. However, if the correct numerical damping is chosen, the fermionic profile is very symmetrical and completely stable over the whole range. Much lighter damping of 0.98 is required, which is suitable for the whole range from a straight string down to a radius of 0.4. With either set of parameters it is not possible to get exponential decay at the minimum radius of 0.2, but only an exponential increase, indicating an instability. At first it seemed as if the gauge components might be a main cause of the fermions moving away from the string, but checking with the gauge-invariant quantity $\bar{\psi}\psi$ showed the latter gave the same profiles. This leaves the $1/r$ and $1/r^2$ terms as the most likely cause, although not all those terms are associated with the gauge terms.

It is a distinct compromise having to reduce the value of e to such an extent, or to have to give it a specific value, but there is no reason why e must be equal to 1. To summarise, the reasons in justification for changing this parameter are:

a) the fermions always remain on or very close to the string;

b) the gradient increases steadily and exponentially, until increasing oscillations at very small radius slow the rate of decay;

c) considerably less damping is required.

Rather than the physics involved, it would seem that the most likely source of the problem is the code, which is causing the fermions to move off the string.

radius	damping	T	$\gamma/2$	Ω	ω
10	0.99	26.04	-0.004585	0.2413	0.2413
"	0.985	0	-0.002387	0	0
9	0.99	21.63	-0.004592	0.2905	0.29052
"	0.985	0	-0.002674	0	0
8	0.99	18.69	-0.00469	0.33618	0.3362
"	0.985	0	-0.002965	0	0
7	0.99	17.25	-0.0045934	0.36424	0.36427
"	0.985	0	-0.003294	0	0
6	0.99	15.65	-0.004649	0.401353	0.40138
"	0.985	0	-0.003689	0	0
5	0.99	14.61	-0.004569	0.43	0.43
"	0.985	0	-0.004215	0	0
4	0.99	12.98	-0.004627	0.484	0.4841
"	0.985	0	-0.00555	0	0
3	0.99	11.34	-0.0045116	0.55407	0.5541
"	0.985	27.97	-0.006971	0.2264	0.2275
2.0	0.99	9.33	-0.004264	0.67344	0.67345
"	0.985	14.0	-0.006430	0.4488	0.4488
"	0.98	0	-0.005688	0	0
1.8	0.99	8.78	-0.00421	0.71562	0.71563
"	0.985	10.13	-0.0058	0.6094	0.6095
"	0.98	52.53	-0.006294	0.11961	0.11978

Table 5.1.

radius	damping	T	$\gamma/2$	Ω	ω
1.6	0.99	8.42	-0.003878	0.74622	0.74623
"	0.985	10.19	-0.005323	0.6166	0.61662
"	0.98	16.60	-0.006122	0.37775	0.37778
1.4	0.99	8.00	-0.00343	0.7854	0.7854
"	0.985	9.78	-0.004881	0.64245	0.6425
"	0.98	14.43	-0.0056835	0.4354	0.43546
1.2	0.99	7.81	-0.00311	0.8045	0.8045
"	0.985	9.33	-0.00449	0.67343	0.67345
"	0.98	12.91	-0.005340	0.4867	0.48672
1.0	0.99	7.55	-0.002773	0.8322	0.8322
"	0.985	8.75	-0.004094	0.71808	0.7181
"	0.98	11.28	-0.005	0.55702	0.55704
0.8	0.99	7.16	-0.00243	0.87754	0.87754
"	0.985	8.055	-0.003682	0.78	0.78
"	0.98	9.73	-0.004681	0.64575	0.64577
0.6	0.99	6.71	-0.001846	0.9364	0.9364
"	0.985	7.145	-0.00293	0.87938	0.87938
"	0.98	7.83	-0.00403	0.80245	0.80246
0.4	0.99	exponential increase			
"	0.985	exponential increase			
"	0.98	4.33	-0.002917	1.45108	1.451085

Table 5.1. continued

At any given radius, the figures show that the observed and natural frequencies vary considerably for different damping values. When these damped oscillations arise, they can be compared with the ideal case of a SHO. If they conform reasonably well, we would expect little variation in the natural undamped frequency for different

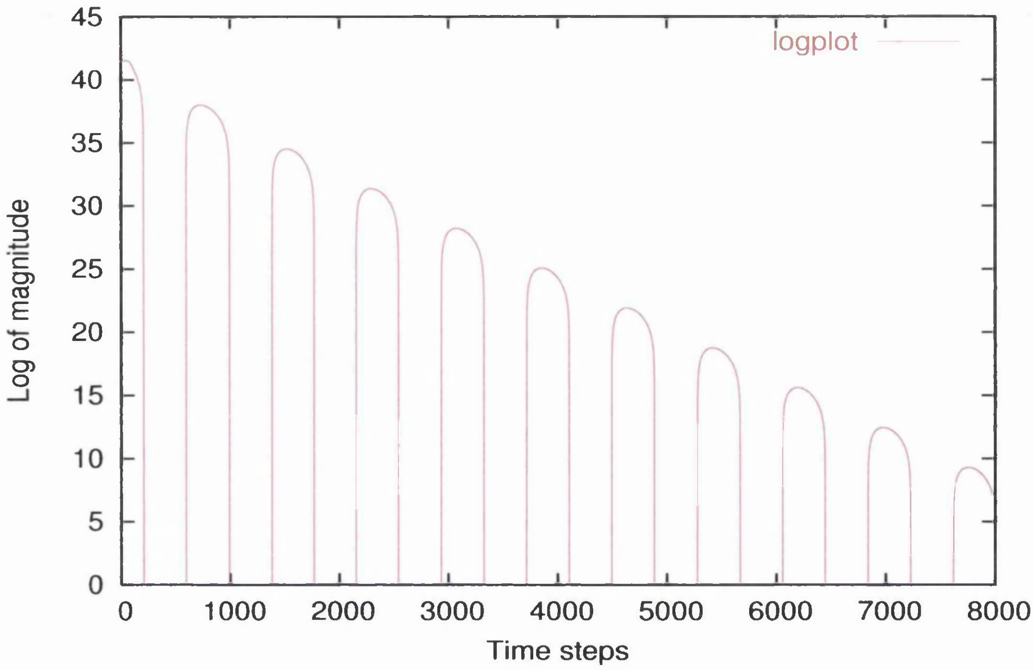

Figure 5.8: The log plot of the positive peaks of the oscillations at a radius of 0.6. From about 1500 time steps the peaks form a perfectly straight line indicating the decay has become exponential.

damping values at any given radius.

To calculate the observed and natural angular frequencies, the following definitions are used:

τ = the natural period,

T = the observed period, obtained from the positive log-plot peaks, see Figure 5.8, when these have settled to form a straight line. T is first calculated in terms of time steps, which must be multiplied by the time interval Δt, in this case 0.01, to obtain the frequency in radians sec^{-1}.

$\gamma/2$ = the gradient, obtained from the log-plot,

$\omega = \frac{2\pi}{\tau}$ = the natural angular frequency,

Ω, the observed angular frequency, is obtained from the damped harmonic oscillator model, so that $\Omega = \frac{2\pi}{T} = \sqrt{\omega^2 - \gamma^2/4}$. Then the observed and natural frequencies are the same when the gradient is zero, corresponding to the SHO with no damping. In practice, the gradient is so small that the observed and natural frequencies only differ in the fourth or fifth decimal place, as can be seen in Table 5.1.

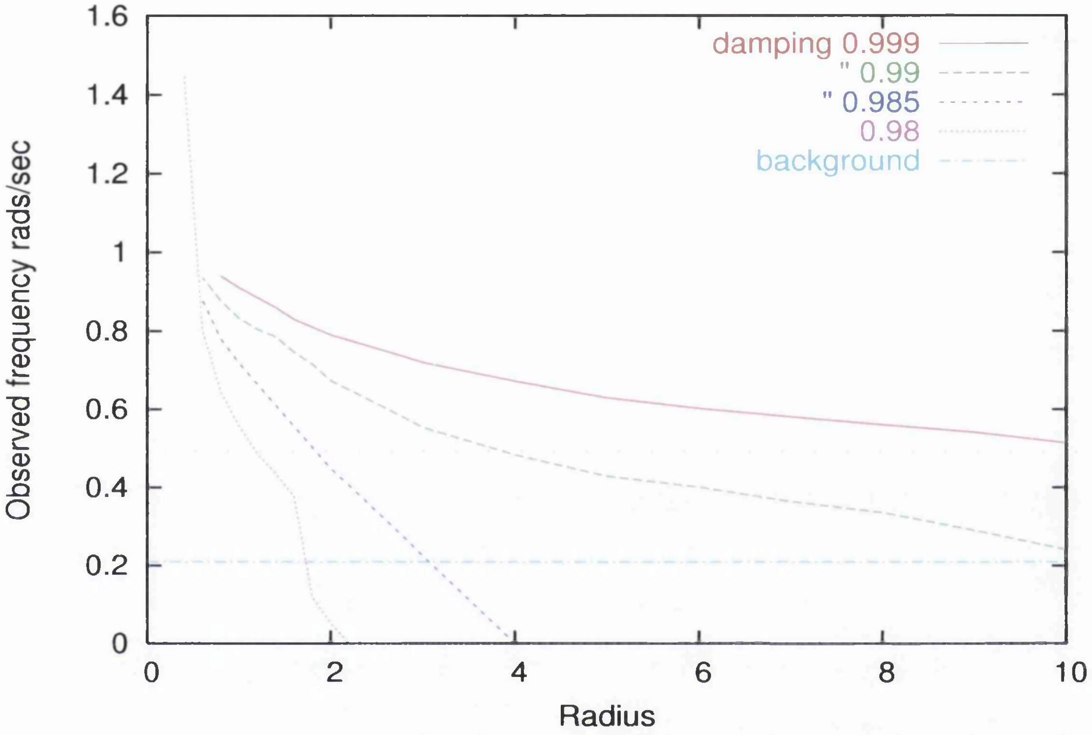

Figure 5.9: The observed angular frequency at different numerical damping values. With damping of 0.99, oscillations start to appear at a radius between 11 and 12, and with damping of 0.999 large radius oscillations with a frequency of $\omega = 0.21$, continue at all radii greater than about 120. This background frequency is shown by the line at 0.21, and its value is dependent on the lattice size. It decreases as the lattice is enlarged. The curves for all damping factors seem to be converging on a common value.

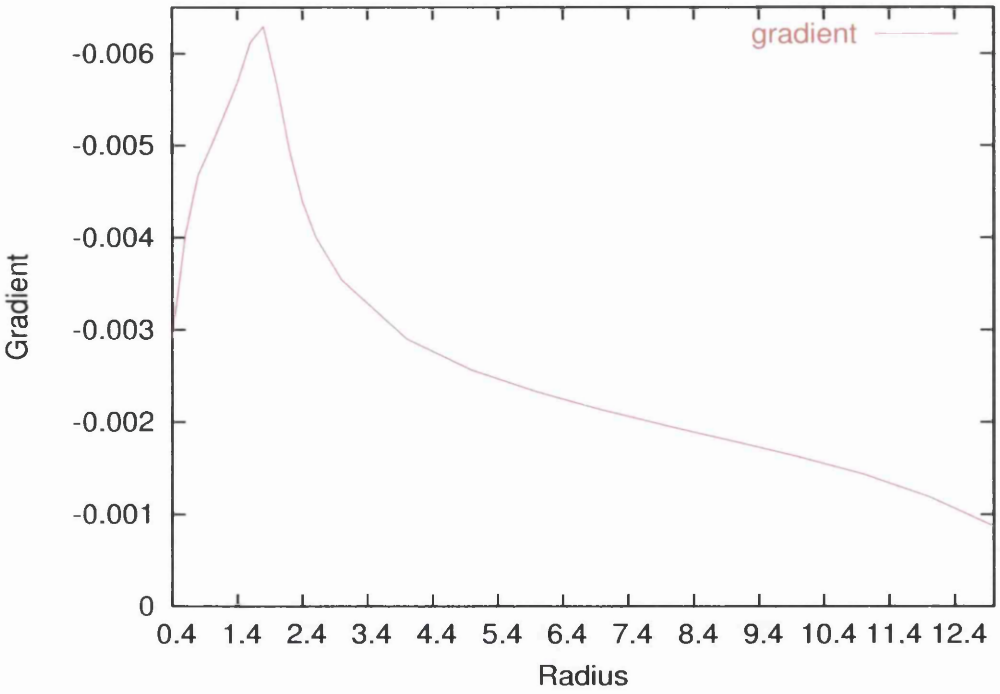

Figure 5.10: The gradient at reducing radius with numerical damping = 0.98. The gradient increases until the radius = 1.8 and increasing oscillations slow the rate of increase.

Figure 5.9 shows that these variations decrease with reducing radius, and would appear to be tending to a common value slightly greater than 1. As the numerical damping is reduced, it becomes more difficult to achieve an exponential rate of decay at the smallest radii, so with damping of 0.999 or less we cannot get further than a radius of 0.8. Referring to Figure 5.9 and table 5.2, it certainly appears that at the smallest radii for which we can obtain applicable data, extrapolation would suggest the observed frequency on a loop is tending to 1, but it should be pointed out that this could still be coincidence rather than conclusive evidence that the mass is attaining its vacuum value. It would be helpful to know if the frequency fall-off is consistent with a 1/radius decay, indicating a power law. Although the period with no damping is regular, the amplitude of the oscillations at smaller radii fluctuates, so minimum numerical damping values of 0.9995 and 0.999 were tried to produce steadier oscillations with a very small exponential decay. However, the difference in the frequency results was negligible in both cases compared with no damping at all, and 0.999 is used when very low damping is required. Another approach was to apply the numerical damping in two stages, starting with a value of 0.98 for the first 1500 steps, and then reducing to 0.999 for the remaining time. Down to a radius of around 2 this results in no oscillations for the first stage, followed by more even oscillations for the second stage. The latter are of smaller magnitude than would otherwise be the case, due to the greater rate of decay during the first stage. This method does not affect the results significantly; the large radius angular frequency is still 0.21 rad s^{-1}, and at very small radii there is a tendency to very slightly increase the frequency. The heavier the damping in stage 1, the more the frequency is increased in stage 2, although only by a very small amount. This procedure was repeated on the 200×200 lattice at a radius of 1000, and this time the underlying frequency was found to be 0.1 rad s^{-1}. This is pointing to a background frequency dependent on the size of the lattice, and suggests that the background 'noise' should disappear given a large enough lattice. If this is so, it would seem reasonable to subtract the background frequency from the observed angular frequency to give a more accurate result at the smaller radii. Insufficient time has prevented testing this on large lattices.

The only way to achieve exponential decay at a radius of 0.4 required rather heavier damping of 0.98 than was considered the optimum, and so the first appearance of oscillations was delayed well beyond the radius where they might have been expected to appear. The impossibility of obtaining an exponential decay at a radius of 0.2 points to a numerical instability, and even at 0.4 it was only just possible to obtain exponential decay with damping of 0.98. With the very light damping regime the smallest radius to allow exponential decay is 0.8.

5.5 *Fermion Mass*

Having now established the ranges for different numerical dampings over which oscillations are observed, we next need to calculate the fermion mass causing the oscillations. If the radius is allowed to reach its minimum value of 0.2, further time steps eventually cause the Higgs field to reach the vacuum value of 1, as the loop disappears. With no string present, the fermions will no longer be localised, so we seek plane-wave solutions, instead of solutions confined to the string. These solutions have the general form,

$$e^{i(k\cdot x-\omega t)}, \tag{5.1}$$

which can be substituted into the Dirac equation,

$$(i\gamma^{\mu}\partial_{\mu}-m)e^{i(k\cdot x-\omega t)}=0. \tag{5.2}$$

Acting twice with the operator gives the Klein-Gordon equation,

$$(\Box+m^2)e^{i(k\cdot x-\omega t)}=0, \tag{5.3}$$

with the solution

$$\omega^2=k^2+m^2, \tag{5.4}$$

in the form of the Einstein equation, $E^2=p^2+m^2$, which, in the absence of angular momentum gives, $E^2=m^2$. Since the vacuum is spatially uniform, (5.4) becomes,

$$\omega^2=m^2. \tag{5.5}$$

If we now take the matrix (4.49), the gauge field is zero in this sector and all terms containing spatial derivatives vanish, so that after substituting $e^{k\cdot r-i\omega t}$, we are left with

$$(\partial_t^2+|g\phi|^2)e^{k\cdot r-i\omega t}=-\omega^2+g^2=0, \tag{5.6}$$

since $\phi=1$ in the vacuum sector. We can now equate $\omega^2=g^2$, giving the solution e^{igt}, and with $g=1$, we therefore have $\omega^2=1$. This suggests that the natural frequency will tend to 1, if the fermions on the loop are going to finally attain their vacuum mass.

As is evident from Figure 5.9, reducing the numerical damping results in an increasingly long tail, which does seem to suggest a power law increase with reducing radius rather than an exponential increase. The natural state has no numerical damping, and is the best state in which to look for a power law. In practice we find the results do not fit for this simple $1/r$ example:

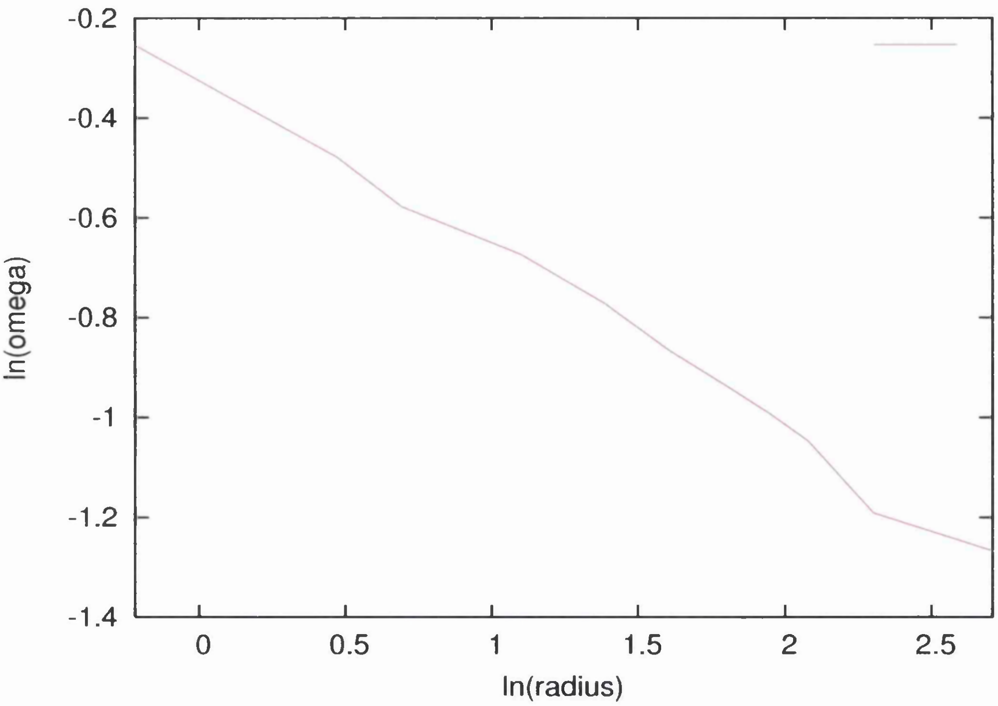

Figure 5.11: The log-log plot of $\ln\omega = \alpha \ln r$ over the radius range 0.8-15, with the background frequency removed, gives the closest approach to a straight line, particularly between radii 0.8 and 8. The main deviations are at radii 2 and 10. The best fit slope is $\alpha = -0.346$

radius r	1000	100	10	1
1/r	0.001	0.01	0.1	1
observed frequency	0.21	0.23	0.51	0.91
net frequency	0.0	0.02	0.3	0.7

Table 5.2.

However, other power relationships which can be tried, for example, $\omega = r^{\alpha} \rightarrow$ $\ln\omega = \alpha \ln r$; or $\omega \sim e^{-\beta r} \rightarrow \ln\omega \sim -\beta r$. The best result proved to be the log-log plot, with the background noise deducted from the observed frequency, Figure 5.9, to give the net frequency values in Table 5.2. This is a reasonable fit to a straight line given the sensitivity of the observed frequency to the technique used, such as the ratio of the two-stage damping times.

In considering the mass at very small radius, it must be remembered that we have stipulated a radial dependence, and due to the symmetry imposed on it, the wave is actually wound round the string. However, the boundary conditions are not symmetrical, so creating the possibility of angular momentum. One solution might be to use anti-periodic boundary conditions, which would give the wave a variation along the loop.

As is evident from 5.9, the mass may be tending to increase to the vacuum value, and we can ask what happens when it reaches 1, with the same energy as a fermion asymptotically far from the string. Because we have forced a condition of axial symmetry around the loop, we are seeing a plane wave in a state which it would not naturally exist in, and this could be part of the explanation for why the mass appears to tend a value greater than 1 at a radius of 0.4. In particular, unlike the vacuum mass case, there are now gauge fields and other factors exerting considerable influence as well. Of course, if we are justified in subtracting the background frequency, the actual angular frequency would extrapolate to a final value much closer to 1.

Assuming that we have acquired fermion mass, we now need to see how this is going to affect the vorton, in particular its lifetime. A typical vorton width is normally taken to be 10-100 string widths. The latter is difficult to assess accurately, but an approximate figure of 2 radius units for the string width is obtained from the Higgs profile when $\phi \sim 0.7$. So if we consider a vorton with a width of 100 string widths, it has a radius of 100 radius units, which is relatively large, and we would not normally expect to see a definite signal at these larger radii. At the lower limit, the vorton would have a radius of 10 radius units, where extrapolation would suggest a fairly small but non-vanishing mass.

We now consider the case of a vorton with a radius of 10 in more detail. With low damping of 0.999, the angular frequency is found to be 0.51 rad s^{-1}. If we assume for the moment that the background frequency of 0.21 can legitimately be subtracted, we are left with a net angular frequency of 0.3, or 30% of the vacuum mass, since $\omega =$ mass. Referring to the paper by C.T.Hill and L.M.Widrow [39], we can use aspects from their model to obtain an approximate lifetime for a vorton, although in that case the method is applied to a straight string. Given that the oscillations cause the string to radiate and lose power power at a rate $\sim \omega A^2$, where A is the amplitude of the oscillations, the current is,

$$J = -J_0\left(1 - \frac{k^2}{4}\right) + \frac{J_0 k^2}{4}\cos\frac{2\pi J_0 t}{q}, \tag{5.7}$$

also,

$$k^2 = \frac{4c\mu^2 e^2}{\pi J_0^2}, \tag{5.8}$$

where J_0 is a large current that has been generated in the string, c is a constant and μ is the mass. Then,

$$A = \frac{k^2 J_0}{4} \sim \frac{\mu^2 e^2}{\pi J_0}, \tag{5.9}$$

and we have,

$$\text{power} \sim \frac{2\pi J_0}{q}\left(\frac{\mu^2 e^2}{\pi J_0}\right)^2 \sim \frac{2\mu^4 e^4}{q\pi J_0}, \tag{5.10}$$

since $\omega = 2\pi J_0/q$ from (5.7). Then if $\dot{J}_0 \propto$ power,

$$\dot{J}_0 \propto \frac{-1}{J_0} \Longrightarrow \frac{d}{dt}(J_0^2) \propto -1 \Longrightarrow J_0^2 \propto -t. \tag{5.11}$$

We then have

$$J_0^2 \sim \text{(an integration constant)} - \text{(a given constant)}t. \tag{5.12}$$

Thus the current dissipates in a time $\propto \mu^4$, and for the vorton under consideration, with a radius of 10 and $\mu = 0.3$, this gives a factor of ~ 100 in its lifetime. This means that although it will take a long time, the current will eventually dissipate in a finite time. It also infers that as $\mu \to 1$ the current will dissipate more quickly. At the other end of the scale, a vorton with a radius of 100 has $\mu = 0.02$, which gives a factor of $\sim 10^7$ in the lifetime, which would be correspondingly extended, to become virtually infinite. Therefore, over the whole vorton radius range, we could expect to see the lifetime decreasing by a factor of $\sim 10^5$ as the radius is reduced from 100 to 10.

5.6 *Conclusions*

We can now consider how well we have answered the questions posed at the end of the introduction.

1. What is the evidence for fermion mass on the loop?

In general, the results have proved to be as expected:

a. The most realistic picture is found with very low or no damping, and in this case the mass is switching on at large radius; in fact there are factors, probably due to the size of the lattice used for practical reasons, that are preventing it turning off at all. The crucial point, however, is that it only becomes significant at very small radius.

b. The frequency, and therefore the mass, continues to increase to a value close to the vacuum mass. This frequency increase appears at first sight to follow a power law rather than being exponential, but rather than a simple $1/r$ power law, we have shown it is $\sim 1/r^{1/3}$. It had been hoped to get down to a radius of 0.2, but an instability prevented this. It might be that at extremely small radius the fermions are not so tightly bound and are starting to move around, so increasing any problems due to numerical issues. Direct tunneling off the string to the vacuum sector by the fermions would not be an issue until very near the end.

2. How does the acquisition of fermion mass affect the lifetime of a vorton?

Even after deduction of the background 'noise', a vorton at the upper limit of the radius range would still show an extremely small mass, and consequently the lifetime would be very long indeed, if not effectively infinite. Even at the lower radius limit in our model, the lifetime would still be very long. We have shown that the fermions can acquire mass over the whole predicted radius range of the vorton.

There are questions that still need further investigation, which lack of time has prevented. The small radius loop analysis in particular could benefit from comparing results as the lattice is enlarged to rather more than the larger 200×200 lattice we have used. This could demonstrate which anomalies are lattice-related, for example the background 'noise' may well become insignificant on a large enough lattice.

The code used for the numerical method of solution has performed very well in the case of the bosonic equations, but some changes and refinements might benefit the fermionic results at small radii. A different numerical method for solving the fermionic equations would be a consideration, or for example, reviewing the update algorithm. These questions tended to became evident towards the end, when it was too late to introduce major changes.

Appendix

1. The Real Bosonic Equations

To determine (2.16) as a real scalar equation, let $\phi = \phi_1 + i\phi_2, \phi^\dagger = \phi_1 - i\phi_2$ and $\phi^\dagger\phi = \phi_1^2 + \phi_2^2$, to give real and imaginary equations:

$$\begin{aligned}&(\partial_0^2 - \partial_r^2 - \frac{1}{r}\partial_r - \partial_z^2)\phi_1 + (\partial_r A_r + \frac{1}{r}A_r + \partial_z A_z)\phi_2 + 2(A_r\partial_r + A_z\partial_z)\phi_2 \\ &\qquad + (A_r^2 + A_\theta^2 + A_z^2)\phi_1 + \phi_1(\phi_1^2 + \phi_2^2 - 1) = 0,\end{aligned} \tag{13}$$

$$\begin{aligned}&i[(\partial_0^2 - \partial_r^2 - \frac{1}{r}\partial_r - \partial_z^2)\phi_2 - (\partial_r A_r + \frac{1}{r}A_r + \partial_z A_z)\phi_1 - 2(A_r\partial_r + A_z\partial_z)\phi_1 \\ &\qquad + (A_r^2 + A_\theta^2 + A_z^2)\phi_2 + \phi_2(\phi_1^2 + \phi_2^2 - 1)] = 0,\end{aligned} \tag{14}$$

resulting in two real scalar equations in ϕ_1 and ϕ_2.

In the vector equations (3.18) and (3.20), substituting for $\phi, \phi^\dagger$ to eliminate the imaginary terms,

$$\begin{aligned}&-i[(\phi_1 - i\phi_2)\partial_r(\phi_1 + i\phi_2) - (\phi_1 + i\phi_2)\partial_r(\phi_1 - i\phi_2)] \\ &\qquad = -2(\phi_2\partial_r\phi_1 - \phi_1\partial_r\phi_2).\end{aligned}$$

Three real vector equations are obtained by substituting in the same way and the resulting system of real scalar and vector equations is thus,

$$\begin{aligned}&(\partial_0^2 - \partial_r^2 - \frac{1}{r}\partial_r - \partial_z^2)\phi_1 + (\partial_r A_r + \frac{1}{r}A_r + \partial_z A_z)\phi_2 + 2(A_r\partial_r + A_z\partial_z)\phi_2 \\ &\qquad + (A_r^2 + A_\theta^2 + A_z^2)\phi_1 + \phi_1(\phi_1^2 + \phi_2^2 - 1) = 0,\end{aligned} \tag{15}$$

$$\begin{aligned}&(\partial_0^2 - \partial_r^2 - \frac{1}{r}\partial_r - \partial_z^2)\phi_2 - (\partial_r A_r + \frac{1}{r}A_r + \partial_z A_z)\phi_1 - 2(A_r\partial_r + A_z\partial_z)\phi_1 \\ &\qquad + (A_r^2 + A_\theta^2 + A_z^2)\phi_2 + \phi_2(\phi_1^2 + \phi_2^2 - 1) = 0,\end{aligned} \tag{16}$$

$$\partial_0^2 A_r - \partial_z^2 A_r + \partial_r\partial_z A_z - 2(\phi_2\partial_r\phi_1 - \phi_1\partial_r\phi_2) + 2A_r(\phi_1^2 + \phi_2^2) = 0, \tag{17}$$

$$\partial_0^2 A_\theta - \partial_r^2 A_\theta - \frac{1}{r}\partial_\theta A_\theta + \frac{1}{r^2}A_\theta - \partial_z^2 A_\theta - 2(\phi_2\partial_\theta\phi_1 - \phi_1\partial_\theta\phi_2) + 2A_\theta(\phi_1^2 + \phi_2^2) = 0, \tag{18}$$

$$\partial_0^2 A_z - \partial_r^2 A_z + \partial_r\partial_z A_r + \frac{1}{r}\partial_z A_r - \frac{1}{r}\partial_r A_z - 2(\phi_2\partial_z\phi_1 - \phi_1\partial_z\phi_2) + 2A_z(\phi_1^2 + \phi_2^2) = 0. \tag{19}$$

Equation (2.25) indicates the particular solution $A_\theta = 0$, in which case we obtain the reduced system of equations,

$$(\partial_0^2 - \partial_r^2 - \frac{1}{r}\partial_r - \partial_z^2)\phi_1 + (\partial_r A_r + \frac{1}{r}A_r + \partial_z A_z)\phi_2 + 2(A_r\partial_r + A_z\partial_z)\phi_2$$

$$+(A_r^2 + A_z^2)\phi_1 + \phi_1(\phi_1^2 + \phi_2^2 - 1) = 0, \tag{20}$$

$$(\partial_0^2 - \partial_r^2 - \frac{1}{r}\partial_r - \partial_z^2)\phi_2 - (\partial_r A_r + \frac{1}{r}A_r + \partial_z A_z)\phi_1 - 2(A_r\partial_r + A_z\partial_z)\phi_1$$

$$+(A_r^2 + A_z^2)\phi_2 + \phi_2(\phi_1^2 + \phi_2^2 - 1) = 0, \tag{21}$$

$$\partial_0^2 A_r - \partial_z^2 A_r + \partial_r\partial_z A_z - 2(\phi_2\partial_r\phi_1 - \phi_1\partial_r\phi_2) + 2A_r(\phi_1^2 + \phi_2^2) = 0, \tag{22}$$

$$\partial_0^2 A_z - \partial_r^2 A_z + \partial_r\partial_z A_r + \frac{1}{r}\partial_z A_r - \frac{1}{r}\partial_r A_z - 2(\phi_2\partial_z\phi_1 - \phi_1\partial_z\phi_2) + 2A_z(\phi_1^2 + \phi_2^2) = 0. \tag{23}$$

2. The indicial equation for the straight string approximation

When $t = +1$, we get either,

$$-p^2 + q^2 + (p-q)\chi = 0, \qquad \chi = 0, 2$$

i.e. $(p-q)(-p-q+\chi) = 0 \Longrightarrow p = q$, or $p = -q + \chi : \chi = (1+t) = 2$.

Or, $-p^2 + q^2 + (p+q)\chi = 0$,

i.e. $(p+q)(-p+q+\chi) = 0, \Longrightarrow p = -q$, or $p = q + \chi : \chi = (1-t) = 0$.

With $\chi = 2$ the solution set is

$$q = \quad 0 \qquad 1 \qquad 2$$

$$p = (0,2) \quad (1,1) \quad (2,0),$$

and with $\chi = 0$ the solution set is,

$$p = (0,0), \quad (-1,1) \quad (-2,2).$$

When $t = -1$, either

$$-p^2 + q^2 + (p-q)\chi = 0,$$

i.e. $(p-q)(-p-q+\chi) = 0, \Longrightarrow p = q$, or $p = -q + \chi : \chi = (1+t) = 0$.

Or, $-p^2 + q^2 + (p+q)\chi = 0$,

i.e. $(p+q)(-p+q+\chi) = 0, \Longrightarrow p = -q$, or $p = q + \chi : \chi = (1-t) = 2$.

With $\chi = 0$ the solution set is,

$$q = \quad 0 \qquad 1 \qquad 2$$

$$p = (0,0) \quad (1,-1) \quad (2,-2),$$

and with $\chi = 2$ the solution set is,

$$p = (0,2) \quad (-1,3) \quad (-2,4).$$

Thus the required coinciding solution sets correspond to $q = 0$ and $p = (0,2)$.

Bibliography

[1] E.Witten; Nucl. Phys. **B249**, (1985), 557.

[2] R.Jackiw and P.Rossi; Nuclear Physics **B190**, (1981), 681.

[3] R.H.Brandenberger, Brown Univ. preprint, BROWN-HET-906 (1993).

[4] R.Schild, I.S.Masnyak, B.I.Hnatyk, V.I.Zhdanov, Astron.Astrophys. **422**:477-482, 2004.

[5] A.A. de Laix,T.Vachaspati, Phys.Rev. **D54** (1996) 4780-4791.

[6] A.A.de Laix, L.M.Krauss, T.Vachaspati; Phys.Rev.Lett. **79** (1997) 1968-1971.

[7] T.W.B.Kibble, IMPERIAL-TP-041001, Oct 2004.

[8] M.B.Hindmarsh and T.W.B.Kibble, Cosmic Strings; Rept.Prog.Phys. **58** (1995) 477-562.

[9] A.Gangui, Topological Defects in Cosmology; Lecture Notes for the First Bolivian School on Cosmology, La Paz, 2001.astro-ph/0110285, (2001).

[10] A.Vilenkin and E.P.S.Shellard; 'Cosmic Strings and other Topological Defects', Cambridge University Press, (2000).

[11] T.W.B.Kibble, J.Phys. **A9**, (1976) 1387.

[12] F.Moraes, Brazilian Journal of Physics, vol.**30**,no2, 304-308, (2000).

[13] J.Magueijo and R.H.Brandenberger; Lecture notes given at IPM School on Cosmology: Large Scale Structure Formation, Tehran, Iran, 1999. astro-ph/0002030, (2000).

[14] T.W.B.Kibble, Aust.J.Phys. **50**, 697-722, (1997).

[15] T. Vachaspati, Contemp.Phys. **39** (1998) 225-237.

[16] T.Vachaspati; lectures given at the 2000 summer school in cosmology at ICTP, Trieste; hep-ph/0101270.

[17] T.Vachaspati, Tufts Univ. preprint, TUTP-94-2, Jul 1993.astro-ph/9401039.

[18] G.'t Hooft, Nucl. Phys. **B79** 276, (1974).

[19] A.M.Polyakov, JETP Lett. **20**, 194, (1974).

[20] T. Vachaspati, CWRU-P18-97, Trieste 1997, High energy physics and cosmology 446-479; hep-ph/9710292.

[21] S.Poletti, Topological defects, Canberra 1995, Cosmology 308-333.

[22] R.H.Brandenerger, Brown Univ. preprint BROWN-HET-1037, Apr 1996.

[23] R.Durrer, Cosmological Structure Formation with Topological Defects; talk at the XXXV Rencontre de Moriond on 'Energy densities in the Universe', January 2000; astro-ph/0003363.

[24] N.B.Nielsen and P.Olesen, Nucl. Phys. **B61**, 45, (1973).

[25] B.Carter, Int.J.Theor.Phys. **36** (1997) 2451-2458.

[26] R.H.Brandenberger, B.Carter, A.C.Davis, m.Trodden, Phys.Rev. **D54** (1996) 6059-6071.

[27] L.M.Widrow; Fermilab-pub-88/61-A, (1988).

[28] A.Gangui and E.Gunzig; Current-Carrying String Loops leading to Vortons; Recent developments in theoretical and experimental general relativity, gravitation, and relativistic field theories, Pt.B, 1290-129, 1997

[29] R.L.Davis and E.P.S.Shellard, Cosmic Vortons, Nucl. Phys. **B323**, 209-224, (1989)

[30] C.J.A.P.Martins and E.P.S.Shellard; Phys.Rev. **D57**: 7155-7176, 1998.

[31] C.J.A.P.Martins and E.P.S.Shellard, Phys.Lett. **B445** (1998) 43-51 (1998).

[32] Y.Lemperiere, E.P.S.Shellard, Phys.Rev.Lett.**91**:141601,2003

[33] C.Ringeval, Phys. Rev. **D64**, 123505 (2001).

[34] A.C.Davis, S.C.Davis, W.B.Perkins; COSMO 99: 3rd International Conference on Particle Physics and the Early Universe, Trieste, Italy, 1999; hep-ph/0005091, (2000).

[35] A.C.Davis, Int.J.Theor.Phys. **38** (1999) 2867-2888.

[36] C.J.A.P.Martins and E.P.S.Shellard, Phys. Lett. **B432**, Number 1, 1998, 58-64.

[37] L.Masperi and M.Orsaria, Int.J.Mod.Phys.**A14**:3581, 1999;

[38] T.Vachaspati, Les Houches 1999, Topological defects and the non-equilibrium dynamics of symmetry breaking phase transitions, 55-75; astro-ph/9903362, (1999).

[39] C.T.Hill and L.M.Widrow, Phys. Lett. **B189**, (1986), 17.